ADDIS ABABA UNIVERSITY
COLLEGE OF NATURAL AND COMPUTATIONAL SCIENCES
SCHOOL OF EARTH SCIENCES

STREAM OF APPLIED GEOPHYSICS

INTEGRATED GEOPHYSICAL EXPLORATION FOR IRON ORE DEPOSIT IN OMO BEYEM, JIMMA ZONE, SOUTH WEST ETHIOPIA

A THESIS SUBMITTED TO

THE SCHOOL OF GRADUATE STUDIES OF ADDIS ABABA UNIVERSITY FOR PARTIAL FULFILLMENT OF THE REQUIREMENTS FOR THE DEGREE OF MASTER OF SCIENCE IN EARTH SCIENCES (APPLIED GEOPHYSICS)

BY

MENGISTU BACHA

ADDIS ABABA UNIVERSITY
ADDIS ABABA, ETHIOPIA
JUNE, 2017

ADDIS ABABA UNIVERSITY
SCHOOL OF GRADUATE STUDIES
SCHOOL OF EARTH SCEINCES

This is to certify that the thesis prepared by **Mengistu Bacha**, entitled: **"Integrated Geophysical Exploration for Iron ore Deposit in Omo Beyem, Jima zone, South West Ethiopia"**and submitted in partial fulfillment of the requirements for the degree of Master of Science in Applied Geophysics complies with the regulations of the University and meets the accepted standards with respect to originality and quality.

Approved by examining committee:

	Signature	Date
Dr. Balemwal Atnafu (Head, School of Earth Sciences)	_____	_____
Dr. Getnet Mewa (Advisor)	_____	_____
Dr.Worash Getaneh (Examiner)	_____	_____
Prof. Tilahun Mamo (Examiner)	_____	_____

DECLARATION

I, the undersigned, hereby declare that the thesis entitled with: **"Integrated Geophysical Exploration for Iron ore Deposit in, Omo Beyem, Jimma zone, South West Ethiopia"** is my original work carried out under the supervision of Dr. Getnet Mewa and has not presented to any University or institution for the award of any degree or diploma program and all sources of materials used for the thesis are duly acknowledged.

Name of the candidate	Signature	Date
Mengistu Bacha	_____	_____

This is to certify that the above declaration made by the candidate is correct to the best of my knowledge and it has been submitted for examination with my approval as University advisors.

	Signature	Date
Dr. Getnet Mewa (Advisor)	_____	_____

ABSTRACT

An integrated geophysical exploration using Magnetic, Induced Polarization (IP) and Gamm-Ray Spectrometry methods were conducted for iron ore exploration in Meti Segeda locality, Omo Beyem woreda, Jimma zone Southwest Ethiopia. Geologically, the area is situated by volcanic rocks represented by basalts, rhyolite and trachyte flows. The NW-SE striking iron bearing zone is occurred between the rhyolite and basalt.

The objective of the study was to map anomalous zones for possible iron ore mineralization with its extents and dip. This objective was achieved through different steps and processes including, collection and reviewing of all relevant secondary data and reports which followed by field primary data collection. In doing so Magnetic, Induced Polarization, Gamm-Ray Spectrometry, and Resistivity surveys were applied for data acquisition. Rock samples were also collected for thin section description, major oxide analysis and susceptibility measurements. Remote sensing methods of ASETR imagery data was used for iron alteration mapping of surrounding area.

The processed, interpreted and integrated geophysical data revealed the mineralized zone as a zone of intersection of high chargeability, high resistivity, intermediate magnetic susceptibility and high Thorium to Potassium ratio. This intersection zone has NW-SE strike direction and represents the mineralized zone. The same zone is correlates with the IP/R inverted section which is easterly dipping with depth of more than 30m and length of 190m. Mineralization seems to have an association with NE-SW and NW-SE structures within survey area. Based on lateral and vertical extents of the mineralized zone the prospect may be used for small scale investment. Based on northern opened Induced Polarization/Resistivity anomalies and processed satellite imagery data, the extensional surveys are recommended to the northwest and northern part of the grid.

Keywords: Iron; deposit**;** Mineralization; Association; Structure; Susceptibility; Magnetic Anomaly; Chargeability;

ACKNOWLEDGEMENTS

I would like to express my deepest appreciation to my advisor, Dr. Getnet Mewa for his especial and devoted support in advices, guidance and encouragements throughout all the work with friendly and exemplary characters. His devotion to reviewing the thesis and providing corrections was really admirable.

I am very much grateful to Ato Bekana Muleta for his unreserved professional support. His contribution in commenting, guiding in all steps of the work and reviewing the thesis for relevant corrections were significant.

I would like also to thank the Geological Survey of Ethiopia for the chance it gave to me and all necessary field equipment and data for the fulfillment of the study.

I would like to extend my thanks to Ato Dawit Mamo for his encouragement, professional support and cooperation for all material I had needed during the study.

My special thanks go to W/o Emebet Lisanu and secretary office members for their support and cooperation in all support I had needed from the office.

I would like to express my deepest gratitude to all graduate students of the stream of Applied Geophysics for their team work sprit and interests for sharing knowledge through discussions during all the study.

Finally, I would like to express my deepest gratitude to mywife; Tadeleche Girma and my daughter; Hasset Mengistu for their time, support and all encouragement for the success of this study.

TABLE OF CONTENTS

LIST OF FIGURES

LIST OF TABLE

ACRONYMS AND ABBREVIATION

μ	Permeability of vacuum
Ω.m	Ohm.meter
NAI (TI)	Titanium Activated Sodium Iodide
2D	2 Dimensional
3D	3 Dimensional
ASTER	Advanced Space Born Thermal Emission and Reflection Radiometer
CGS	Centimeter gram Second
Cps	Count per second
D	Declination
DC	Direct Current
E	East
eTh	Equivalent Thorium concentration
eU	Equivalent Uranium concentration
GPS	Global Positioning System
GSE	Geological Survey of Ethiopia
I	Inclination

I	Current
IGRF	International Geomagnetic Reference
IP/R	Induced Polarization/Resistivity
K	Potassium
mV/V	Mill volt per volt
N	North
NE	North East
nT	Nano Tesla
NW	North West
NW	North West
NW-SE	North West -South East
RES2DINV	Resistivity 2D Inversion
RMS	Root mean Square
SE	South East
SI	Structural Index
NE-SW	North East-South West
SW	South West
SWIR	Short Wave Infrared
Tc	Total count
Th	Thorium
TIR	Thermal Infrared
U	Uranium
UTM	Universal Transverse Mercator
VNIR	Very Near Infrared

CHAPTER I

1. Introduction

1.1 Background

A development in human life is unthinkable without the proper utilization of natural resources, including water, minerals, forest, etc. From time to time the dependency on such resources is increasing. On the other hand, the basic natural resources which were easily obtained in the past are becoming scarce and demand intensive searching using sophisticated exploration techniques. Iron ore deserved special attention by ancient people as it uses to make household tools, weapons and different materials. It had been exploited and smelted at several localities for centuries using primitive technique of smelting. In other way, as it is among the hottest elements besides oil, gas and gold, the demand for iron ore is rising yearly among people and industries.

Due to that fact, iron is arguably the backbone for development and indispensable to modern civilization. It is the fourth most common element in the Earth's crust after oxygen, silicon and aluminum. It is mostly found combined with oxygen forming iron oxide minerals such as magnetite (Fe_3O_4) which contains 72.36% iron and 27.64% oxygen; or hematite (Fe_2O_3) that contains 69.94% iron and 30.06% oxygen. Magnetite occurs in igneous, metamorphic, and sedimentary rocks while, hematite in association with vein deposits as a product of the weathering of magnetite. However, some compounds are contain iron as one of their constitute, based on their chemical compositions, only oxides, carbonates, sulfides and silicates are used as commercially important iron compounds as shown table 1.1

Table 1.1: Major iron bearing minerals (Lindgren and Waldemer, 1933)

Mineralogical name	Formula and %Fe	Common designation
Hematite	Fe_2O_3 (69.9)	Ferric oxide
Magnetite	Fe_3O_4 (74.2)	Ferrous-ferric oxide
Siderite	$FeCO_2$ (48.2)	Iron carbonate
Ilmenite	$FeTiO_3$ (36.81)	Iron-titanium oxide

Depending on the presence of iron in compound, iron ores can be categorized as high-grade (compound that contain more than 60% Fe) and low-grad (which contain 25-30% Fe). Therefore, economical iron ore deposits belong to magnetite, hematite and Limonite. However, iron ores are known to occur in sedimentary, hydrothermal, and magmatic environments, more than 95% of all deposits exploited today are of sedimentary origin that originated as chemical precipitates from ancient ocean water (Jens. G. and Nicolas J.B., 2000). In Ethiopia, extensive iron exploration had been made to meet the plan of constructing steel and metal industry in the period between 1962-1964 (Milan,H., 1963).

1.1.1 Iron Ore Deposit in Ethiopia

The most promising region for base metal prospecting in Ethiopia is low grade Metamorphic or metavolcano sediments belt in the northern, western and south-western parts which are in the metamorphic volcano-sedimentary succession and associated intrusive (Mengesha Tefera et al., 1996). According to Golivkin, N.I. and Kovalevich, V.B. (1982) out of the six genetic types of iron (stratiform, magmatic, hydrothermal, elluvial, sedimentary and placer) the most promising iron ore deposits in Ethiopia is the stratiform type that is connected with late Precamperian volcanogenic sedimentary strata. The magmatic and hydrothermal types are lesser important as compared with the first.

However Murdock.T.G (1960) stated that, none of the ore occurrence in Wollega are of any importance except for local use, Milan, H., (1963) in his study concludes that, most promising high-grade iron ores are confined to the Precambrian metamorphic rocks in central Wollega. About 58 million tons of iron ore reserve is confirmed so far in Bikilal area by Ethio-Korea iron ore exploration project in1987.

And thus, the Precambrian basement complex must be considered as the potentially favorable environment to contain primary high-grade iron ore. The metamorphic type is found in Koree-Gollisso-Nejo area which seems to be one of the promising areas in the country.

1.1.1.2 History of Iron Exploration in Ethiopia

In Mai Gudo area, which is only 60km SE of Jimma, iron ore had been exploited by natives and smelted in a primitive way from extrusive rocks (Milan, H., 1963). Extracting and smelting of iron in current study area (Jimma zone) had been known since the regime of Jimma Aba Jiffar, around 1820th and thus, approximately**,** 5500 kg iron was produced in Jimma area in 1938 using blast furnaces (Milan, H., 1963). During Italian occupation, efforts were made to assess iron deposits throughout the country including Jimma area. As a result, about 20,000 tons of ore were mined (Barnum, B., and Hamrl, M., 1966). In 1945 Murdock estimated the reserve of the ore Jimma area to be 120, 000 tones (Murdock,T.G., 1960). According to Masresha Gebrselassie and Wolf, U. R. (2000), small steel foundry and rolling mill was built in 1962 at Akaki which used imported raw material and scrap iron. Entoto hill had been known for long time to yield limonitic iron ore to meet local requirement of the Akaki smelting factory (Golivkin, N.I. and Kovalevich, V.B., 1982).

1.2 Location and description of the study area

1.2.1 Location and Accessibility

The study area, Meti Segeda (Figure 1.1) is located in Omo BeyemWoreda, Jimma zone in Oromia National Region State at about 329km from Addis Ababa in SW direction. It can be reached by the road from Addis Ababa to Nada via Woliso, Welkite and Sokoru towns driving 293km on asphalt road, from Nada to Iliche village 20km in all-weather gravel road and from Iliche to study area with 10km dry weathered road.

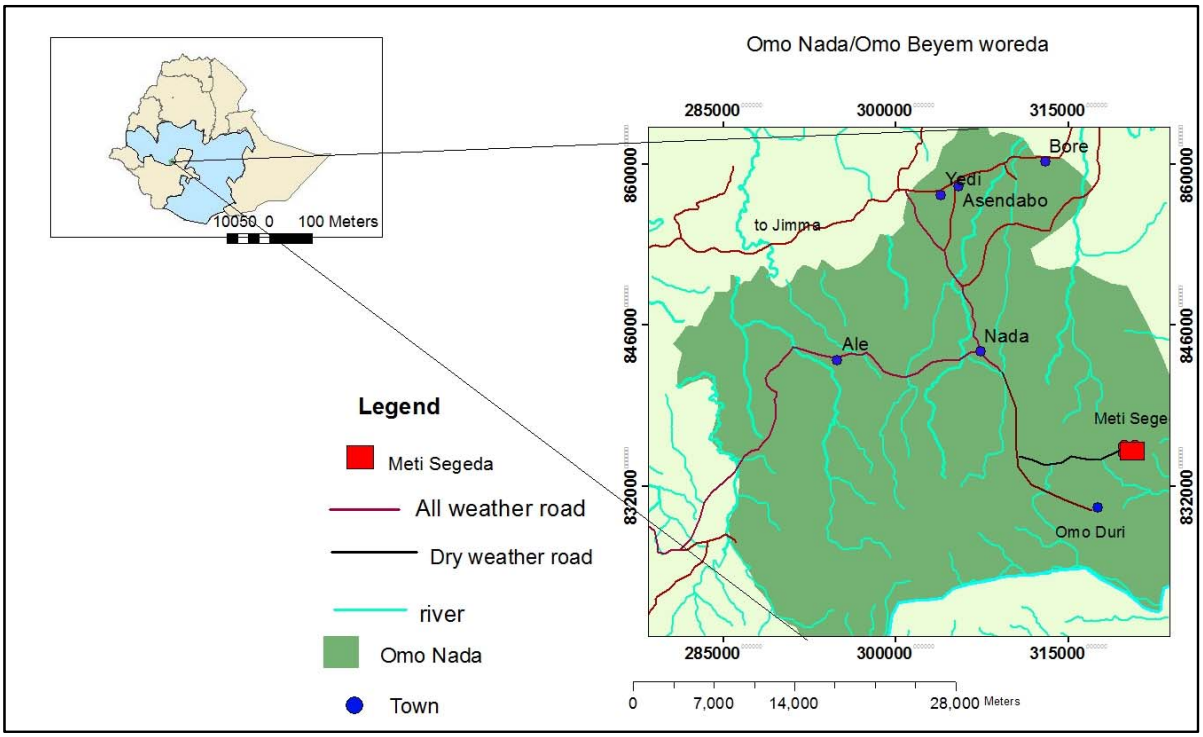

Figure 1.1: Location map of study area

1.2.2 Physiography

Physiographic features of the area are the results of volcanism, faulting and rifting represented by plateau areas, dissected gorges and graben. The study area is situated in the elevated part of

the region between Asendabo graben in the North and dissected Omo River in the south (Workineh Haro et al., 2012 and Habtamu Eshetu et al., 2014).

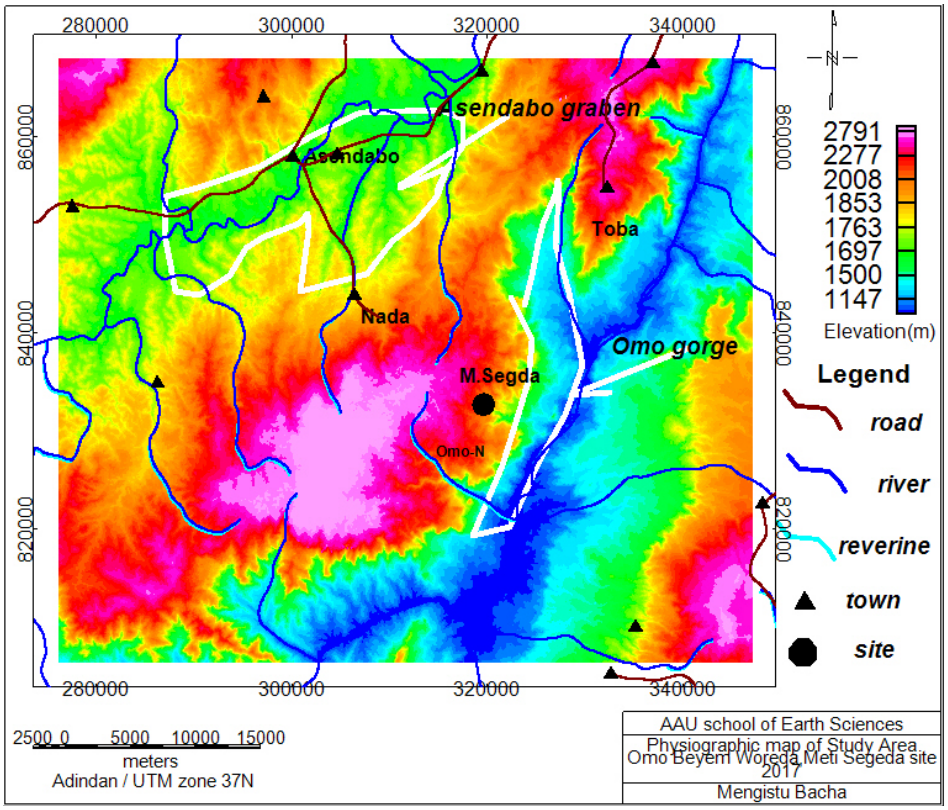

Figure 1.2: Physiographic map of the area

1.2.3 Site description

The study area is bounded by longitudes 37° 22' 0.37" E–37° 22' 31.59" E and latitudes 7°32'56.37" N-7°33'20.57"N in Meti Segeda Kebele of Omo Beyem Woreda. It covers an area of approximately 0.71 km^2. It can be reached through the road from Omo Nada to Omo Duri. The terrain of the site is characterized by slightly steep surface at the northern and southern parts, flat at the northern central and lowlands of soil cover at eastern part of the area with streams at the northern and southern parts. Most of the area is laid within grazing land while only small portion in farm lands. A typical local setting of the area is the outcrop of volcanic rocks at the north east part and its elevation that varies between 2250 m to 2150 m above mean sea level.

1.3 Statement of the Problems

Industrial developments need natural resources as raw materials for manufacturing of varieties of products that are vital to human needs. In this respect, almost all sectors require iron ores as key raw material for the production of machineries and other utilities. World widely, in the form of steel about 20 times more iron is consumed than all the metals put together. The increasing consumption of iron by a country is taken as the indicators of the level of the industrial developments of the same country.

In Ethiopia, (Jimma zone) a primitive way of iron smelting had been known during the regime of Jimma Aba Jifar and lately during the Italian occupation. Based on these information, several studies have been conducted in different areas throughout the country although not much have been done to determine the cumulative potential of all scale deposits that would have considerable input to national potential. And thus, it is not yet possible to use local ore for domestic steel factories. They depend only on imported raw materials and recycled scrap iron. As worldwide consumption of iron in relation to industrialization is increasing from time to time, depending on those sources would be a problem that requires solutions. In relation to this, understanding the nature and viability of even ***small scale iron*** occurrences becoming the demand of mining sectors nowadays to enhance the national reserve.

This study will contribute its part in generating reliable information about the nature and viability of iron occurrence in the current study area and providing valuable input for further studies in the vicinity of the area, which in turn play significant role in understanding and estimating a national ore reserve.

1.4. Objectives of the research project

1.4.1 Main Objectives

To understand and asses the iron prospect of Omo Beyem

1.4.2 Specific Objectives

1. To map lithologic and structural features that may have genetic or spatial association with iron mineralization

2. To determine parameters of mineralized zone through identification and modeling of specific anomalies

3. To determine specific parameters of ore bodies such as lateral extent, depth and dip direction

1.5 Significances and Expected Outcome

The demand for iron ore as raw material for metallic industries is drastically increasing nationally and internationally. As a result, the need for studying the undiscovered resources has become critically essential to promote economic development. In this regard, this study may contribute its part in delineating small scale resource in areas expected to have iron ore potential and enhance the national reserve to the already confirmed ones, such as like the Bikilal and Melka Areba iron deposits. The result of this study is expected to play significant role inproviding the realizable geophysical information for further and extensional studies in and around the area. Generally, after scientific data analysis had been made to recent and previous geophysical, geological and geochemistry data, the following outcomes are summarized:

- All possible geophysical information was extracted from integrated geophysical maps to get equivalent geological meanings
- The horizontal extent, depth and dip of the ore occurrences are identified
- Possible mineralization controlling structures are inferred with the boundary of anomalies

- Subsurface under mineralized zone is modeled to define the extents of mineralized zone

1.6 Previous Works

Understanding the geological conditions of the study area is crucial in order to successfully apply geophysical method and interpret the results. However, more studies were not conducted in current area, some regional scale (1:250,000 and1:200,000 scale) works were so far performed by different scholars around the current area. The purposes of those studies were for iron ore exploration, regional geological mapping, and geo-hazards assessment. Therefore, to prepare this paper some of those works were reviewed.

The geology of Jimma zone, including current study area were a studied by Mohar (1983), Kazmine (1972), Davidsone et al. (1980) and (1983), and Golivkn.N.I (1982). According to Golivkn.N.I (1982), Melka Sedi and Dombova localities in Mai Gudo Mountains, are covered by volcanites of the Trap series, which have the same content of (about 40%) concentrations of iron which related to tectonic zones. The study of Hamral, M. (1963) using laboratory silicate analysis from pits of Mia Gudo areas presented follow.

Table 1.2 Chemical laboratory results of samples (Golivkn.N.I, 1982)

Locality	Fe_2O_3 (%)	SiO_2 (%)	ore
Iliche	37	36	Siliceous ore (10km from current site in west direction)
Kurkure	45	20	Rich compact ore
Aebicha I	45	21	Siliceouse ore
Aebicha II	34.8	41	Unclean breccious ore
Sunaro	58.8	3.5	Clean compact ore

Based on assessments Hamral, M. (1963) concludes that:

- The mineralization of Mia Gudo area is the result of chemical weathering of the country rock.
- Iron and manganese have been leached out of mafic minerals and precipitated to be accumulated in residuals.
- Economically important iron ores are bound to more basic rocks.

- Due to transportation difficulties, the iron ore in Mai Gudo area shows very small economic importance for the time being.

Recently, GSE conducted both geological and geophysical reconnaissance survey in Omo Beyem and Kersa woredas in (Jimma zone) for iron ore exploration in 2016. The surveys were conducted in Meti Segada, Omo Duri, Gato and Bulbul Kebeles. Gamma ray spectrometry, magnetic and IP/R data were acquired as a result. Even though, the technical reports are not yet completed, the progress report indicates the necessity of detail geophysical work to prove if the iron occurrence observed during survey is a surface manifestation or has extents.

1.7 Methodologies

To achieve the objective of the research and answer the proposed questions according to the proposal, several steps were taken. Secondary data and respective reports were collected from GSE resource center and internet. As a result, different literatures were reviewed and finally integrated geophysical methods (Magnetic, IP/Resistivity and Gamma ray spectrometry) surveys as summarized in table 1.3 and remote sensing were employed.

Table 1.3: The details of the survey grids and summary statistics

Area		**Geographic coordinate**		**Line orientation**		**Area (Km^2)**
Meti Segeda		37° 22' 0.37" E–37° 22' 31.59" E 7° 32' 56.37" N–7° 33' 20.57" N		N-S for Magnetic and Radiometric, E-W for IP/R and VES		0.71Km^2
Summary grid statistics of the geophysical survey						
No	Geophysical Method	No. of lines	Sampling interval	No of observation/ No of Dipoles	Volume of Work (Line Km	Instrumentation
1	Total field Magnetic	8	100mX20m	134	2.8	IGS-2/MP4 Proton Precession Magnetometer
2	IP/Resistivity	5	50mX20m	141	3.5	IPR-12 Receiver 3kw-TSQ-2 Transmitter
3	Radiometry	14	50mX20m	227	4.3	GAD-6 Gamma-Ray Spectrometers
4	VES (Schlumberger Array)	1	150m	3	-	Scintrex made TSQ-2 Transmitter and IPR-10A receiver
Total		28	-	505	10.6	

Fifteen days field work was conducted to collect geophysical data along selected profiles (crossing the strike of assumed anomaly) according to base map prepared during pre-field period. Some rock samples were taken from site for thin section, major oxide and petro-physics investigation. Relevant field photos and necessary notes were acquired as well. Remote sensing satellite imagery data processing was employed to map iron oxide alteration zone.

1.7.1 Rock Samples Collections

To help geophysical data interpretation process, seventeen rock samples were collected (Figure 1.4a) from the host rock and mineralized zone for thin section investigation, rock slab preparation and major oxides investigation. Samples were coded and their respective location, elevations and descriptions were recorded during collection. All information of rock samples were entered into computer and fourteen samples were selected and submitted to Geological Survey of Ethiopia to Chemical and Geotechnical laboratories. Accordingly, the compositions for six samples (from iron bearing zone) were determined. Thin sections for twelve samples were

prepared and their representation of rock and mineral types determined. Petro physical parameter (magnetic susceptibility) from twelve rock slabs was measured (Figure1.4b) using Norwegian made magnetic susceptibility meter. Before measuring susceptibility; the meter was calibrated using its own calibration sample. Slabs of rock samples prepared in laboratory with an approximate dimension of 4x2x2cm were inserted into the sensor of susceptibility meter and reading was taken from its six faces and the average of those is considered as the susceptibility values of the same sample.

Figure 1.3: Field rock sample collection (a) and Magnetic susceptibility measurement (b)

Susceptibilities that were measured in CGS unit were converted into SI unit by the relation of k_mSI unit = k_m cgs 4π unit; were k_m is magnetic susceptibility. Measured susceptibilities (k_m) range between 174.584 SI units to 8063.52 SI units as shown table1.4. All information of the thin sections analysis and iron oxide composition of rock samples with their measured susceptibilities were used during geophysical data interpretation.

Table 1.4: Laboratory results for susceptibility (k) measurements and (SiO2 and Fe2O3) concentration for rock samples

Sample ID	X	Y	SiO_2 (%)	Fe_2O_3 (%)	k(SI)
MT01	320248	835128			226.08
MT02	320291	835145	38.4	40.68	1159.28
MT03	320331	835152	29.96	52.24	1875.2
MT04	320434	835231			174.584
MT05	320415	835070			369.264
MT06	320524	835098			8063.52
MT07	320415	835328			231.104
MT09	320225	835112			458.44
MT10	320326	835164	39.46	35.88	639.304
MT11	320224	834710			360.472
MT12	320047	834916			
MT 13	320440	835290			282.6
MT 14	320220	835110			175.84
MT 15	320220	835110			481.048
MT16	320390	835110	42.84	34.96	1072.62
Tr-2-1	320457	835309	10.4	66	
Tr-2-2	320458	835309	47.56	30	

1.8.2 Remote Sensing: Thermal Emission and Reflection Radiometer (ASTER)

Iron alteration distributions were detected in wider zone around current study area by using ASTER Imagery data with Qgis software. Band ratio of B2 to B1 was used to enhance the small contribution of iron oxide minerals to discriminate iron bearing zone shown in figure 5.38.

1.9 Structures of Thesis

This thesis has been developed as a series of chapter that are connected each other.

- Chapter I: Introduction
- Chapter II: Geology of the area (regional and local geology)
- Chapter III Basic principles of geophysical methods
- Chapter IV: Geophysical Exploration (data acquisitions, processing and presentation)
- Chapter V: Interpretation and Discussion
- Chapter VI: Integrated Interpretation
- Chapter VII: Conclusions and Recommendations

CHAPTER II

2. Geological and Structural Setting

2.1 Regional Geology

According to Davidson et al. (1983) the main volcanic sequence for Jimma and the surrounding region, which is part of the southern volcanic plateau, are of Eocene to Oligocene Epoch. It consists of basalt, rhyolite, trachyte, tuff and ignimbrite. Mengesha et al. (1996) mapped the geology of Jimma area (Figure 2.2) as Cenozoic volcanic of early Tertiary rocks that include:

- Lower Jimma volcanic (Pjb): mainly basalt flows or flood basalt
- Upper Jimma volcanic (Pjr): mainly silicic flows that include rhyolitic and trachyte flows and tuff.
- Nazret series (Nn): Thick succession of welded ignimbrite, minor basalt and rhyolite flows.

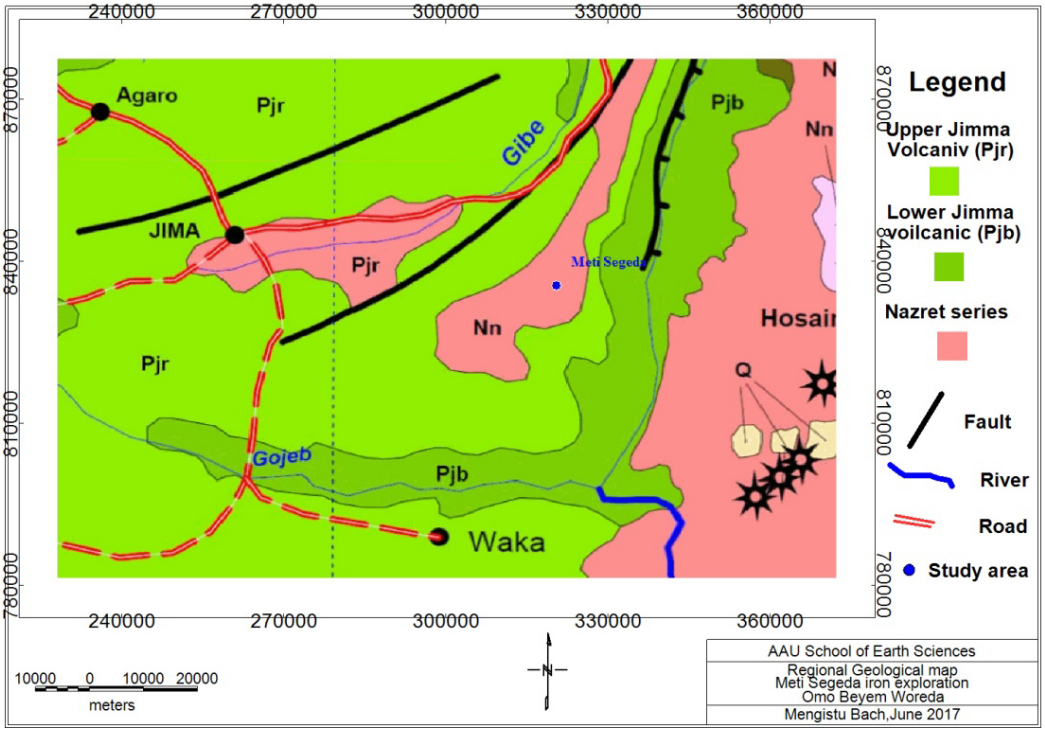

Figure 2.1: Regional geological map of Jimma area (Extracted from the Geology of Ethiopia by Mengesha et al. (1996).

According to Mengesh et al. (1996) the large region of Mai Gudo area is built up of volcanic rocks of trap series while, the highest part of the mountain is built of dolerite and olivine-basalt. The common rocks of the area are extremely weathered trachyte-rhyolite.According, to Workineh Haro et al. (2012), the regional stratigraphy from oldest (Omo trachyte) to youngest (rhyolite flows) seems the following: Omo trachyte (mainly exposed in the Omo valley), lava flows (lower basalt flows), lower trachyte flows, lower pyroclastics, middle basalt flow, middle trachyte flows, upper basalt flows (that forms elevated topography), upper trachyte flow, rhyolite flows which is exposed at east of Nada town including current study area. In other way, on the road from Nada (only 15 to 20km from the study area at the NW direction) to the study area, the outcrops of major lithological unit encountered from bottom to top is lower basalt, prorphrtic rhyolite, pyroclastic fall, weathered rhyolite and fresh rhyolite as shown in figure 2.1

Figure 2.2: Outcrops of major lithological units encountered on the way from Nada town to study area: a) prorphrtic rhyolite, b) ash (pyroclastic falls), **c**) weathered rhyolite and d) fresh rhyolite.

2.2 Local Geology and Mineralization

According to Getnet Gezahegne et al. (2016) the local geology (Figure 2.3) of the area is grouped to slightly weathered geryish to pinkish color trachyte flows and massive and black basaltflows.The result of thin section analysis, measured susceptibilities, gamma ray spectrometry maps and the rock type mapped byMengesh Tefera (Figure 2.2,) are correlated to those rock units within the area.

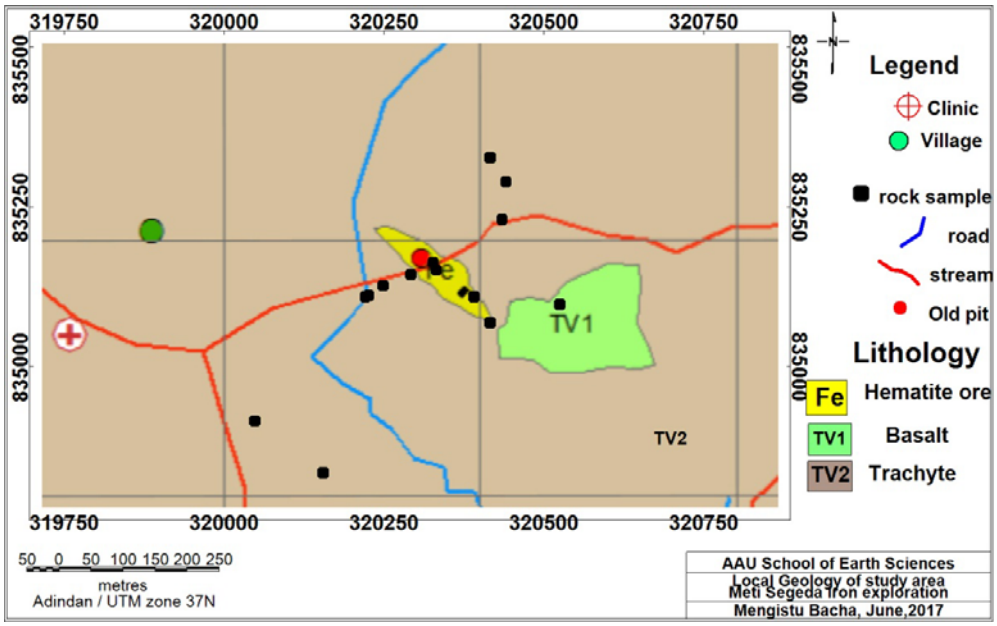

Figure 2.3 Local geology of study area

Light yellowish to black hematite and limonite iron ores (Figure 2.4) observed in N50^{0}W striking mineralized zone within those volcanic units (Getnet Gezahegne et al., 2016). The mineralization is associated with the late residue of magmatic solution which, deposited with rhyolite/trachyte after the main volcanic. This could occur when, inhomogeneous magmatic flow left magma first and the iron with rhyolite lately. The mineralization is thus, a residual concentration of iron oxides with silica after the main volcanic episode. From the thin section analysis, opaque minerals (iron oxide/hematite) have 15-30% in five rock samples; quartz minerals show 40-55% in most rock samples and opaque minerals (iron oxide/magnetite) minerals of 13% is observed in

one rock sample in basalt rock unit. Major oxide analysis for six rock samples from mineralized zone show that, 29-66% iron (Fe_2O_3) while, 10-47% of silicon oxides (SiO_2).

Figure 2.4: N50^{0}W striking outcrop of iron-bearing zone

2.2.1 Thin section descriptions for rock samples (by: Workineh Haro, GSE)

Sample No	Easting	Northing	Elevation
MT06	320524	835098	2146m

Major mineral or phenocryst=olivne =2%

Groundmass=Plagioclase laths and microlites 32%

Oliven 15-20%

Texture = intersertal texture and partly microphenocrystic with flow texture.

Frock name = olivine basalt

Remark: The groundmass is dominated by laths or microlites of plagioclase, olivine and glass. The rock shows intersertal texture.

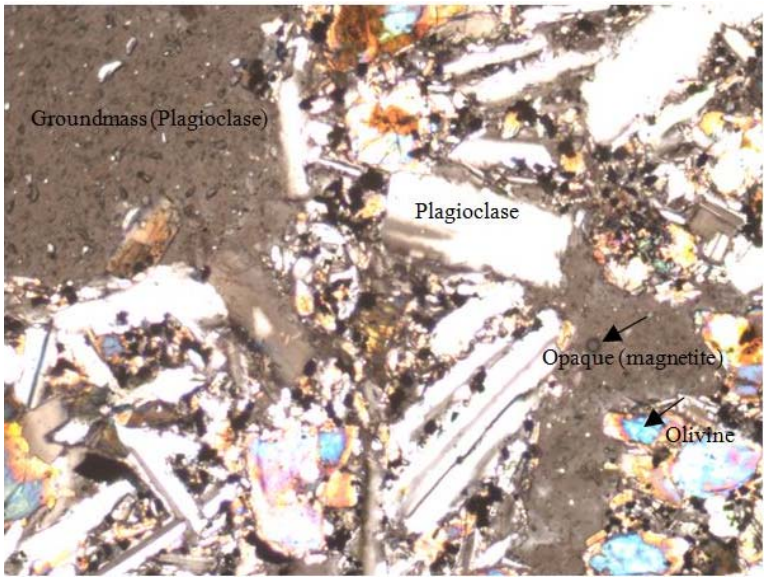

Figure 2.5: Thin section view for basalt rock sample

Sample No	Easting	Northing	Elevation
MT01	320248	835128	2216m

Major minerals Phenocrysts = sanidien = 5%

Groundmass =Major composition is radiating groundmass of quartz 40%, normal quartz 10%

Glass 15%-20%, Iron oxide (hematite) = 15%, groundmass of sanidine =15%

Texture= slightly phenocrystic and mainly glassy

Rock name=Porphyritic Rhyolite

Remark: The major mineral occur as glassy mineraloid of quartz

Sample No	Easting	Northing	Elevation
MT04	320434	835231	2177m

Groundmass (quartz) = 55%

Minor mineral=sanidine laths and micrlites =20%, Glass 10% alteration minerals 15%

Texture = glassy

Rock name = Glass rhyolite

Remark: The major minerals occur as groundmass consisting of quartz, phenocrysts are rare.

Sample No	Easting	Northing	Elevation
MT09	320225	835112	2217m

Major mineral: Aegerine augite = 20%, sanidine microloids 30%, quartz microloids 40%

Minor minerals: Glass=10%

Texture =Glassy and also show flow texture

Rock name: Trachyte

Remark: The major composition occur as glass which exhibit forms of quartz and sanidine also aegirine augite. They mostly occurs as mineraloids

Sample No	Easting	Northing	Elevation
MT 11	320224	834710	2136m

Phenocrysts=sanidine

Groundmass=aegerine augite 15%-20%, Quartz and mineraloids of quartz

Sanidine laths and microlites

Glassess are often altered to iron oxide (hematite)

Texture: glasses with slightly phenocrysts texture

Rock name: Trachyte

Remark: The composition of the rock is mainly glass and also occurs as mineraloids

The magma is not well developed to form crystalline shape for the minerals. This shows the flow is quickly cooled.

Sample No	Easting	Northing	Elevation
MT 07	320415	835320	2217m

Major minerals (groundmass) of quartz 40% and sanidine 30%

Minor minerals =phenocrysts of quartz 3% and sanidine 4%, glass 7%, opaque 3%,alteration minerals 3%

Texture = glass texture

Rock name = Rhyolite

Remark: The major minerals occur as glass groundmass

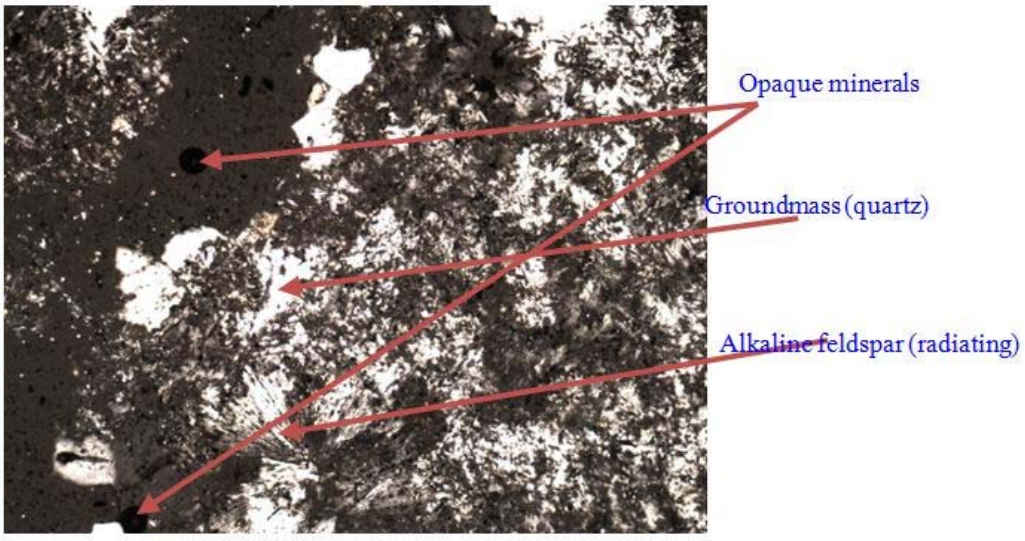

Figure 2.6: Thin section view for rhyolite rock sample

Sample No	Easting	Northing	Elevation
MT 12	320047	834916	2232m

Groundmass: Mineraloids of quartz=45%

Opaque (hematite) =20%, glass=20%, mineraloids of sanidine =15%

Texture=glassy

Rock name: Rhyolite

Remark: The major composition occurs as groundmass which are mostly cryptocrystalline or as mineraloids. They don't show definite boundary and shape. This shows fast cooling of the magmatic eruption.

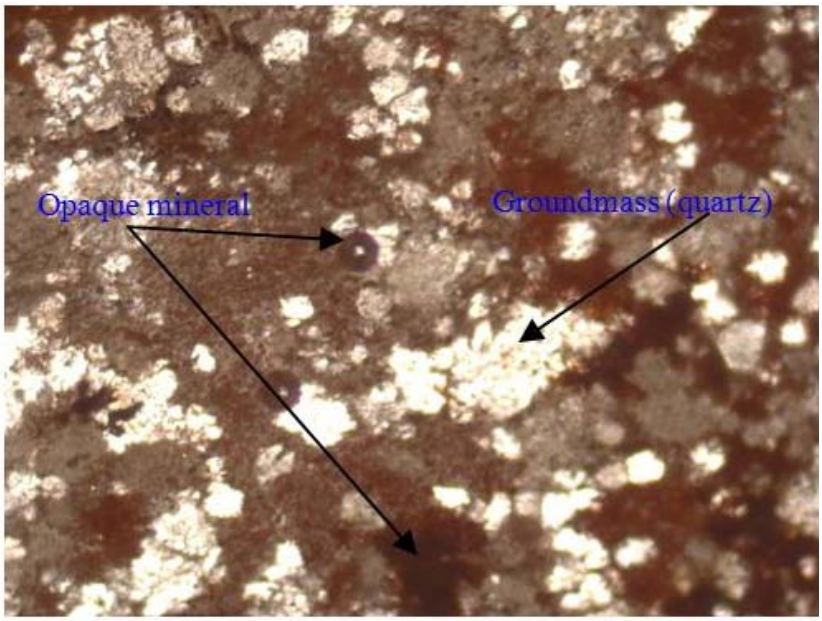

Figure 2.7: Thin section view of rhyolite rock sample

Sample No	Easting	Northing	Elevation
MT 13	320440	835290	2197m

Phenocryst= sanidine 5%, quartz 4%

Groundmass of quartz and its mineraloids 40%, Aegirine augite 20%

Sanidine laths and microlites 15-20%, opaque= trace 1%

Glass =1%

Texture: glass and to some extent porphyritic

Rock name: Trachyte

Remark: The minerals occur mostly as groundmass and those are mostly mineraloids.

Sample No	Easting	Northing	Elevation
MT 14	320220	835110	2179m

Phenocryst = Orthopyroxene 3%, and clino pyroxene 2%

Groundmass=sanidine crystal mineralites 15-20%

Quratzt radiating =55%, opaque and altered minerals minerals 10%, glass 10%

Texture: Glass and slightly porphyritic

Rock name: Rhyolite

Remark:The minerals mostly occur as radiating mineraloids of quartz and as microlites (sanidine)

Sample No	Easting	Northing	Elevation
MT 15	320220	835110	2179m

Phenocryststs =Sanidine 5%, quartz and quartz mineralloids 40%

Opaque (iron oxide) 30%, glass 15%, minor minerals or groundmass= glass and plagioclase 10%, Texture; It is slightly porphyritic and show radiating texture of quartz

Rock name: Porphyritic rhyolite

Remark: The major composition is glassy radiating quartz with iron-oxide minerals (hematite)

2.3 Geological Structure

The rifts (graben) in the Jimma map zone have similar origin to the MER, eventhough pyroclasts formed are lesser in volume in Jimma rift graben. The major structures in Jimma map zone show ENE-WSW trend. This structure controls the location of local graben in the area. The graben is formed by normal faults which is asymmetrical. The eastern limit of the Asendabo Graben is east of Nada.

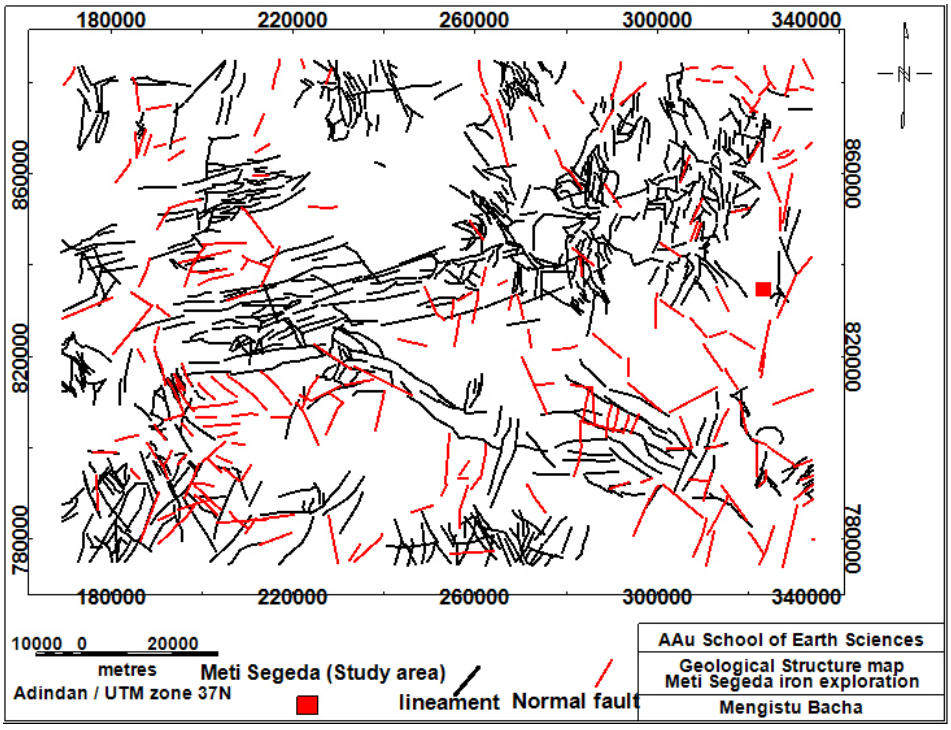

Figure 2.8 Geological Structure of the study area

Around the current study area normal faults and lineaments are oriented NW-SE to the west of the site and N-S oriented faults are observed to the east of the study area. In the northwest of the study area several short fault and lineaments are observed.

CHAPTER III

3. Basic Theory and Principles of Geophysical Methods

3.1 Magnetic method

Magnetic method is used to detect iron ore deposits, delineating lithologic boundaries and structures that are favorable for mineralization, mapping intrusive bodies etc. It is based on small variation in susceptibility of magnetic minerals. The shape and amplitude of the resulting anomaly caused by the induced magnetization of magnetic minerals related to the size and shape of the body, and its orientation with respect to the Earth's field. (Reynolds, R.L., 1990)

3.1.1 Magnetic field strength and flux density

Just like an electric field strength give rise to an electric current, a magnetic field strength can give a magnetic flux. If the magnetic flux density (magnetic induction) which is the flux per unit area is denoted by **B** and **H** is the inducing field strength, then: $B = \mu H$..... (3.1).

The concept of Earth's magnetism is based on the origin of magnetism and the interaction of magnetic force between magnets. Basic magnetism theory tells us that magnets of same polarity exert repels forces on each other while, of opposite polarity attract each other. From Coulomb's law, the interaction force between two magnetic poles of strength P_1 and P_2 that separatedby "r" meter is given as:

$$F = \frac{\mu_o}{4\pi\mu_r}\frac{P_1P_2}{r^2} \quad \text{.....(3.2).}$$

, where F: is magnetic force in Newton (N), r in meter and P_1 and P_2 are pole strength in Ampere meter (Am). μ_o: Constant known as permeability of vacuum which has a value of 4 $\pi x10^{-7} NA^{-2}$, μ_r : a dimension less quantity known as relative permeability of the medium. $F_n = \frac{-\mu_o}{4\pi\mu_r}\frac{P_1P_2}{r_n^2}$ is attractive force from the negative pole of the bare magnet and $F_p = \frac{\mu_o}{4\pi\mu_r}\frac{P_1P_2}{r_p^2}$ is the repelling force from the positive pole of the bar magnet.

And thus the total force F_T acting on $+P_2$ is give as the vector sum of F_n and F_p: - $F_T = F_n+F_p$..... (3.3)

As the magnetic field is defined as the magnetic force per unit pole strength, its components at the location of the positive test pole P_2 at their respective distance are given as:-

$B_n=\frac{F_n}{P_2}=\frac{-\mu_o}{4\pi\mu_r}\frac{P_1P_2}{r_n^2P_2}=\frac{-\mu_o}{4\pi\mu_r}\frac{P_1}{r_n^2}$ ..... (3.4)

and $B_p=\frac{F_p}{P_2}=\frac{\mu_o}{4\pi\mu_r}\frac{P_1P_2}{r_p^2P_2}=\frac{\mu_o}{4\pi\mu_r}\frac{P_1}{r_p^2}$ .....(3.5)

According to electrodynamics theory, the force field which is known as magnetic field is experienced by the charge in motion. Therefore magnetic fields and magnets are originated from electric charge in motion.

3.1.2 Earth's Magnetic Field (B)

It depends on Earth's internal properties and thus, gives lots of information about the interior of the Earth. The Earth's magnetic field (B-field) can be represented by a magnet dipole (figure 3.1) situated at the center of the Earth. It is vector quantity that is varying both in magnitude, direction over the surface of the earth. It also varies in time as well. The present theory about the origin of the Geomagnetic field is an electric current (in the form of loop) in the liquid iron of the Earth's core which is surrounded by a magnetic field just in similar fashion as a bar magnet.(Thomas, M.D., et al, 2000)

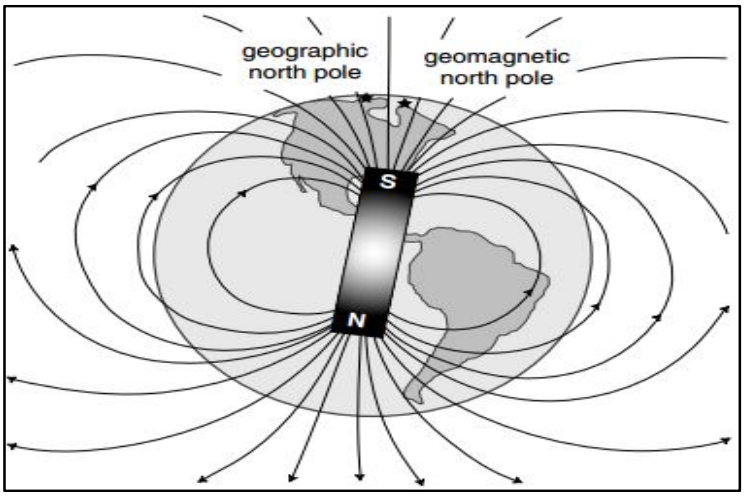

Figure 3.1: Earth's geomagnetic dipole as a bar magnet

3.1.3 Components of the Earth's total magnetic field

The Earth's total magnetic field (B_T) consists of an external component (B_{ext}) and an internal component (B_{int}) which can express by: $B_T = B_{ext} + B_{int}$ ..... (3.6)
The external component (B_{ext}) originate from magnetic field induced by the flow of ionized particles emitted by the sun within the ionosphere toward the magnetic poles while, the internal component (B_{int}) originates from the dipole field or main field (B_D) generated by the fluid core and magnetized crustal rocks known as rock magnetism or anomalous magnetic field (B_{rm}). Hence B_T is given as: $B_T = B_{ext} + B_{int} = B_{ex} + B_D + B_m$ ..... (3.7)
However, the main constitute of Earth's total magnetic field (99%) of the total field is the dipole field (B_D)rock magnetism or anomalous field (B_{rm}) is produced by ferromagnetic minerals and rocks in the Earth's crust which is variable and the weakest one.

3.1.4 Elements of the Earth magnetic field

A vector Earth's magnetic field has maximum intensity of about $6x10^{-5}$Tesla near to the magnetic pole and $3x10^{-5}$ Tesla near magnetic equator. It can be expressed as Cartesian components parallel to any the three orthogonal axes. The magnitude of the magnetic vector is given by the field strength **B**; and its direction is specified by two angles figure 3.2 known as declination **D** and inclination **I**. Declination is the angle between the magnetic meridian and the geographic meridian while, the inclination is the angle at which the magnetic vector dips below the horizontal.

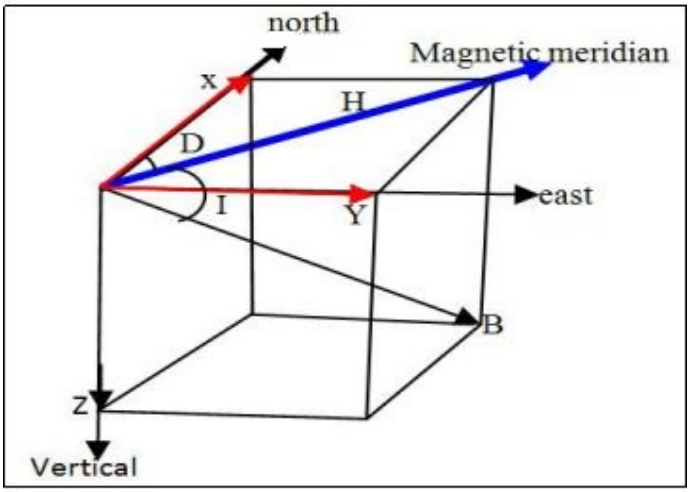

Figure 3.2: Elements of the Earth's magnetic field: inclination **I,** declination, D and total magnetic field **B**

Telford et al., (1990**),**the field can be described in terms of the vertical component (Z), positive down, and the horizontal component (H), which is always positive. X and Y are the component of H, which are considered positive to the north and east, respectively. Those elements are related as follow.

$$B^2 = H^2 + Z^2 = X^2 + Y^2 + Z^2 \quad \text{..... (3.8)}$$

$$H = F\cos I, Z = F\sin I \quad \text{..... (3.9)}$$

$$X = H\cos D, Y = H\sin D \quad \text{..... (3.10)}$$

$$\tan D = \frac{Y}{X}, \tan I = \frac{Z}{H} \quad \text{..... (3.11)}$$

3.1.5 Magnetic properties

3.1.5.1 Magnetization and magnetic susceptibility

When a magnetic substance say iron, is placed in external magnetic field, **B**, the magnetic material will produce its own magnetization (**J**). This phenomenon is called induced magnetization (**J_i**). The direction of induced magnetization $\mathbf{J}_i$ is the same as the direction of the inducing field **B**. In practice, the induced magnetic field (the one produced by the magnetic material) will look like as if it is being created by a series of magnetic dipoles located within the magnetic material and oriented parallel to the direction of the inducing field, **B**.

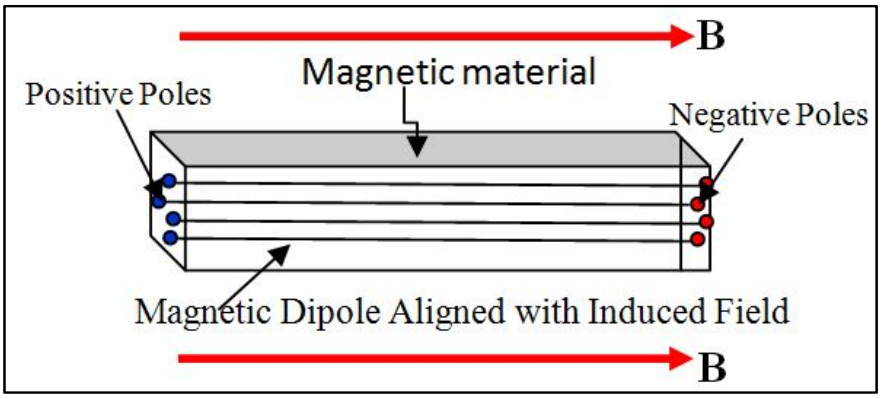

Figure 3.3: Inducing field, **B** producing Magnetization within magnetic material that looks as if the material contains magnetic dipoles aligned with **B**. (Kamar Shah Ariffin, EBS 309)

The ability of a substance to be magnetized when exposed to external magnetic field is known as magnetic susceptibility (k) of the materials which can relate to the induced magnetization

(Chapman & Hall, 1997),$\mathbf{J_i}$) as: Ji= kB..... (3.12)

Magnetic susceptibility k is a unit less constant that is determined by the physical properties of the magnetizing material. (Philip Kearey, 2002). The negative values of (k<0) indicate that, the induced magnetic field $\mathbf{J_i}$is in the opposite direction as the magnetization field **B,** whereas positive susceptibility (k>0) implies that, induced magnetic field is in the same direction as the magnetizing field **B.** The shape of a magnetic anomaly depends on the shape, depth of the anomalous body and on its orientation with respect to the profile direction and with respect to the direction of the inducing magnetic field. If k_b represents the susceptibility of an anomalous body and k_h is of the host rocks, then the susceptibility contrast is given as

$\Delta k = k_b - k_h$..... (3.13)

$\Delta k > 0$ results in positive magnetic anomaly and $\Delta k < 0$ is result in negative magnetic anomaly. Therefore, magnetic anomaly is based on contrast between susceptibility of the anomalous rock body and that of the surrounding host rock.

3.1.6 Magnetic Data Processing

3.1.6.1 Filtering

Processing of observed magnetic field undergo through some mathematical operations, enhancing certain components of the observed field while, suppressing the other components

by using different filtering techniques like reduction to pole and derivatives. The essential goal of signal processing is to improve the signal-to-noise ratio. A signal is defined as a sequence of numbers that contains interesting (i.e. wanted and relevant) information about some property of the Earth or a geological process. Noise, the residual data left over after the signal has been isolated, contains either no information or else it contains unwanted or irrelevant information. The signal in one data process purpose might be noise in other data processing. Therefore some filtering techniques should commonly apply to magnetic total field to extract maximum information from it.

Analytic signal or total gradient is formed through the combination of the horizontal and vertical gradients of the magnetic anomaly. Mathematically it can define as the square root of the sum of the square of the derivatives in the x, y and z direction.

$$|A(x,y)| = \sqrt{\left(\frac{dB}{dx}\right)^2 + \left(\frac{dB}{dy}\right)^2 + \left(\frac{dB}{dz}\right)^2} \quad \text{..... (3.3)}$$

Where, $|\ A(x,y)\ |$ is the amplitude of the analytic signal at (x,y), B is the observed magnetic field at (x,y). The main feature of the AS is that its independency on the inclination and magnetization direction. It is very sensitive to edge effects of the causative magnetic bodies and reveals the edges and the horizontal dimensions of geological formations. It has peak amplitudes over magnetic contact (Nabighian.M.N. (1972). In addition to banded and linear magnetic anomaly patterns, many circular small-scale bodies can be observed in using analytic signal (Roset, W.E., et al 1992). In other way, in order to remove the asymmetry in magnetic anomalies due to the inclination of the Earth's magnetic field, magnetic data generally need to be reduced to the pole, particularly for area close to the magnetic equator. (Mark E. Everett, 2013).

The analytic signal is one way that used to reduce magnetic anomalies to magnetic pole (Oasis Montaj releas 4.3, 1999). Therefore, the complication of the interpretation of magnetic data due to dipolar nature of magnetic field can be solved by removing the effects of the geomagnetic field in using Analytic signal filter.

The directional cosine filter is very good for removing directional features (E-W trading exaggerated magnetic field at equator) from a grid. The rejection option can be narrowed or widened by setting the degree of the cosine function so that highly directional features can be isolated. Directional cosine filter of 85 to 90 degree are good to remove E-W trading artifacts that occurred due to low latitude (near magnetic equator) which seems the effects due to geology. By doing so, the regional field effect can be removed from observed magnetic data and the remaining field may represent the residual field.

The tilt angle derivatives are the (tilt) angles θ (in radians) between total horizontal derivative and vertical derivative of total magnetic intensity (Verduzco et al, 2004).

$$\theta = \tan^{-1}\left(\frac{\frac{\partial B}{\partial z}}{\frac{\partial B}{\partial h}}\right) \quad \text{.....3.4}$$

where the total horizontal derivative is $\frac{\partial B}{\partial h} = [\left(\frac{\partial B}{\partial x}\right)^2 + \left(\frac{\partial B}{\partial y}\right)^2]^{1/2}$

Total horizontal derivative, $\frac{\partial B}{\partial h}$ provides an effective procedure for separating shallow and deep magnetic sources and enhancing the visualization of linear features.

Tilt angle derivative that applied to total filed magnetic data or residual field data use to enhance near surface geological features and mapping shallow basement structures and mineral exploration targets (Frantisek H. et al, 2009 and Reynolds et al, 1990).The tilt angle is restricted to lie between +90 ^{0}and -90^0 regardless of the amplitudes of the vertical and horizontal derivatives. It has the attractive property of being positive over the sources, crosses through zero at or near the edge of a vertical side source and is negative outside the source region. (Salem A., et al, 2007).

3.2 Electrical Methods

3.2.1 Electrical Resistivity Methods

Typically, current (I) is induced between paired electrodes (C_1, C_2) and the potential difference (ΔV) between paired voltmeter electrodes P_1 and P_2 is measured. Apparent resistivity (ρ_a) is then calculated (based on I, ΔV and electrode array configuration factor). If the current electrode spacing is expanded about a central location, a resistivity depth

sounding can be generated. (Neil, A,. and Neil, C., 2008). Electrical methods are based on the study of natural and artificial electromagnetic fields injected into the ground. In electrical prospecting, subsurface bodies are studied based on active or passive conductors electricity. Electrical resistivity methods (eg.VES), electrochemical methods (eg. SP and IP), electromagnetic methods, magneto telluric methods and radio wave methods are grouped into electrical methods of prospecting. Electrical resistivity (ρ) /conductivity (ρ=1/σ) are properties that characterizes the ability of rocks to resist / conduct (transmit) electric current when a voltage is applied. Resistivity of rocks is expressed in (Ω.m), and conductivity (1/Ω.m). Electrical resistance is proportional to length (L) and cross-sectional area of the material "A", that given as $R = \rho \frac{L}{A}$. From Ohm's law (Figure 3.4, resistance is giving as $R = \frac{V}{I}$. The resistivity of the medium can the given as

$$\rho = \frac{VA}{IL}(\Omega.m). \quad \text{..... (3.14)}$$

As the electric field strength (E) can give as the potential gradient as; $E = \frac{V}{L} \Rightarrow V = E.L$ and current density (J) as $\left(\frac{I}{A}\right)$.Further using $V = E.L$ and $J = \frac{I}{A}$ the expression for resistivity can be given which can a ρ (Ω.m) =E (v/m)/J (A/m2)(M.H.Loke, 2001).
or J = σE.....(3.15)

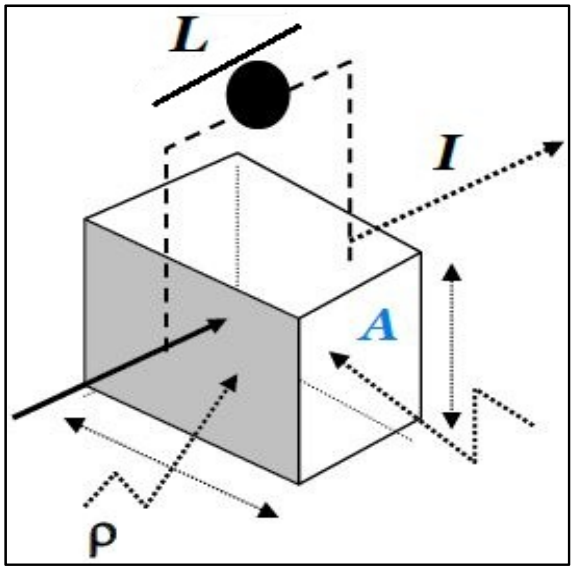

Figure 3.4: Demonstration of Ohm's law

In practice, what is measured is the electric field potential. We note that, in geophysical surveys the medium resistivity ρ, which is equals to the reciprocal of the conductivity ($\rho=1/\sigma$) is more commonly used. The relationship between the electric potential and the field intensity is given by $E= -\nabla \phi$ ..... (3.16)

for ϕ is field potential used to give V for the volume. Combining equations (3.15) and (316), we get $\mathbf{J} =-\sigma\nabla \phi$ ..... (3.17)

In almost all surveys, the current sources are in the form of point sources. In this case, over an elemental volume ∇V surrounding the a current source I, located at ($x_s.y_s.z_s$) the relationship between the current density and the current (Dey A and Morrison 1979a)is given by: $\nabla.V= \left(\frac{I}{\Delta V}\right)\delta(x-x_s)\delta(y-y_s)\delta(z-z_s)$ ..... (3.18)

where, **δ** is the Deric Delta function. Then, equation 3.17 can rewrite as: $-\nabla.[\sigma((x,y,z)\nabla \phi (x,y,z)] = \left(\frac{I}{\Delta V}\right)\delta(x-x_s)\delta(y-y_s)\delta(z-z_s)$ .....(3.19)

This is the basic equation that gives the potential distribution in the ground due to appoint current source. A number of techniques have been developed to solve this equation. This is the "Forward" modeling problem, i.e. to determine the potential that would-be observed over a given subsurface structure. Fully analytical methods have been used for simple cases, such as a sphere in a homogenous medium or a vertical fault between two areas each with a constant resistivity. Considering a homogeneous subsurface and a single point current source on the ground surface as in figure 3.5a. In this case, the current flows radially away from the source, and the potential varies inversely with distance from the current source. The equipotential surfaces have a hemisphere shape, and the current flow is perpendicular to the equipotential surface.

The potential in this case is given by: $\phi = \frac{\rho I}{2\pi r}$ ..... (3.20)

where "r" is the distance of a point in the medium from the electrode.

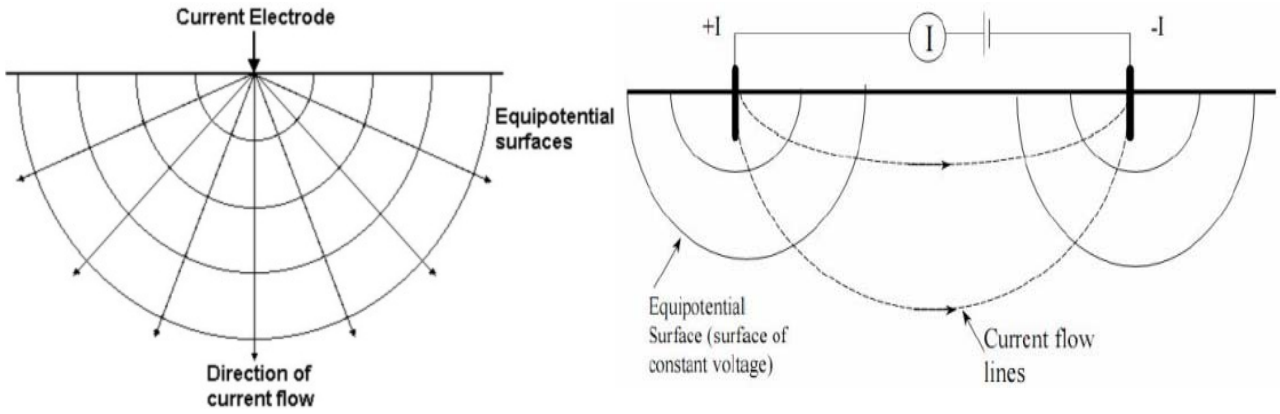

Figure 3.5: The potential distribution due to: a point current source (a) and due to pair of current electrodes (b)

However, for all resistivity surveys at least two current electrodes are required to serve as a current source and sink as in figure 3.5b that show the potential distribution caused by a pair of current source. The potential value in the medium at any point "P" due to such a pair is given by:

$$\phi = \frac{\rho I}{2\pi}\left(\frac{1}{r_{+I}} - \frac{1}{r_{-I}}\right) \quad \text{..... (3.21)}$$

where '**r**' is the distance between the point "P" in the medium and the electrode. $r_{+1}$and r_{-I} are distances of the point from the first and second current electrodes.

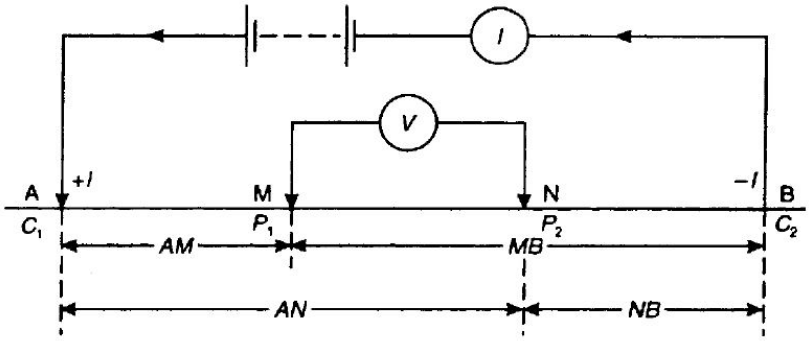

Figure 3.6: Generalized form of electrode configuration in resistivity survey. (John M.Reynolds, 1997)

For a current source and sink, the potential V_p at any point "P" in the ground is equal to the sum of the voltages from the two electrodes, such that :$V_p = V_A + V_B$ where V_A and V_B are the potential contributions from the two electrodes, A(+I) and B(-I). The potential at electrodes M and N (according to equation 3.21) are:

$V_M = \frac{\rho I}{2\pi}\left[\frac{1}{AM} - \frac{1}{MB}\right], V_N = \frac{\rho I}{2\pi}\left[\frac{1}{AN} - \frac{1}{NB}\right]$. Then the potential difference (ΔV) between M and N can be rewritten as: $\Delta V = V_M - V_N = \frac{\rho I}{2\pi}\left\{\left[\frac{1}{AM} - \frac{1}{MB}\right] - \left[\frac{1}{AN} - \frac{1}{NB}\right]\right\}$. Rearranging this to get resistivity (ρ) as: $\rho = \frac{2\pi\Delta V}{I}\left\{\left(\frac{1}{AM} - \frac{1}{MB}\right) - \left(\frac{1}{AN} - \frac{1}{NB}\right)\right\}^{-1}$ ..... (3.22)

Equation 2.23 can be written as: $\rho = K\frac{\Delta\phi}{I}$ where, K= $\frac{2\pi r}{\left[\frac{1}{AM} - \frac{1}{MB}\right] - \left[\frac{1}{AN} - \frac{1}{NB}\right]}$ is a geometric factor that depends on the arrangement of the four electrodes.

This calculated resistivity value is not the true resistivity of the subsurface, but an apparent value that is the resistivity of a homogeneous ground that will give the same resistance value for the same electrode arrangement. The objective of modern electrical resistivity surveys is to obtain true resistivity models for the subsurface which have a geological meaning. To determine the true subsurface resistivity from the apparent resistivity values is the inversion problem. (Reynolds, J.M. (1997)

There are two standard procedures in resistivity surveying work known as resistivity profiling and resistivity sounding. Resistivity profiling which is also known as lateral inhomogeniety hunting is used to obtain the information on lateral variation in resistivity. This method is achieved by keeping the separation between the electrodes fixed and moving all the electrodes on the surface along selected survey lines to map vertical and near vertical contacts between rock formation and weak zones like faults, fractures and fissures. Resistivity sounding which is also known as Vertical Electrical Sounding (VES) is used to determine the variation in resistivity in the vertical direction and to outline the boundaries between horizontal horizons in stratified medium. It is achieved by symmetrically expanding the distance between the current electrodes (Figure 3.7) about a point called the sounding point. (Philip Kearey et al, 2002).

3.2.2 Electrode Arrays

Although many configurations of electrodes have been designed, only few (Schlumberger, Wenner and dipole-dipole configuration) are in common use.

The apparent resistivity values observed by the different array types over the same structures can be very different. This is because the apparent resistivity depends on the geometry of the electrode array used. The choice of a particular array depends on a number of factors including: the geological structures to be delineated and heterogeneities of the subsurface. In other way, the sensitivity of the array to vertical and lateral variations for resistivity, its depth of investigation and horizontal coverage and signal strength of the array are the factors that have to consider in resistivity survey.

3.2.2.1 Dipole-Dipole array

In a dipole-dipole array (figure 3.8), the distance between the current electrodes **A** and **B** (current dipole) and the distance between the potential electrodes **M** and **N** (measuring dipole) are significantly smaller than the distance (**r**) between the centers of the two dipoles. The potential electrodes (**M & N**) are outside the current electrodes (**A & B**).

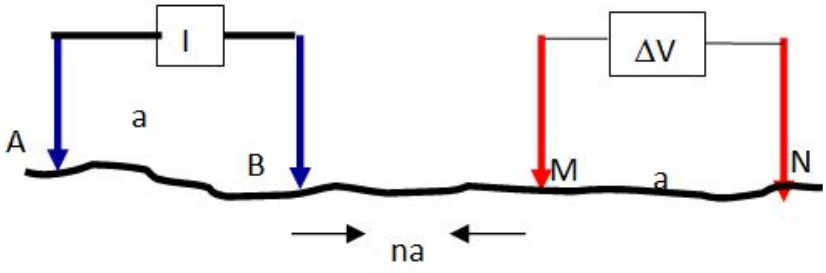

Figure: 3.7 Dipole-Dipole array electrode configurations

K = πn (n+1) (n+2) a: is geometric factor and then apparent resistivity is given as:

$$\rho_a = \pi n(n+1)(n+2)a\,\frac{\Delta\phi}{I} \quad \text{……………………………… (3.23)}$$

3.2.3 Electrical properties of earth materials

Electric current flows in earth materials at shallow depths through two main methods that are known as electronic conduction and electrolytic conduction methods. In electronic conduction, the current flow via free electrons, such as in metals. In electrolytic conduction, the current flow via the movement of ions in groundwater. Electronic conduction is important when conductive minerals such as metal sulfides and graphite are present. In general, resistivity of a material is most dependent on the water saturation, the presence of dissolved salts, and the connectivity of pore space. It is one of the most variable material properties,

with values ranging from 10^{-8}Ω-m for native silver and 1016 Ω-m for pure sulfur. Sedimentary rocks have low resistivity values due to their high fluid content, while igneous and metamorphic rocks tend to have the highest resistivities. Most rock-forming minerals, including quartz and mica, are highly resistive insulators; unconsolidated sediments and clayey soil are more conducive to current. It is not possible to identify rock type solely on the basis of resistivity data. As shown in table 3.1 (Sara Michelle Monahan, 2013).

Table 3.1: Resistivities of common rocks and ore minerals (Rosli.S. et al, 2012)

Rock type	**Resistivity (Ohm-m)**	**Ore types**	**Resistivity (ohm-m)**
Topsoil	50–100	Pyrite (ores)	0.01–100
Loose sand	500–5000	Pyrrhotite	0.001–0.01
Gravel	100–600	Chalcopyrite	0.005–0.1
Clay	1–100	Galena	0.001–100
Weathered bedrock	100–1000	Sphalerite	1000–1 000 000
Sandstone	200–8000	Magnetite	0.01–1000
Limestone	500–10 000	Cassiterite	0.001–10 000
Greenstone	500–200 000	Hematite	0.01–1 000 000
Gabbro	100–500 000		
Granite	200–100 000		
Basalt	200–100 000		
Graphitic schist	10–500		
Slates	500–500 000		
Quartzite	500–800 000		

3.2.2 Induced Polarization

Induced polarization is a geophysical imaging technique used to identify the electrical chargeability of subsurface material. Consider a standard case of resistivity survey, at which the current "I" is injected in to the ground by means of two current electrodes and the resulting potential difference between potential electrodes are measured. If the current is abruptly switched off, the voltage between the potential electrodes does not drop to zero immediately. After a large initial decrease (Figure 3.9) the voltage suffers a gradual decay and can take many seconds to reach a zero value. A similar phenomenon is observed as the current is switched on. After an initial sudden voltage increase the voltage increases gradually over a discrete time interval to a steady-state value.

The ground thus acts as a capacitor and stores electrical charge, that is, becomes electrically polarized. IP/Resistivity induced potential is thus, a potential difference that sometimes exists briefly after the current in a resistivity array has been switched off. (Alan E. Mussett, et al, 2000).

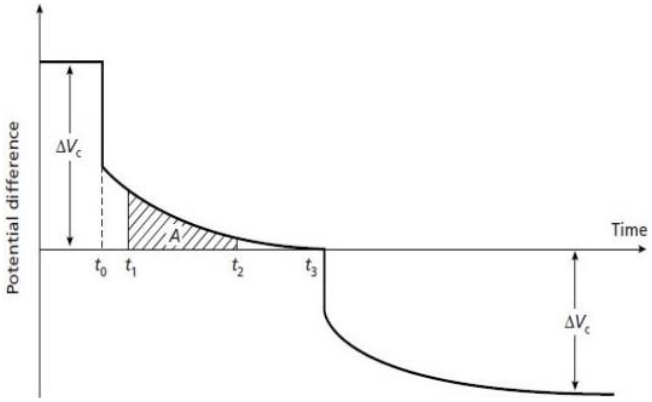

Figure 3.8: The phenomenon of induced polarization.

At time t_0, the current is switched off and the measured potential difference, after an initial large drop from the steady-state value ΔV_c, decays gradually to zero. A similar sequence occurs when the current is switched on at time t_3. "A" represents the area under the decay curve for the time increment t_1-t_2.

3.2.2.1 Mechanisms of Induced Polarization

There are two main mechanisms of rock polarization and three main ways in which polarization effects can be measured.

3.2.2.1.1 Electrode Polarization

In rocks other than ores, current is conducted by positive and negative ions moving through the groundwater, often in tiny channels formed of interconnecting pores as in (Figure 3.9). If a channel is blocked by a grain that is insulating, no current can flow through it, but if the grain is conducting electrons can pass through, though ions cannot. Negative ions reaching the blockage will lose electrons and become electrically neutral; the electrons pass rapidly through the grain to its other side, where they are available to combine with positive ions coming to the blockage from the opposite direction.

Because the exchange of electrons to and from ions is relatively slow there is a 'queue 'or buildup of ions on each side of the grain, forming a small accumulation of charge the rock behaves similarly to an electrical capacitor. When the current is switched off these charges disperse through the pore water and briefly produce a small current; as a result, the potential difference between the potential electrodes does not fall immediately to zero, as it would in a rock without ore grains. This buildup of ions is called electrode polarization.

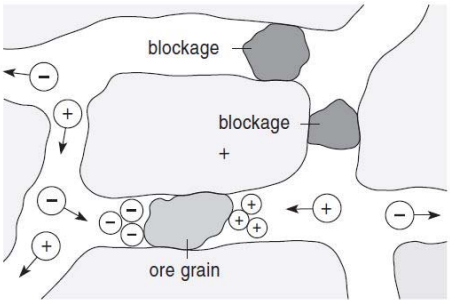

Figure 3.9: Microscopic pore channels in rocks (Alan et al., 2000).

3.2.2.1.2 Membrane Polarization (electrolytic polarization)

The second mechanism of IP is, due to clay particles along the sides of the narrow pores. Negative charges that normally exist on their surfaces are in contact with the pore water, and these tend to attract positive ions when electric current flows past (figure 3.10).These small accumulations of charge also disperse and produce a small current when the current is switched off. This membrane polarization, fortunately, is generally only a fraction of the potential due to electrode polarization but may act as background 'noise' when surveying for ores.

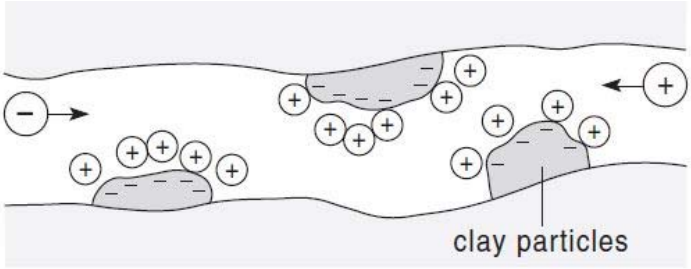

Figure 3.10: Membrane polarization. (Philip Kearey, 2002)

3.2.2.2 Induced Polarization Measurements

There are two types of IP data measurement: frequency domain and time domain. Frequency domain IP data are generated by comparing the apparent resistivities determined for two variable frequency input currents. Time domain data are generated by measuring rate of decay of the measured potential difference after current flow is terminated. IP measures the capacitive properties of the ground, and is used to qualitatively–quantitatively estimate the concentration-distribution of clay or metallic mineralization. (Neil Anderson et al., 2008). IP effect measurements involve the monitoring of the decaying voltage after the current is switched off. The most commonly measured parameter is the chargeability **M**, defined as the area **A** beneath the decay curve over a certain time interval (t_1–t_2) normalized by the steady-state potential difference ΔV_c (Figure 3.8).

$$M = \frac{A}{\Delta V_c} = \frac{1}{\Delta V_c}\int_{t_1}^{t_2} V(t)dt \quad \text{..... (3.10)}$$

Chargeability is measured over a specific time interval shortly after the polarizing current is cut off (figure 3.8).The area A is determined within the measuring apparatus by analogue integration. Different minerals are distinguished by characteristic chargeability, for example pyrite has M = 13.4 ms over an interval of 1 s, and magnetite2.2ms over the same interval. In time domain IP the chargeability, is usually given in millivolt per volt (mV/V) or in milliseconds. (Mark E. Everett, 2013).

Table 3.2shows the IP values (in terms of mV/V) for several mineralized rocks and common minerals. IP effect due to sulfide mineralization (the electrode polarization effect) is much larger than that of due to clay minerals (membrane polarization) in sandstone and siltstones.

Table 3.2: The IP Values for some rocks and minerals (After M.H.Loke, 2001)

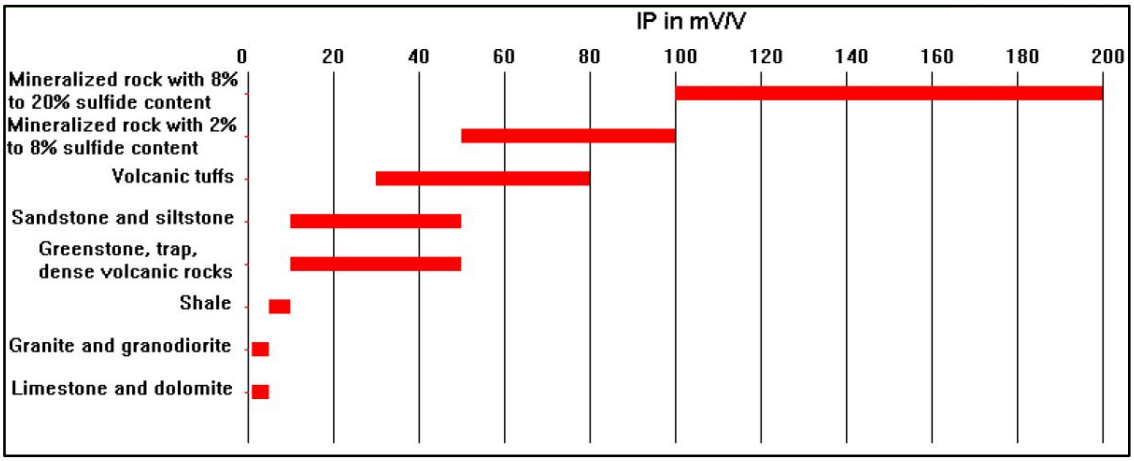

3.3 Radiometric Survey

Radiometric method is one of the static geophysical methods originated from spontaneous disintgration of unstable radioactive nuclei. This disintegration results high energy of atomic particles radiation from natural breakdown of isotope of U, Th and K elements into other stable elements. The rate of disintegration or breaking of radioactive nucleus is proportional to the total number of molecules $\mathbf{N_t}$ at a particular time't' and the intensity of γ- radtion decreases exponentially according to decay equation: $N_t = N_o e^{-\lambda t}$ ..... 3.11 where, N_0 is the number of isotope material present at time t=0, N_t is number of isotope material at time t = t, and λ is a decay constant. There are three characteristic types of radiation that are emitted in radioactive decay: α-radiations the one with less penetrating energy as it pass through matter and highly absorbed by the crystal to produce large number of emission electrons. β–radiations are more penetrating than alpha particles, and can travel up to a meter in material media while,γ–radiations have strong penetrating energies, less absorbed by scintillation crystal and less electron emission from the crystal. Modern instrument, (Gamma ray spectrometer) have been used to differentiate between the radiations from U, Th and K, according to their energy spectra (Figure 3.11)

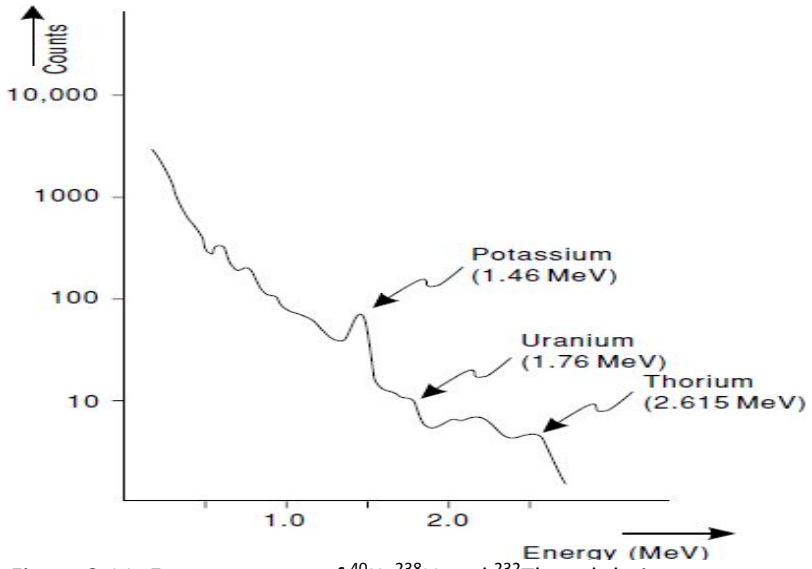

Figure 3.11: Energy spectra of ^{40}K, ^{238}U and ^{232}Th and their measurement windows (Charles J. Moon, 2006)

Spectrometers are designed to detect radiation energies using NAI (TI) crystal to identify the presence of the natural radio elements which gives rise to photons of light that are converted to electrical pulses by photomultiplier tube (Durrance, E. R.1986).Most of the gamma ray radiation in the Earth is originated from the decay of three radioactive isotopes, namely:

- Potassium (K^{40}), with a half-life of $1.3x10^9$ years;
- Daughter products of ^{238}U decay series/Uranium (Bi^{214}), with a half-life of $4.4x10^9$ years, and
- Daughter products of the ^{232}Th series /Thorium (Th^{208}), with a half-life of $1.4x10^9$ years.

In principle, all rocks contain trace of radioactive elements with different abundance. Rocks containing large amount of radioactive minerals (table 3.3) are detected by high radiation count or vice versa**.**

Table 3.3: More common radioactive minerals (Charles J. Moon et al, 2006)

Radioisotope	Minerals	Occurrence
Potassium	Orthoclase and microcline feldspars [KAlSi3O8]	Main constituents in acid igneous rocks and pegmatites
	Muscovite [H2KAl(SiO4)3]	Main constituents in acid igneous rocks
	Alunite [K2Al6(OH)12SiO4]	Alteration in acid volcanics
	Sylvite, carnallite [KCl, MgCl2.6H2O]	Saline deposits in sediments
Thorium	Monazite [ThO2 + rare earth phosphate]	Granites, pegmatites, gneiss
	Thorianite [(Th,U)O2]	Granites, pegmatites, placers
	Thorite, uranothorite [ThSiO4 + U]	Granites, pegmatites, placers
Uranium	Uraninite [oxide of U, Pb, Ra +Th, rare earths]	Granites, pegmatites and with vein deposits of Ag, Pb, Cu, etc.
	Carnotite [K2O.2UO3.V2O5.2H2O]	Sandstones

Gamma-ray methods have wide application in searching for Uranium deposits, exploration for rare metals, lithological mapping, age determination for geological formations and environmental monitoring (Yiheyse Kebede et al., 2000).

3.4 Remote Sensing

3.4.1 Advanced Space Borne Thermal Emission and Reflection Radiometer (ASTER)

Satellite remote sensing images have been widely and successfully used for mineral exploration since the launch of Land sat in 1972. This application relies mostly on the capability of the sensor to register spectral signatures and other geological features related to mineral deposits. Iron is one of the most important mineral commodities that have been searched with the use of satellite remote sensing images. It can be detected by remote sensor, based on its spectral signature. The Advanced Space borne Thermal Emission and Reflection Radiometer (ASTER) sensor measures reflected radiation in VNIR, SWIR and TIR electromagnetic energies. The instrument consists of three separate subsystems with a total of 14 bands. VNIR contain three bands (B1, B2 and B3) between 0.52 and 0.86 μ m, SWIR contain six bands (B4-B9) from 1.6 to 2.43 μ m with spatial resolution of 15m and 30m respectively. Thermal Infrared (TIR) contains five bands (B10-B14) between 8.1 and11.6 μ m with 90 m spatial resolution. (Carlos A. Torres (www.utsa.edu), accessed, April, 2017)

CHAPTER IV

4. Geophysical Data Acquisitions, Processing and Presentation

4.1 Magnetic Method

4.1.1 Instrumentation and Data Acquisition

A Scintrex made (IGS-2) with proton precession MP-4 sensor (Figure 4.1) that measure total earth's magnetic field (T) was employed. It has three modes of operations; total field, gradiometer and base station mode. The total field mode, which is used in this survey, has an operating range of 2000 nT to 100,000nT with an absolute accuracy of 62nT at 100000nT and 1nT accuracy at 50000nT. It has a resolution of 0.1 nT and a 2 second reading time. The IGS-2/MP-4 sensor was mounted on a back harness (Figure 4.2) and is oriented in such a way that the "equatorial region up" arrow imprinted on it points as required by the geographic location of the survey area. The tuning field was set at 35,000 nT at the start. However, fluctuations of the field necessitated changing the tuning field from place to place.

Figure 4.1: IGS-2/MP-4 proton precession magnetometer

Magnetically quite place was established at about 100w from one side of the site as base station on which repeated measurements was taken at the beginning and end of each working day in order to make corrections for the diurnal magnetic field variations. Magnetic data were collected on a systematic grid of 100 m profile and 20 m station interval that prepped using hand held Garmin GPS with ±3m accuracy.

Coordinates are collected for each station in Adindan/UTM 37N projection. (Scintrex,1986 and Scintrex, 1986). During field data acquisition, all ferrous materials were removed from the vicinity of station points.

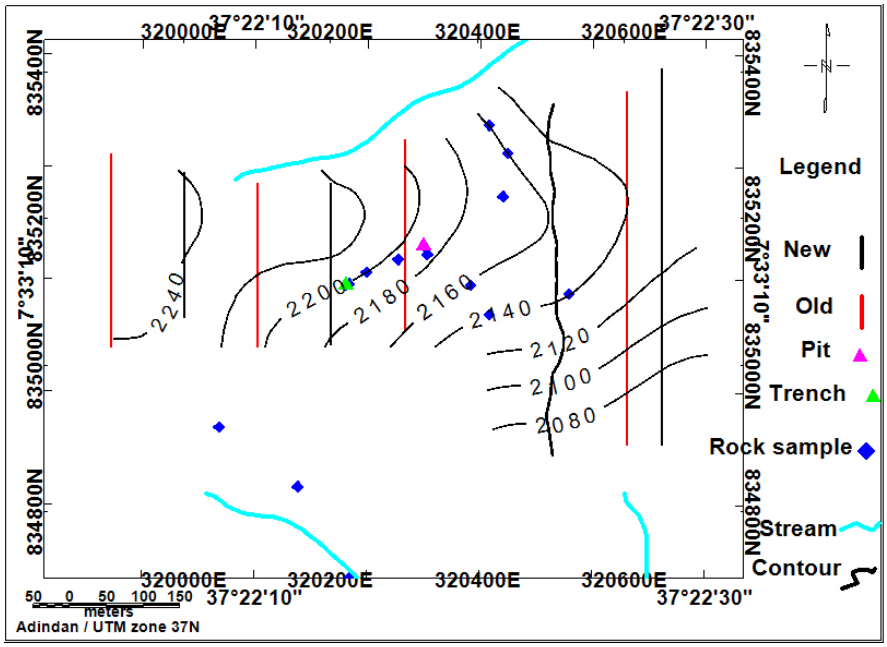

Figure 4.2: Magnetic survey: (a) Field data acquisition process (b) profile information

A total of about 134 magnetic data with 100mx20m grid has been obtained as in figure 4.2b. The magnetic data obtained for this thesis work were collected by researchers and the Geological Survey of Ethiopia.

4.1.2 Data Processing and Presentation

Data recorded from the instrument in site, were entered into computer using spreadsheet software for post survey processing and interpretation. To produce the magnetic anomaly of an observation points, diurnal correction according to equation (4.1) was applied to total field (B_T) that collected by the magnetometer. This correction is essential to remove the noise due to external factor and used as if all reading were taken at same time. Resulting corrected (G_c) field that is known as total magnetic field was smoothed, gridded and contoured to present as total field map.

$$G_c = G_i - \left[\left(\frac{G_2 - G_1}{T_2 - T_1}\right)x(t_i - T_1)\right] - (G_f - G_1) \quad \text{..... (4.1)}$$

Were, G_c, G_1, G2, and G_i are corrected magnetic field, the first magnetic field reading at the base station at time (T_1), the second magnetic field reading at the base station at time (T_2), the observed magnetic field at each station along the profile at time (t_i) and G_f is the reference field is the first day base station reading during time T_1 respectively. Additional data correction and filtering techniques were applied to diurnally corrected field data to extract more information from field data. By doing so, causes of magnetic variation other than those arising from the magnetic effects of the subsurface (rock magnetism) were removed step by step.

The resulting compiled magnetic data were then gridded using minimum curvature gridding system. Following the gridding techniques, total magnetic anomaly map (Figure 5.1) and total magnetic anomaly profile map (Figure 5.2) were produced. To extract maximum information from the total field, some filtering techniques were applied to the diurnally corrected magnetic total field data. Accordingly, Analytic signal and Tilt angle derivative were applied to observed data. Moreover, the residual anomaly field was separated from the estimated regional. All those processing were performed by using Oasis Montaj mapping and processing and excel spread sheet software and, the results are presented in contour map as in figure 5.3 and 5.5

4.2 Induced Polarization

4.2.1 Instrumentation and Data Acquisition

TSQ-2 transmitter, IP-R-12 time domain receiver, non-polarizing porous pots, stainless steel stakes with all IP unit accessories were used for IP/Resistivity survey. Time Domain Induced Polarization/Resistivity meter is seven channel receivers and automatically calculates parameters for latter data retrieval and processing. It averages primary voltage (VP), Self-Potential (SP) and individual transients (Mi) continuously (Scientrex, 1993).

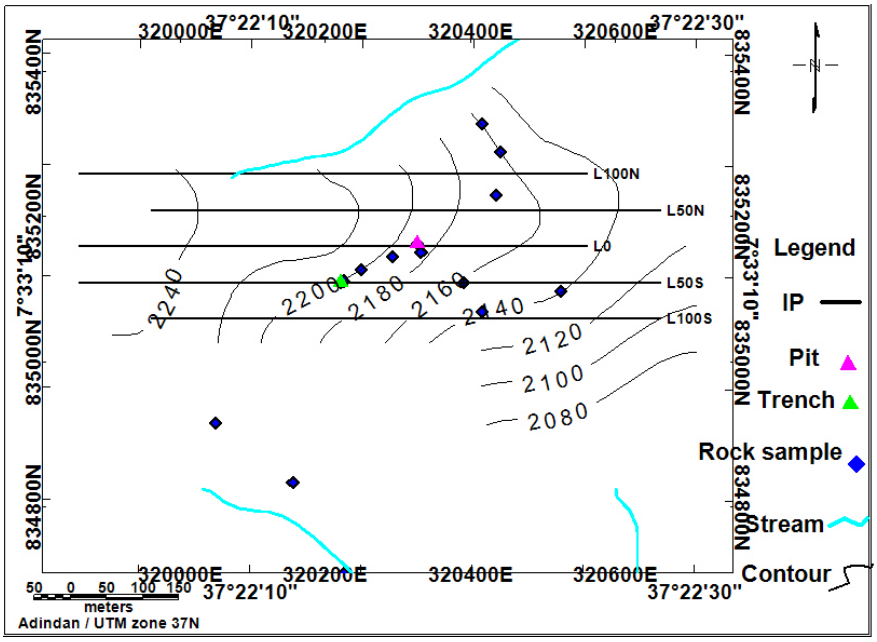

Figure 4.3: IP unit (transmitter, receiver etc. (a) IP data profile lines (b)

IPR-12 time domain receiver records signal simultaneously from 8 dipoles. The receiver can records individual windows from 4th to 14th chargeability slice, in this work the data representing the average chargeability slice of all windows. IPR-12 automatically calculates the average chargeability (M_x) and apparent resistivity (ρ_a) parameters and store data in soild-state memory that could be dumped to computers. A dipole-dipole electrode arrangement (Figure 4.3) was employed for transmitting an electric current to the ground using current electrodes (A and B) and TSQ-2E transmitter with a motor generator.

In order to measure chargeability and potential difference between the two receiving electrodes (M and N), seven non polarized porous pots are filled with a copper sulphate solution and placed sequentially into a small pit dug out at each station. These are connected to IPR-12 receiver to measure the potential difference between them. During the field survey, a two second off and two second on square wave signal was transmitted to the ground and an averaged slice chargeability values were recorded at every pickets of 20 m apart along all the profiles. The whole arrangements are moving forward together keeping constant separation of 20m between neighboring electrodes. The center of the two dipoles (i.e the midpoint between consecutive current electrodes and potential electrodes) is a plotting point (**P.P**) along the profiles

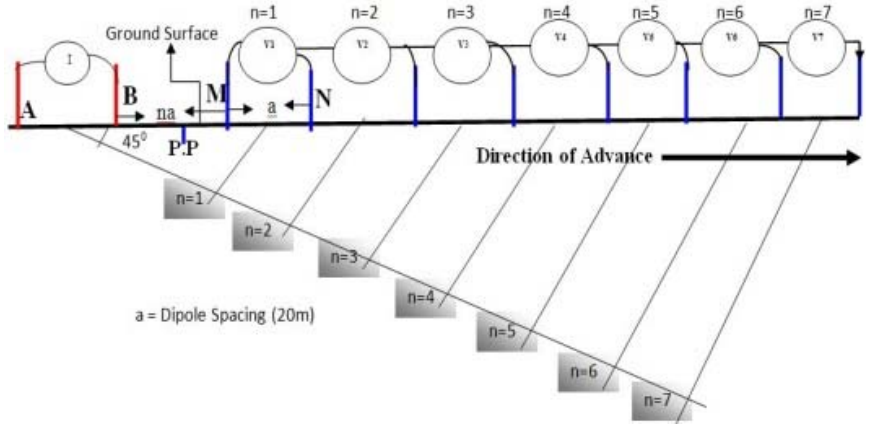

Figure 4.4 Dipole-dipole array electrode configuration (a) and IP data collection (b)

4.2.2 Data Processing and Presentations

IP/Resistivity data processing was started early during field data acquisition by checking and removing or taking repeated measurements when the signal to be measured become too small. This field data reduction and inspection process was based on the values of chargeability, resistivity and their corresponding standard deviation calculated for the user defined chargeability between 310-450ms. Root mean square deviation is expressed in % and is calculated using equation (3.5).

$$RMS\% = \left\{ \frac{1}{wi} \sum_{1}^{wi} \left(1 - \frac{Mi}{Mic} \right)^2 10^4 - \right\}^{1/2} \quad \text{..... (3.5)}$$

where, w_i: number of slices which are included in cole-cole parameter calculation

M_i: values of measured chargeability

M_{ic}: corresponding values of the 'best fit' master curve chargeability. Any data with standard deviation greater than 15% was discarded (Girma Woldetinsae et al., 2006)

As IPR-12 receiver automatically calculate the average chargeability (M_x) and apparent resistivity (ρ_a) parameters and store data in soild-state memory, data were dumped to computer in daily base after field work. Spikes were removed from IP/R data using profile curves after data are dumped to computer and imported to geosoft data processing software. IP/R data are then, gridded, smoothed, and contoured using the same software. Profile map is produced for daily work for each line to extract relevant information by qualitative interpretation to help the next day survey process. As more and more profile lines are surveyed, plan (level maps) and stacked maps should be prepared to help the rest survey process. Accordingly, daily data processing and discussion were performed on the cause of IP/Resistivity anomalies. After the completion of the field work the whole data were dumped and presented by plotting stacked profiles on a base map. Processed IP/R data were presented as contour maps, pseudo section (for all profiles) maps; stacked maps and 2D inverted model maps. Furthermore, composite chargeability and apparent resistivity maps are prepared using the complementary colors of magenta, cyan and yellow. Plan maps for (n=1 to n= 6) have been plotted to inspect lateral variations of chargeability and resistivity at different depths. The RES2DINV program was used to produce 2D model of chargeability and resistivity for quantitative interpretation.

In this study, the average slice of the IP decay curve was used during data processing. The output of IP/R data processing gives true chargeability, resistivity, strike and depth of mineralized zone that help magnetic anomaly modeling.

4.3 Radiometric Method

4.3.1 Instrumentation and Data Acquisition

The gamma-spectrometric survey was conducted using the GAD-6 gamma-ray spectrometer with a GSP-4S sensor.GAD-6 is four channels, spectral stabilized gamma-ray analyzer that simultaneously measures the concentration of radioactive elements within survey area in terms of the total (TC), potassium (K), uranium (U) and thorium (Th) counts. It has three modes of operation: integral, differential unstripped and differential stripped mode (Scientrex, 1989).To ensure that GAD-6 accurately records the gamma radiation energies detected by the sensor, a calibration was performed using thorium-oxide calibration samples. However, this calibration is performed once per week and when changing sensors, daily energy calibration had been performed before starting measurements each morning by repeating small portion of the main energy calibration procedure according to the operational manual. The console is carried in front as shown in figure 4.6 while, the sensor is held in hand and kept on the ground or held at constant height during measurements. Stations were located by GPS with intervals of 20 meters. Total, potassium, uranium and thorium count readings in counts per 10s were acquired in the integral mode and recorded at each station along a profile.

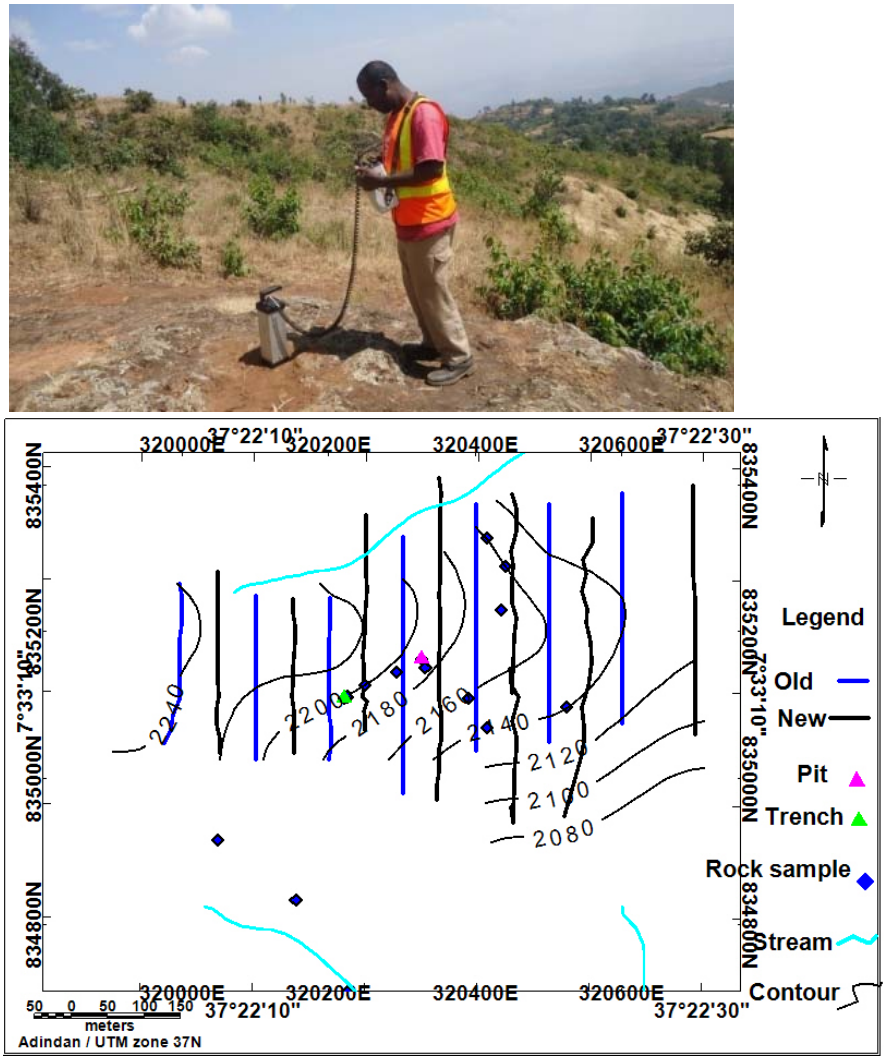

Figure 4.5: Radiometric field data acquisition (a) and data collection point (b)

4.3.2 Data Processing and Presentation

During field survey, the raw radiometric data was manually entered into a computer on a daily base using Microsoft excel spreadsheet software. As GAD-6 read all windows in count per 10 second, the serenading should be converting to conventional units of radioactive element concentration. Accordingly, the concentration of **K** was converted into percents while, the concentration for **U** and **Th** into equivalent ppm to define their concentration in rock unit. To convert cps to percent or equivalent ppm, the following relation for semi-infinite 2π geometry and GAD-6 window are used.

Potassium (**K**) = 3.4cps = 1%; for 1.38-1.56Mev window: (X_{cps}*1%)/3.4cps

Uranium (**U**) = 0.36cps = 1ppm; for 1.66-1.9Mev window: (X_{cps}*1ppm)/0.36cps) and

Thorium (**Th**) = 0.13cps = 1ppm for 2.44-2.77Mev window: (X_{cps}*1ppm)/0.13, where X_{cps} is the reading in cps for each channel (Scientrex, 1989).

Based on the above relation the concentration in percentage and parts per million (ppm) for the Potassium, Thorium and Uranium channels were computed. Radioelement ratio maps, (eTh/K, eU/K and eU/eTh) were also produced to inspect possible alteration zones and different lithologic units. Gridding, smoothing (using 3-pass hanning to enhance valuable surface information that can reflect the nature of the subsurface geology), and contouring were performed for Tc, K, U, Th and ratios using the Montaj Geosoft mapping system software. The composite and individual concentration maps of the area are presented in Ternary map and colored contour map using geosoft software.

CHAPTER V

5. Interpretations and Discussions

5.1 Magnetic Method

5.1.1 Qualitative Interpretation

The first hand interpretation in geophysical anomaly map is known as qualitative interpretation. It gives us the general meaning of the analyzed data in the form of maps and profiles and thus, they are interpretive. For magnetic data, qualitative interpretation involves a visual inspection of magnetic anomaly map and magnetic anomaly profiles which are prepared to recognize and delineate the major anomalies generating by underlying subsurface geological units. Meaningful geological information can be thus, inferred directly by looking at anomaly map and plotted anomaly profile without making any calculation.

5.1.1.1 Magnetic Total Field

Contour and profile maps (Figure 5.1 to 5.5) are used for this type of interpretation. Though, we have to process the magnetic total field before used it for lithological and structural interpretation, magnetic total field (Figure 5.1) seems to delineate the area in to three units of magnetic susceptibilities. The eastern central part that is characterized by higher anomaly values greater than 35272nT is attributed to basalt. Intermediate magnetic field values of (35000-35100nT) contrast were encountered at central to western part including mineralization zone. The intermediate anomaly at the western central is due to hematite iron ore. The higher susceptibility at south central and intermediate susceptibility at western central are supported by susceptibility measurement for rock samples from those locations. The northeast and southeast parts are characterized by low anomalies (<34990nT) which are associated to weak zones as in figure 5.1.

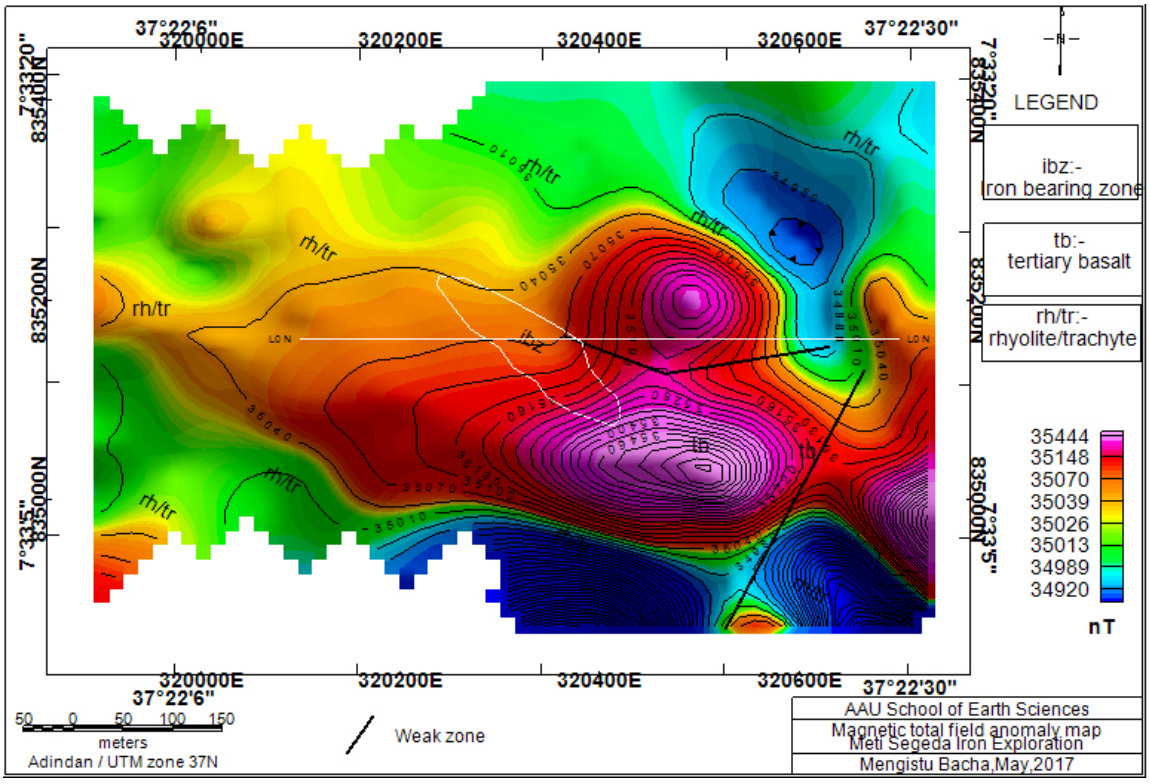

Figure 5.1: Magnetic total field map

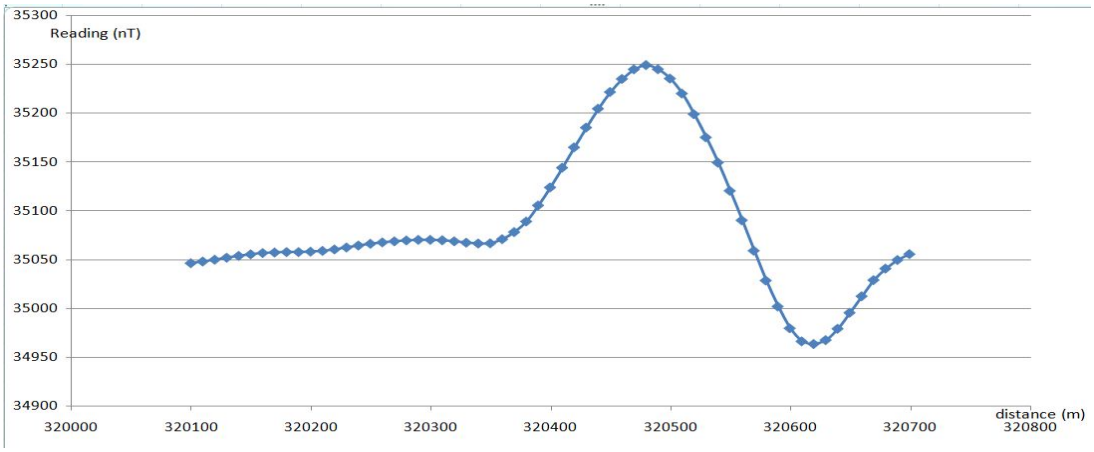

Figure 5.2: Magnetic total field central EW profile (white line)

5.1.1.2 Residual Field Anomaly

Observed magnetic field is the sum of fields produced by all subsurface sources. The target for specific surveys are often small-scale structure at shallow depths, and the magnetic responses of these targets are embedded in a regional field that rises from magnetic sources that are larger or deeper than the targets or located farther away. Correct estimation and removal of the regional field from observed field gives the residual field produced by the target sources. Interpretation and numerical modeling are carried out on the residual field data. According to Agocs, W. B., (1951), the regional field can be estimated by least-squares fitting a low-order polynomial to the observed field. So, here also the same approach was used to estimate the regional field which uses in turn was used to compute the residual anomaly field. Accordingly, the residual field (Figure 5.3) was produced using third order polynomials least square curve fitting

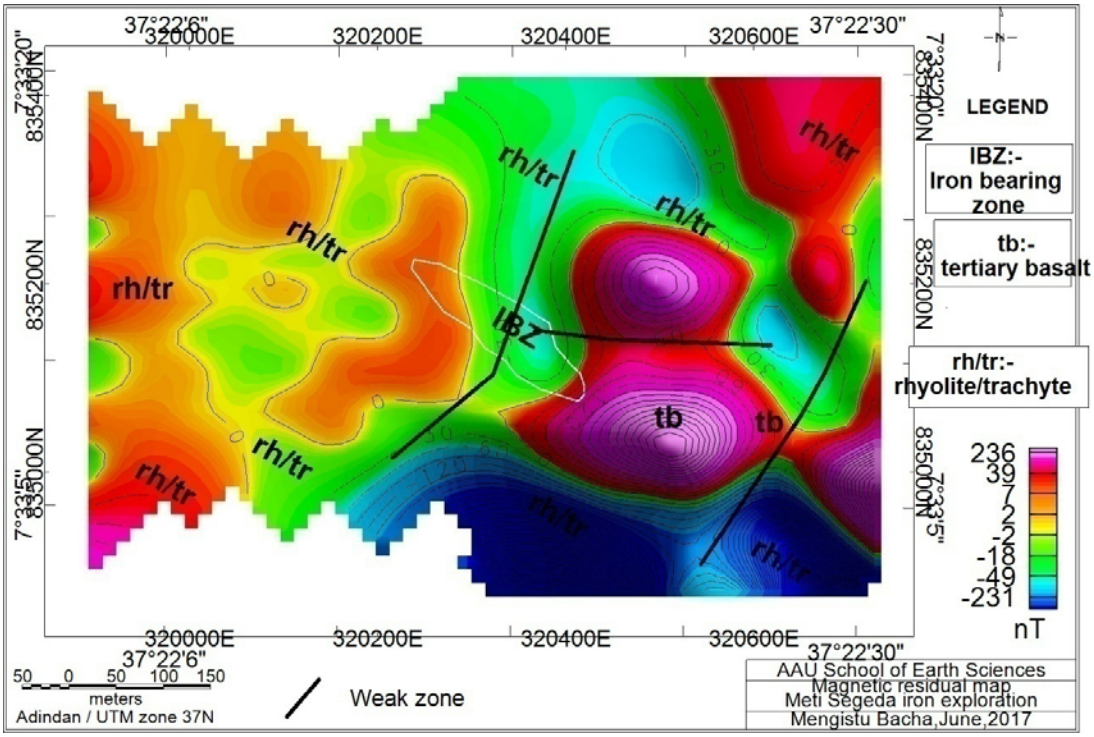

Figure 5.3: The residual field anomaly map

Higher anomaly values (>190nT) observed at the central east due to basalt rock unit. The western part of the area is observed with medium anomalies of values >56nT while, the south east side is characterized by low (negative) anomaly of values less than -314nT. Nearly north-south and east west weak zones are mapped by residual map. In addition to magnetic total field and residual field anomaly maps, the analytic signal and tilt angle derivative maps were produced for qualitative data interpretations. Analytic signal map (Figure 5.4) was produce to enhance shallow sources and contact zones by removing the dipolar nature of Earth's magnetic field (long wavelength anomalies which related to regional features) observed in magnetic total field. The analytic signal generates maximum anomalies (7nT/m) over the basalt at south east low magnetic response (<0.5nT/m) at northwest over rhyolite and trachyte flow. The enhanced analytic signal map that produced from total field, revealed weak zones and northeast to southwest contacts of geologic units. The contact between basalt and rhyolite is attributed to intermediate magnetic response of values between (0.5-6 nT/m).Analytic signal values are generally coincident with the magnetic anomaly peaks observed in the residual map of (Figure 5.4) and geological boundaries are clearer than in the total field. It sharpens individual anomalies within the high magnetic zone. In similar way as magnetic total field anomaly, mineralized zone lied in the area of intermediate magnetic anomaly. The central part of the area is characterized by intermediate magnetic response which is the effect of hematite iron ore in association with quartz.

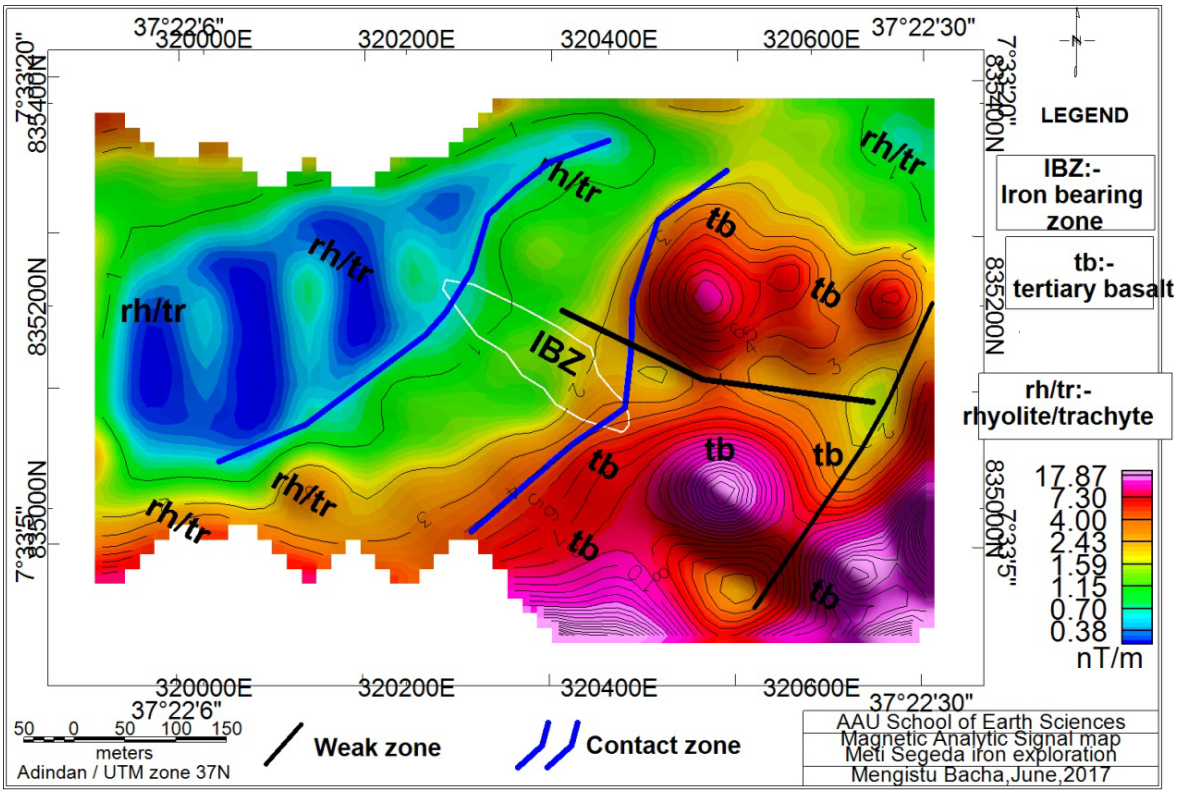

Figure 5.4: Analytic signal map

In order to increase the possibility to identify magnetic lineaments which are difficult to detect using total magnetic field and analytic signal maps, tilt derivative (Figure 5.5) was produced. Tilt derivative (equation 3.4) is the ratio of the vertical derivative to the absolute value of the horizontal derivative (Verduzco et al. 2004). Its value shows positive over magnetic source, cross through zero at or near the fault/contact locations and negative outside source zones. Tilt angle map was produced from analytic signal of residual field (Figure 5.5) for more detailed structural contacts mapping and identifying.

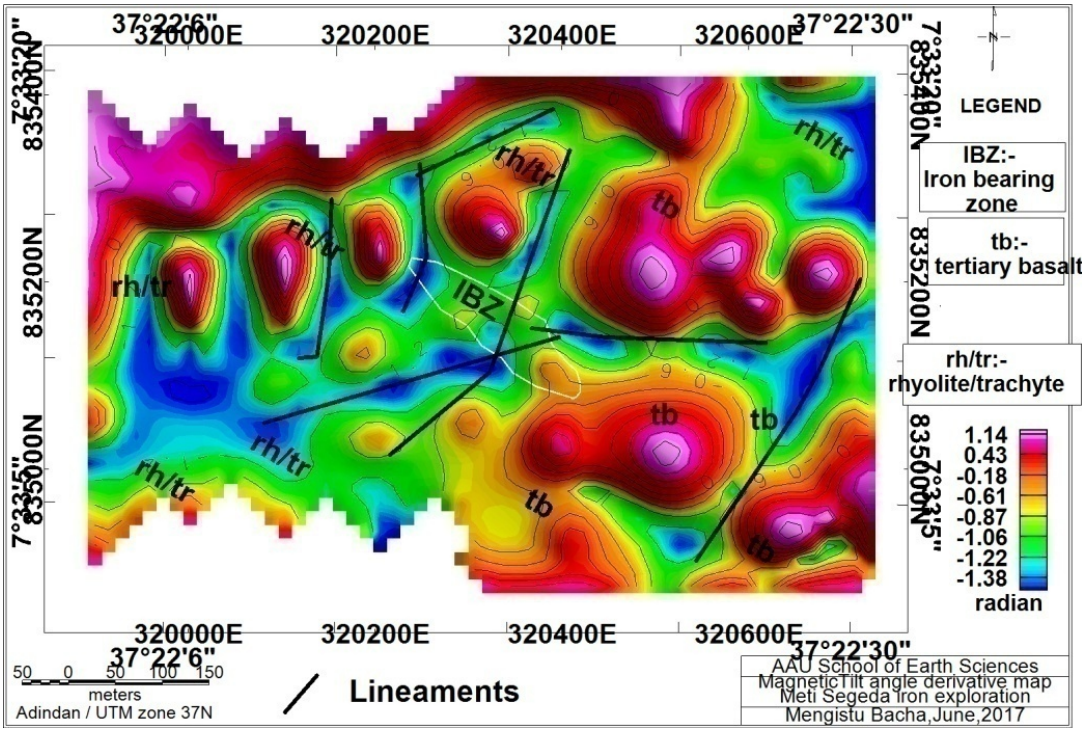

Figure 5.5 Tilt angle derivatives: from analytic signals.

Figure 5.5 revealed that, lineaments in the, NE-SW and nearly E-W directions. The intersection of lineaments indicates the mineralization. Generally, magnetic data was interpreted qualitatively to delineate the area into three lithologic units in addition to mapping structures that have association with mineralization.

5.1.2 Quantitative Interpretation

5.1.2.1 2 D Forward and Inverse of the Magnetic Data

To quantitatively interpret the magnetic data, the GM-SYS profile of Oasis Montaj software was used. It is used for calculating magnetic responses from a geologic cross section model. Forward modeling involves creating a hypothetical geologic model and calculating the geophysical responses to that model while, inverse modeling involves the reveres procedure. Starting with the observed geophysical response, an Earth model that will provide the best fit to that data is calculated.

The a priori information obtained from geology, Resistivity 2D inversion and VES and measured susceptibilities were used in GM-SYS to create hypothetical geological model of the sub surface for IP lin50N. An EW Profile was extracted from the residual grid (Figure 5.6) for numerical sub-surface modeling.

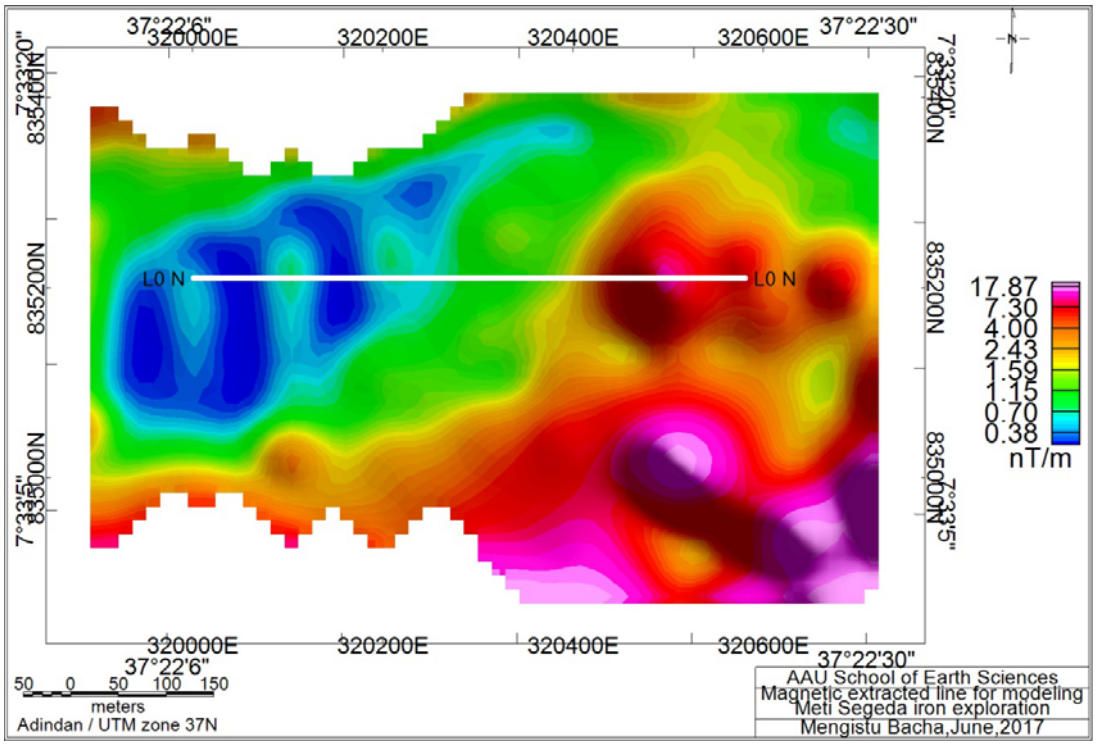

Figure 5.6: Extracted profile from analytic signal grid (white line)

Subsurface geology under extracted profile was modeled by using measured susceptibility, thin section information, inverted depth from IP/resistivity data and VES information as constraints. As a result from magnetic data, the subsurface units were modeled as rhyolite and basalt of different degree of weathering and iron bearing zone as in figure 5.7. Intermediately susceptible zone is obtained between basalt and rhyolite striking with depth of 105m and length of 200m.This result coincides with that of the iron bearing zone as revealed in model IP section of the same line.

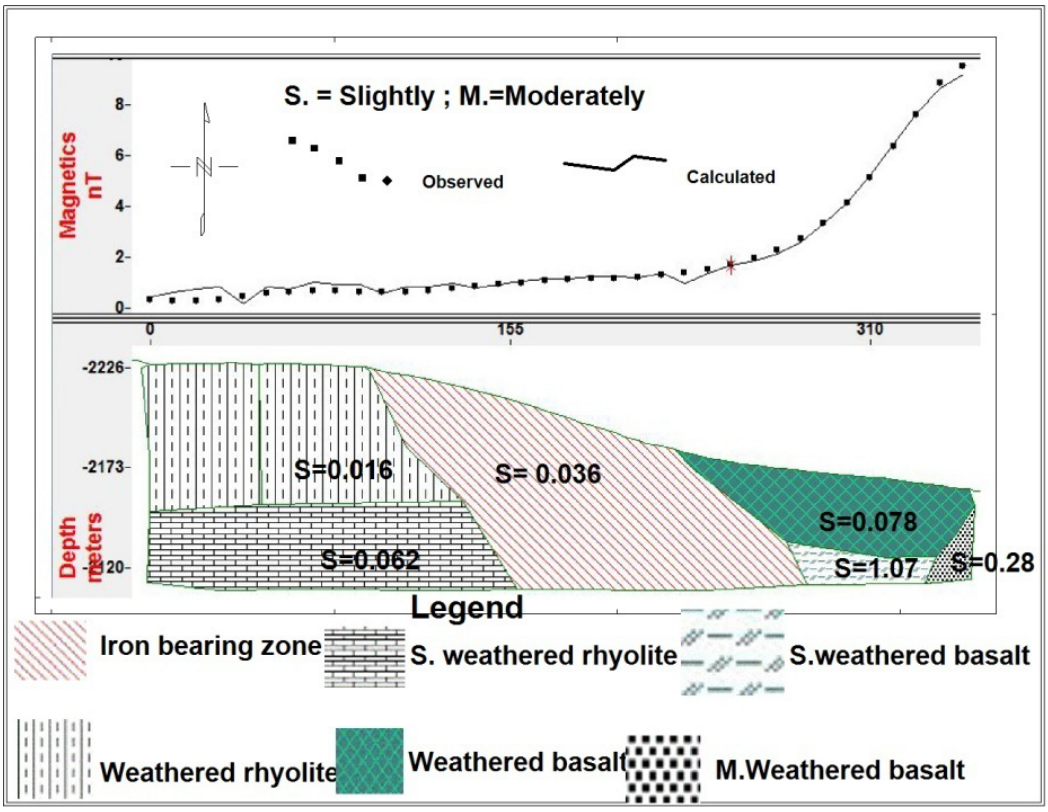

Figure 5.7: A model of subsurface under selected profile using magnetic data

5.1.2.2 Depth to Magnetic Source Bodies

To find the estimated location and depth to the top of the geologic sources produced by observed anomalies, 3D Euler deconvolution depth interpretation method were used. The Euler deconvolution process was carried out for the analytical signal grid of magnetic data using a structural index (defined as the degree of homogeneity). The depth solutions were obtained by inverting Euler homogeneity equation which relates magnetic field and its gradient components to the location of the source of an anomaly and to structural index. Depth solution for SI=0 (Figure 5.8) was selected for estimation of the positions and depths for residual field anomaly. The maximum depth (with 15% depth estimation tolerance) to the top of source bodies 97m. The sources in south, east and west part are deeper than 70m while, sources in the central and north have depths sallower than 40m.

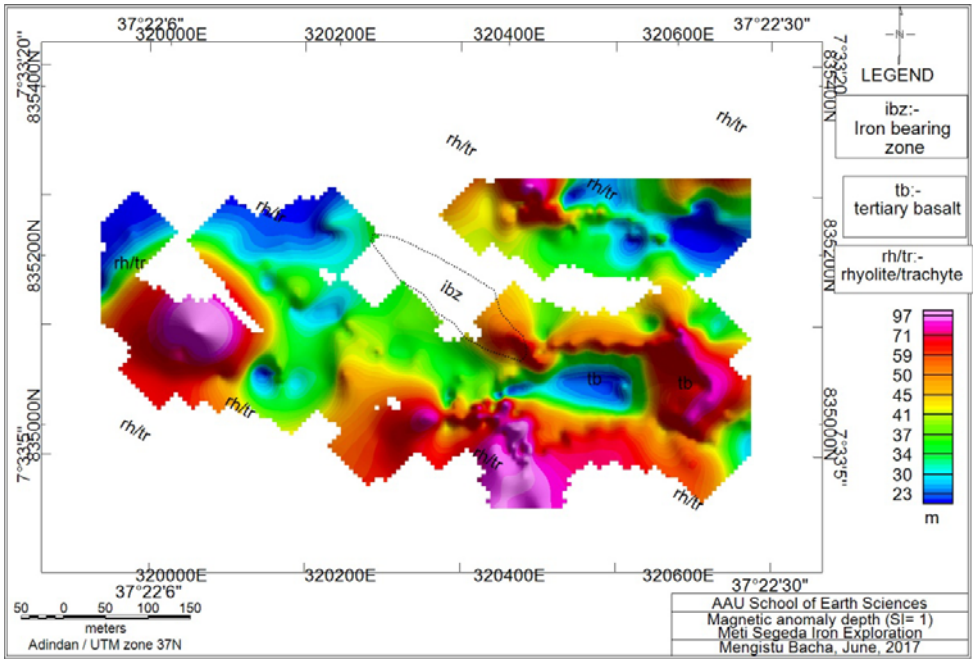

Figure 5.8: Estimated depth of the anomaly sources for SI =1

Generally, the geological model created infered from magnetic data helps to:

- Extract quantitative parameters (extension/depth) of the subsurface units
- Infer the possible subsurface rock unit along extracted profile
- understand the structural setting of the subsurface under extracted profile

5.2 Induced Polarization/Resistivity

5.2.1 Qualitative Interpretation

In qualitative interpretation, possible anomalous zones are identified. However, the chargeability and resistivity anomalies are apparent and the depth is pseudo. As IP/R methods can delineate the rocks, their results from a dipole-dipole array configuration survey are presented by, stacked apparent resistivity and chargeability pseudo section and plan maps as in figures 5.9 to 5.15

5.2.1.1 Stacked Apparent Chargeability Pseudo-Section maps

The average chargeability pseudo-depth sections for the 20m dipole length are displayed in figure 5.9. The average chargeability value varies from 0 to 20mV/V. The values below 4mV/V are taken as backgrounds and those between 4 to14 are treated as intermediate while, above 15mV/V are considered as strong anomalies. Lines 100N, 50N, 0 and 50S are characterized by NW to SE dipping higher chargeability zones which may be due to the cumulative effect of mixture of iron in association to quartz and chargeable minerals.

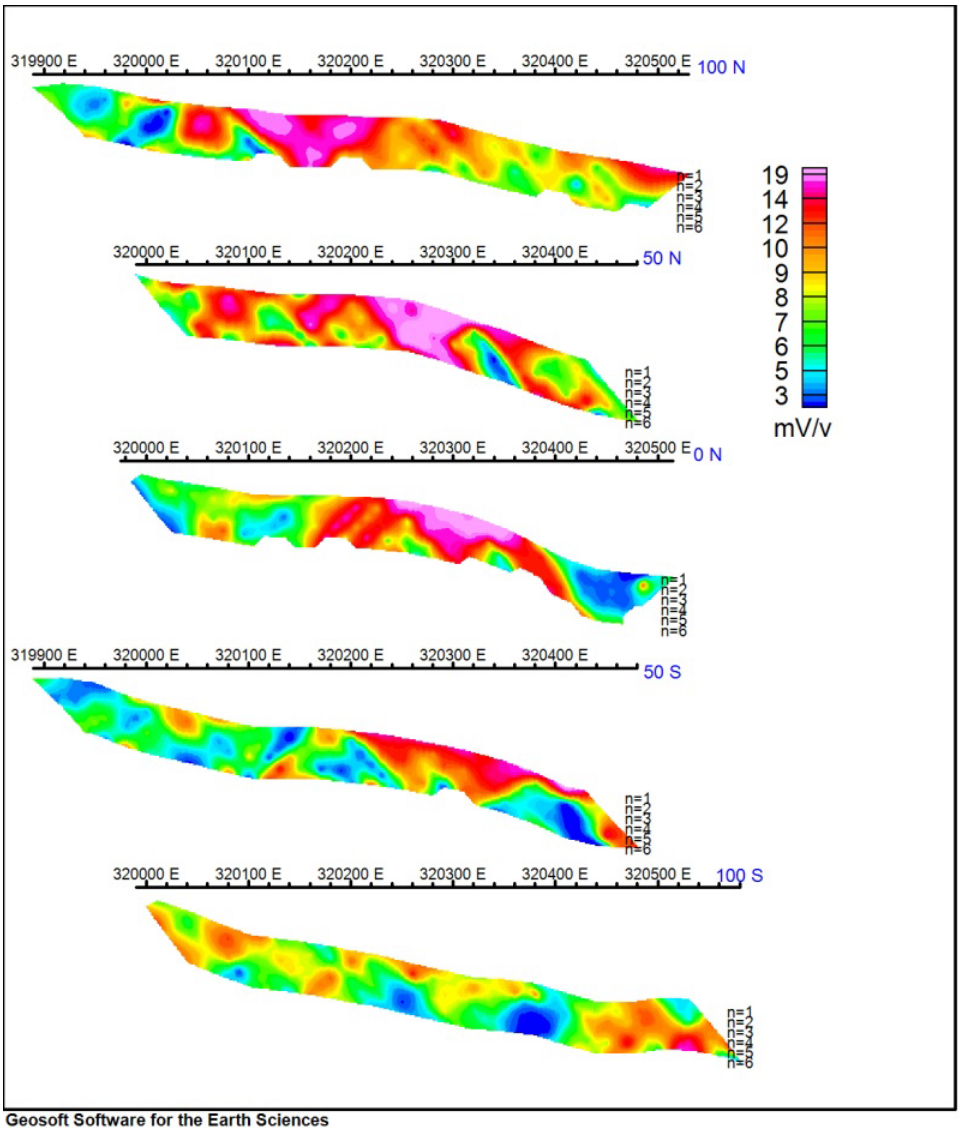

Figure 5.9: IP stacked pseudo section map

For line 100N, IP halo region started near 320300E, and anomaly values increased to ward west until the maximum pant leg anomaly greater than 17mV/V is reached between 320100E and 320200E. The center of maximum anomaly zone of line 50N is shifted toward the east by 140m relative to the center of anomaly starting point of line 100N. This anomaly shift is may be due to NE-SW extending structure that clearly observed on resistivity stacked map of figure 5.14. The anomaly value observed in line 50S is greater than 19mV/V and starting at some depth having dip direction from NW to SE. Similarly, the anomaly of line 0 show similar dip direction, shape and anomaly values except at its east end low IP zone is extending from surface to depth. The anomaly trend of line 50S coincides with that of line 0. The intensity of anomaly for line 50S is less than that of the previous lines. Its anomaly values increasing toward to east, however it came to surface. Low IP zone is observed at the depth of eastern end. The eastern part of the line is characterized by mixed low to moderate IP values. Line 100S is characterized by moderately high and low IP values and show no definite anomaly features.

Generally, stack chargeability map revealed three zones of high, moderate and low IP values which are agreeing by all lines. A NW to SE dipping of high IP anomalies zone are observed connecting line 50N, line 0 and line 50 S. This higher IP zone is shifted toward east by 140m relative to the anomaly of line 50N probably due to NE to SW trading structure crossing line 100N, 50N, 0 and S 50S. Another weak zone crossing line 100N and 50N in NW to SE direction is observed. Therefore the mineralization may be controlled by these structures. The background values (7 to 8mV/V) of IP anomalies are observed at the western side on all lines, while low anomalies of values less than 5mV/V appeared at the surface of eastern end of line0, which is then, shifted to depth on the next line 50S and 100S. Even though, the northern end of the grid was inaccessible, IP anomalies seems open toward north, while dies out toward the south.

5.2.1.2 Chargeability Plan Maps

Plan maps reflect the lateral variation of average chargeability and apparent resistivity over a horizontal plan at a certain depth. In this paper, IP/R data was acquired from six level (n =1to n = 6). Level 1, 3 and 5 are discussed and presented for chargeability as in figure 5.10 to 5.12.

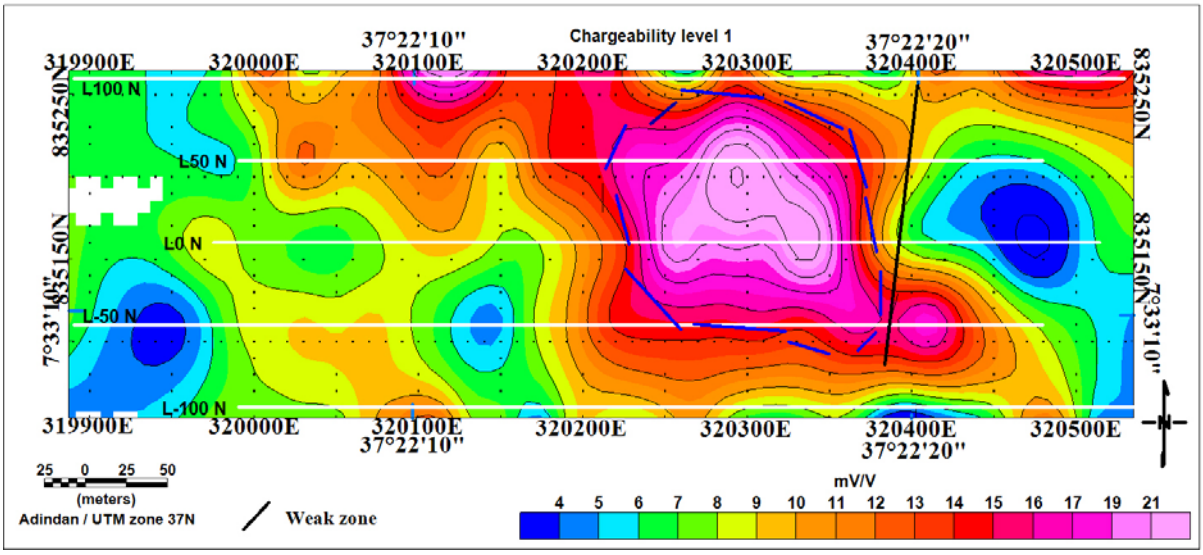

Figure 5.10 Chargeability plan map Level 1

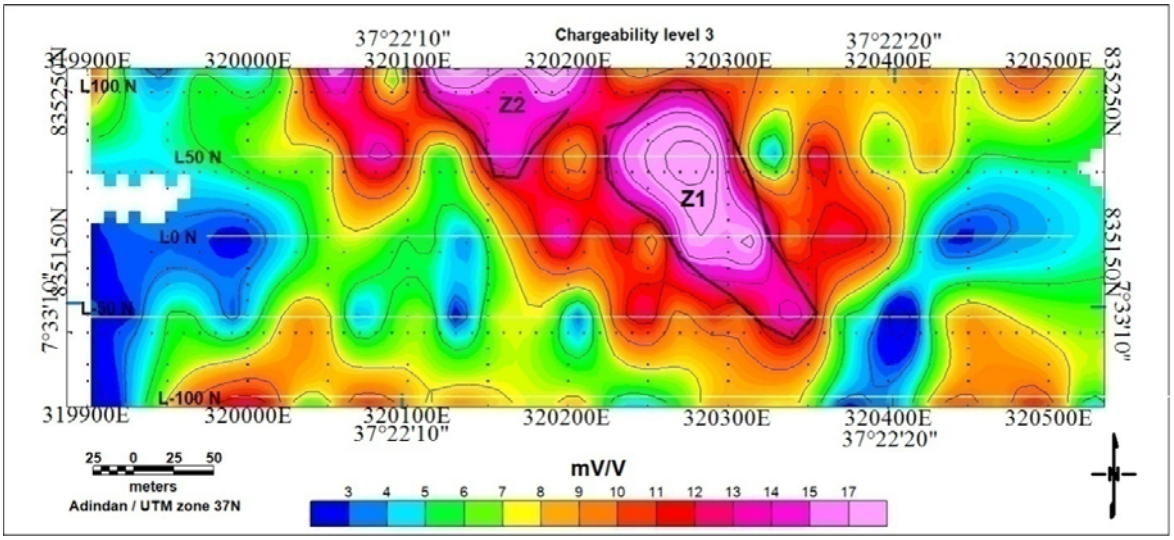

Figure 5.11: Chargeability plan map Level 3

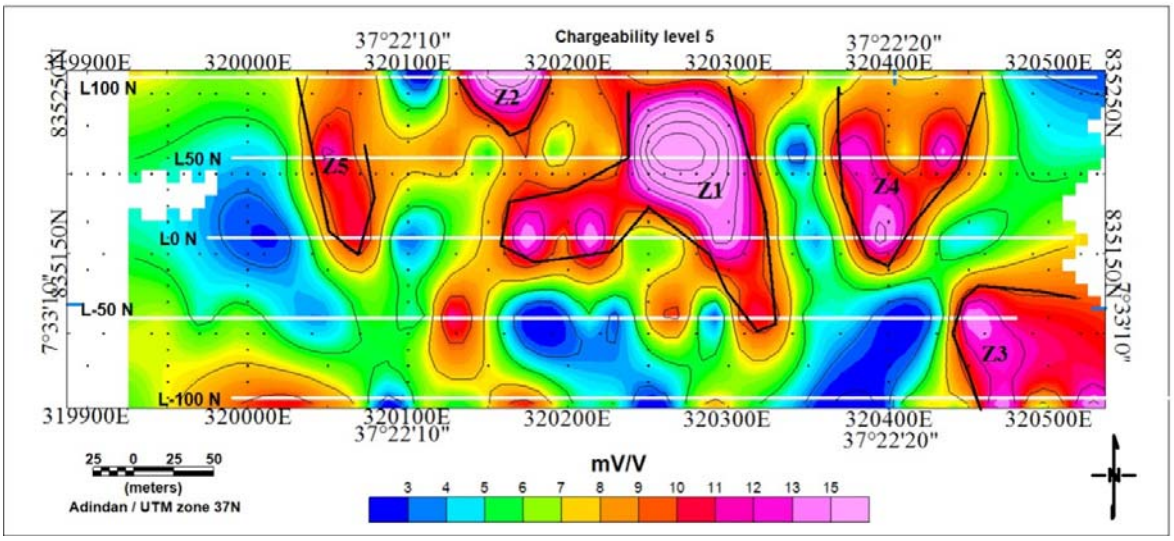

Figure 5.12: Chargeability plan map Level 5

The average chargeability map for the first level (n=1) is shown in Figure 5.10. A relatively high anomalous feature (up to 22mV/V) is mapped between stations 320150E and 320350E and this feature roughly dips easterly at medium angle. This anomalous zone is associated with the occurrence of some chargeable minerals that are associated with hematite. This geophysical interpretation is supported by thin section analysis result. It is worth to note that the strongest anomalies, with values greater than14mV/V, are detected from 320250E to 320350E across Lines 0 and 50N, which means it has an approximate width of 100m. On the other hand, the eastern and western parts of the grid are mapped by low-moderate-chargeability responses (often below 9 mV/, rarely up to13 mV/V) that represent an area of less quartz concentration. Figure 5.11 shows the chargeability anomaly for the third level (n=3), which has a similar trend to that of level 1 discussed above. Here the exception is that the larger anomaly is split in to two separated IP anomalous features denoted as Z1 and Z2. Anomalous zone still starts from central north, follow NW to SE trend with an IP values of 10 to 20 mV/V crossing lines 100N, 50N, 0, and 50S. Zone 1 (Z1) is the highest of the two zones which characterized by values greater than16mV/V at NW to SE direction crossing line 0 and 50N near at 320300E. Moderate IP zone of 8mV/V is observed at the south east corner. Just as, in similar way as that of level 1, these IP anomalous zones may be due to the association of highly disseminated magnetite with hematite.

As the hematite could occur as the result of weathering of magnetite on the surface, this high chargeability could be due to this result and dissemination of magnetite. In other way, at depth there could be sulfides minerals that should be investigate further. In figure 5.12 of level 5 even though, the general trend of anomaly follow the same pattern as that of the previous one, main anomaly seems to pinch out into small anomalies. A new moderately high anomaly starting to observed at southeast side of level 5. Generally, chargeability plan maps of level 1, 3 and 5 revealed easterly dipping main anomalies that started to appear at 320300E and its intensities decreasing from level 1 to level 5. The wider anomaly that is observed at surface shrinks as it goes to depth and the anomalous split into different small anomalies at depth.

For correlation of IP anomalies of different depth, stacked IP plane maps are used for different level (n=1 to n=6) as in figure 5.13. The map reveled that, IP anomalies start at the center of the area, and follow NW-SE trend especially for n =1 to n = 4. The geometry of anomalies are varying from shallow to deeper depth following nearly the same trend for the first four levels and split in to separated anomalous zone for the last two levels. For deepest depth, anomalies seem to follow E-W trend at the northern and central parts. The anomalies between levels 1 to level 3 are stronger and show clear dimension. These anomalies zones may be due to chargeable minerals that are associated with hematite.

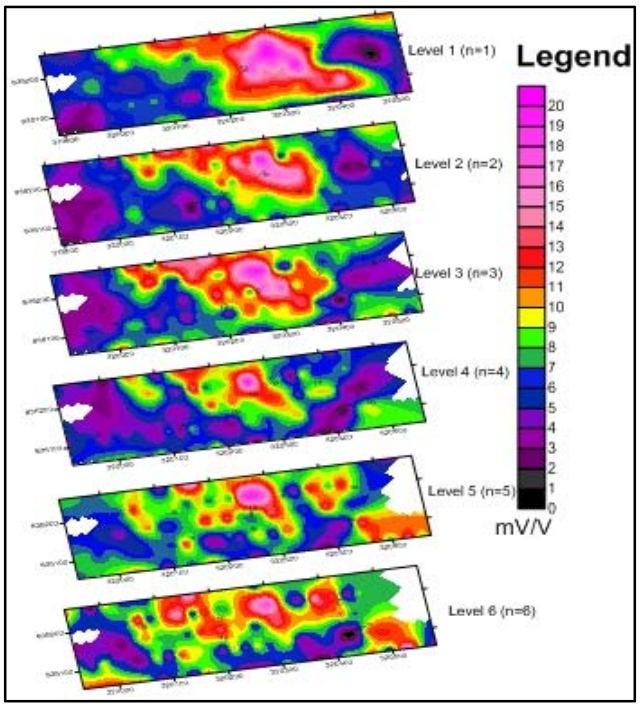

Figure 5.13 Stacked IP plan map

5.2.1.3 Stacked Apparent Resistivity Pseudo-Section Maps

From apparent resistivity stacked map of figure 5.14, line 100N seems to b affected by three weak zones at the western and central part. Two of them laid from NE to SW direction, while the rest one has the NW to SE direction and blocked by the previous. Four zones of higher resistivity are observed between those weak zones which may have effect on mineralization. The resistivity of line100N reaches 700Ω.m. At west and central part of this line, high resistivity unit extends from surface to maximum depth. Line 50N shows similar resistivity anomaly trends and structures with line 100N having maximum resistivity of 600 Ω.m. However, most parts of line 0 are characterized by intermediate to low resistivity anomaly, a NE to SW directed anomaly is extended from line 50N to line 0.

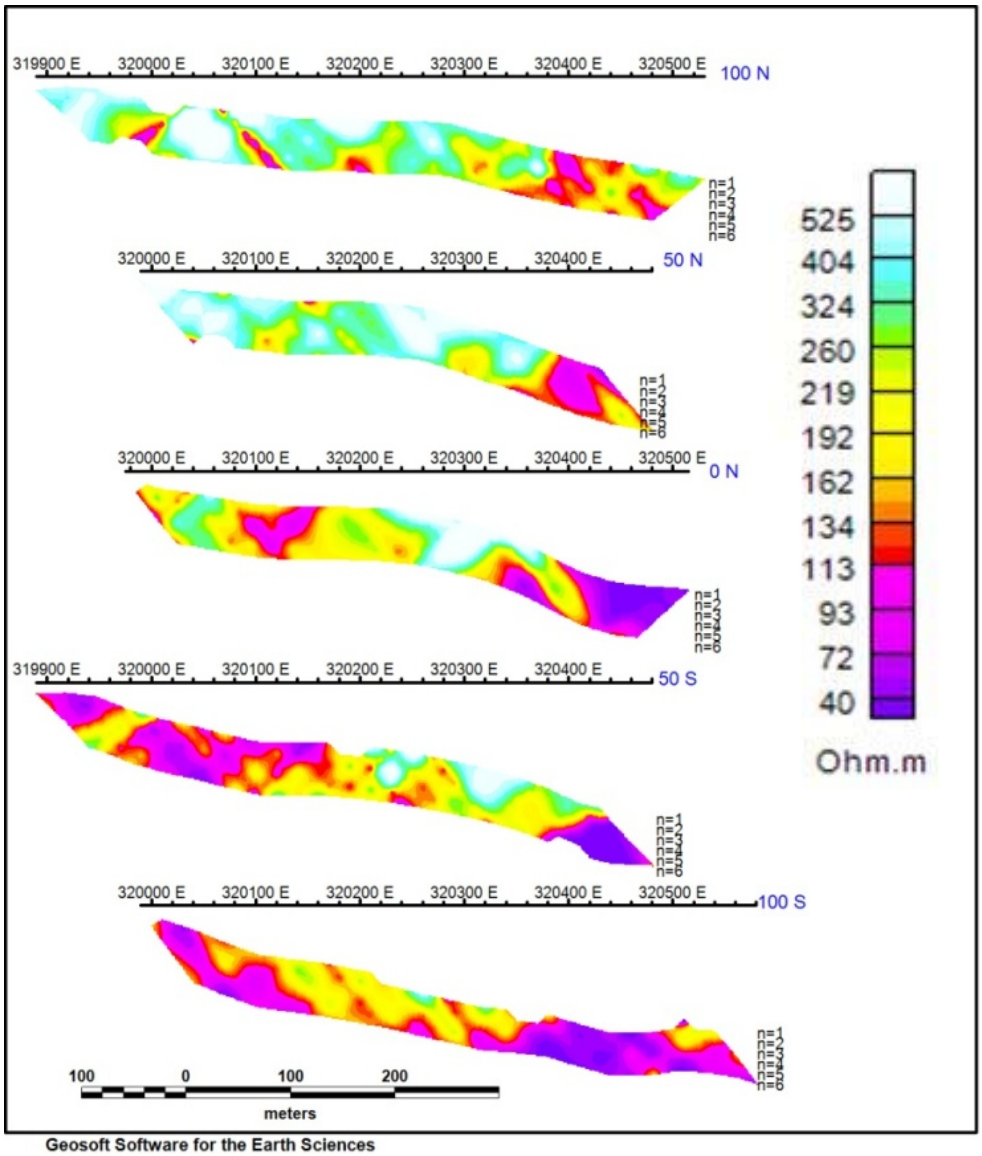

Figure 5.14: Resistivity stacked pseudo section map

5.2.1.4 Resistivity Plan Maps

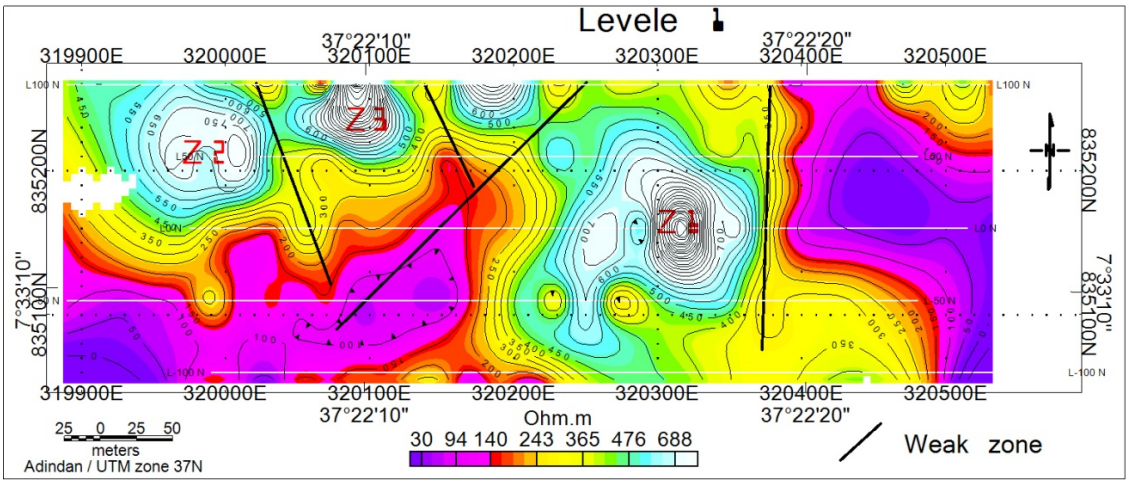

Figure 5.15 Resistivity plan map level 1 (n=1)

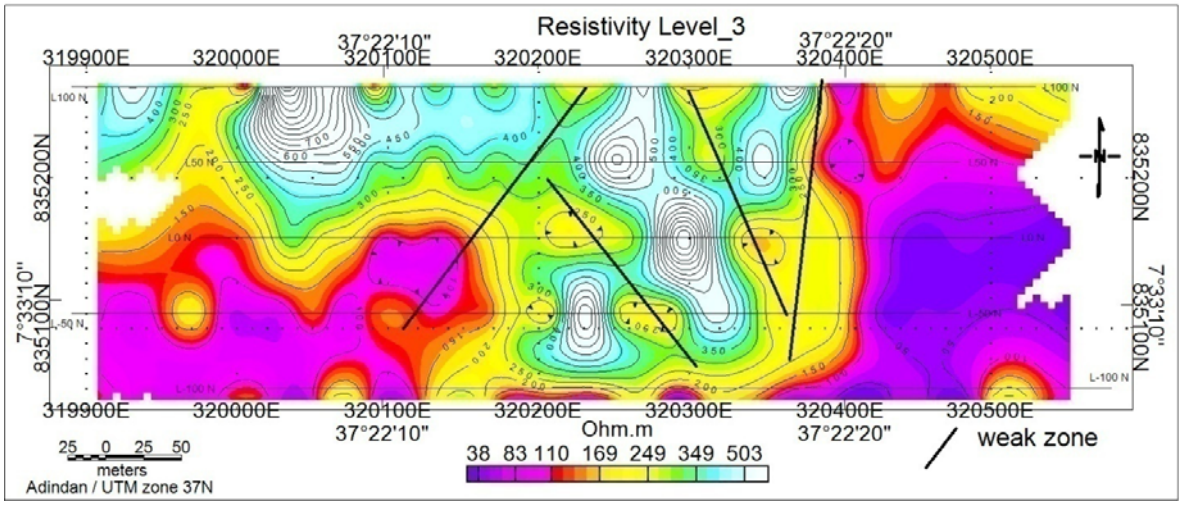

Figure 5.16 Resistivity plan map level 3 (n=3)

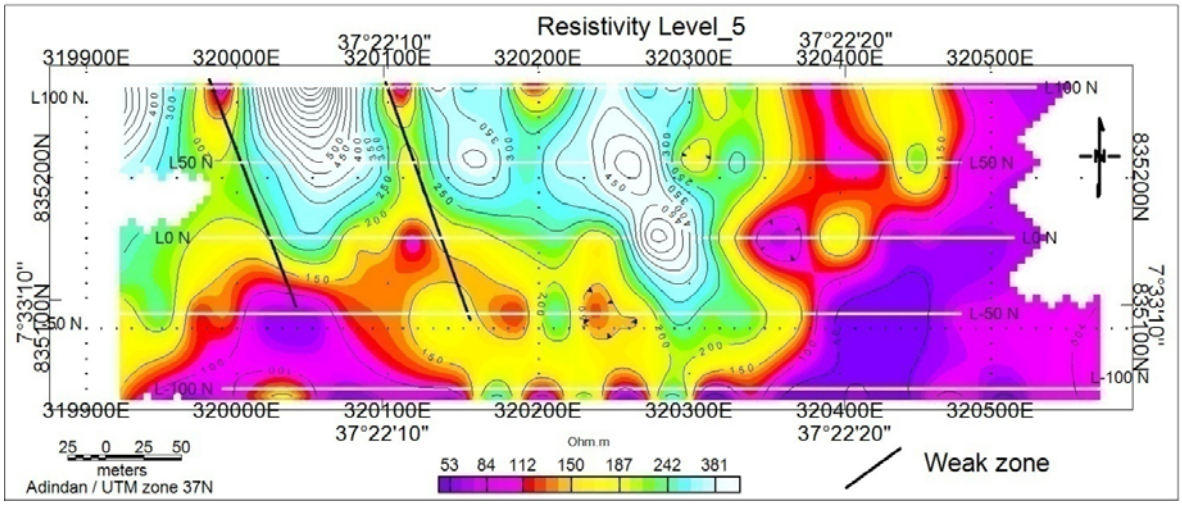

Figure 5.17 Resistivity plan map level 5 (n= 5)

In level 1 apparent resistivity plane map (Figure 5.15), three anomalous zones are observed. They cover the central and northern part of the study area having maximum value of 700 Ω.m. The central highest resistivity zone Z1, crosses line 50N, 0 and 50S, and line 50N is again crossed by other anomalous zone (Z2) at NW side. Two lower (< 150 Ω.m) resistivity zones, are observed at eastern and SW parts. The central resistive unit is due to the resistive nature of quartz mineral in association with iron that was analyzed from thin section and silicate analysis. In addition, the same resistive zone may also be attributed to discontinuous iron ore that slightly lost its high conductivity due to its distributions. One NE to SW directed and two NS directed weak zones are observed at this depth. As resistive regions are observed between weak zones that supported by other approaches, mineralization is affected by strictures.

Level 3 resistivity plan map (figure 5.16), shows three resistive zones of higher values (>350 **Ω**.m), intermitted (>170 **Ω**.m) and low (< 110 **Ω**.m) which have the same shape as that of level 1. Resistive zones are dominated at the northern and central part of study area. NE-SW weak zone that was observed in above shallower depth between 320200E and 320300E is also extended down to this depth. The NW-SE weak zone that was observed at level 1 between 320100E and 320300E starting from northern side seems blocked by that of NE-SW and came to appear again near 835190N with its same previous direction. The highest resistivity zones are cross all except line 100S which is characterized by intermediate and low apparent values at central and both end parts respectively. NW to SE and NE to SW weak zones are observed especially at the central resistive zone.

The general trend of anomaly and subsurface units are stable and similar to that of shallower above levels. Structures around resistive zones for this depth show that, the controlling factors of structures are also extended to this depth. At deeper level of figure 5.17, the anomalous zone seems to split into four parts and shows the fault signature (at 320100E) that was not clearly observed in level 1. The Eastern and SW parts of the area are covered by low to intermediate resistive units. From these three level maps, the eastern and southwestern parts of the area are characterized by low resistive volcanic rocks, while the northern and central parts are dominated by moderate to high resistivity anomalies.

For simple correlation between resistivity anomalies of different depth levels, resistivity stacked maps of figure 5.18 is produced. Almost in all depths the resistive body is shown to dip NW to SE. Resistive bodies occupy the northern and central parts of the area. For level 2 to 5, the whole geological setting from shallow to deeper seems stable and similar. At deeper depth, both the geometry and intensity of resistivity anomaly changed in relative to upper levels.

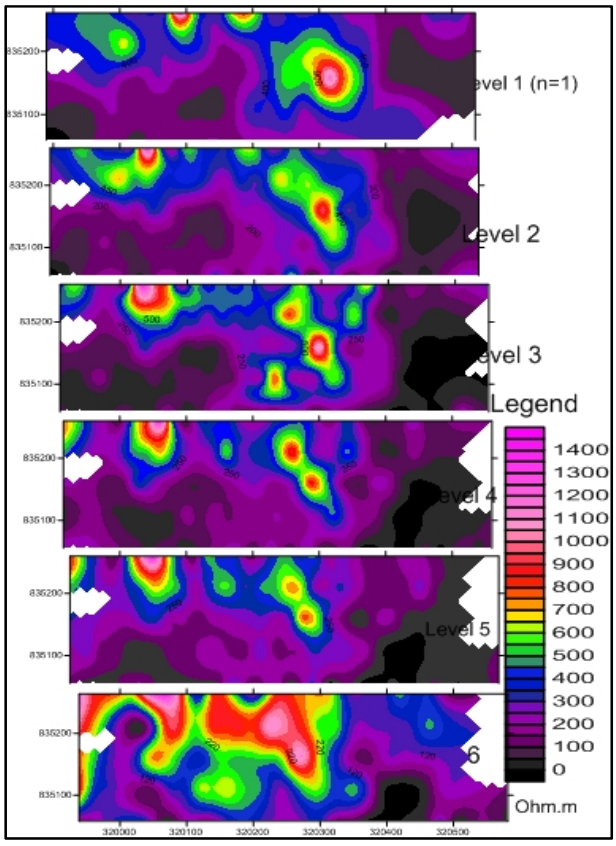

Figure 5.18 Stacked resistivity plan map

5.2.2 Quantitative interpretation

The RES2DINV software was used to interpret IP/Resistivity data quantitatively to produce 2D Inverse Model for Resistivity and chargeability sections. The iteration RMS errors were observed to be less than 10%.The inverted models of resistivity and chargeability for lines 100N, 50N, 0 and 50S revealed the extension and dip of mineralization. Minimum contour values of 8mV/V and 50Ω.m were used for IP and resistivity inversion respectively.

5.2.2.1 IP/Resistivity Inverse Model Section (Line100N)

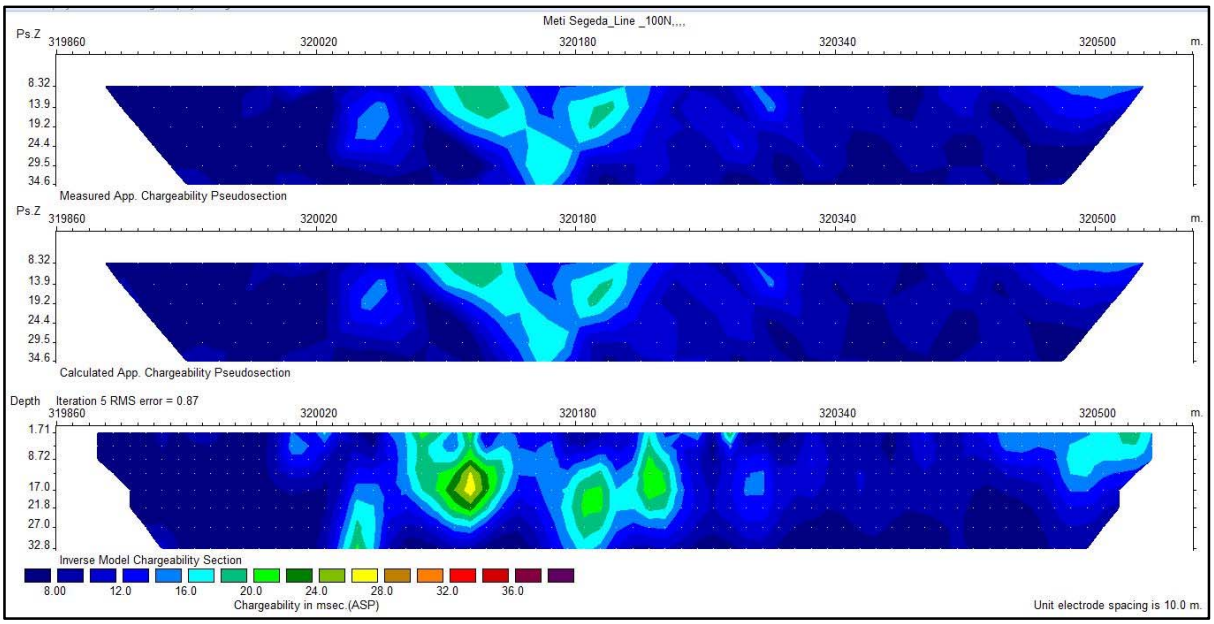

Figure 5.19: I P Measured and inverted section for line100N

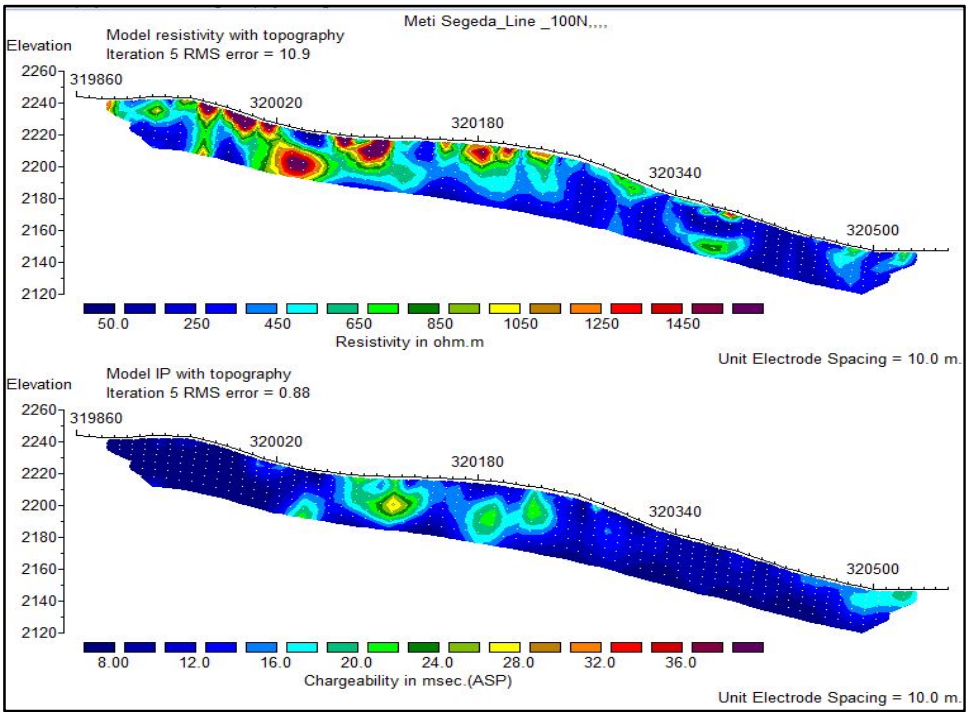

Figure 5.20: Model resistivity and model IP for line 100N

From model resistivity section (figure 5.20) of line 100N, two weak zones are observed between 320020E and 320180E between three resistive zones. The featureless of inverted model resistivity makes difficult to correlate resistivity anomalies with their possible geological sources. This higher resistivity zone dips NW to SE starting from surface to 33m down. The low resistive zones coincide with low chargeability. Two high chargeability zone values greater than16 mV/V are observed around 320180E. This zone correlates to the fault and higher resistivity zone of the same line which interpreted to be due to quartz and iron bearing zones. At the eastern end at 320500E a horizontal chargeable zone is observed near surface.

5.2.2.2 IP/Resistivity Inverse Model Section (Line 50N)

High resistive unit is started from surface and opened to ward depth of more than 32m in the western side, while in the central part, high resistive unit continuing up to 30m starting from surface.

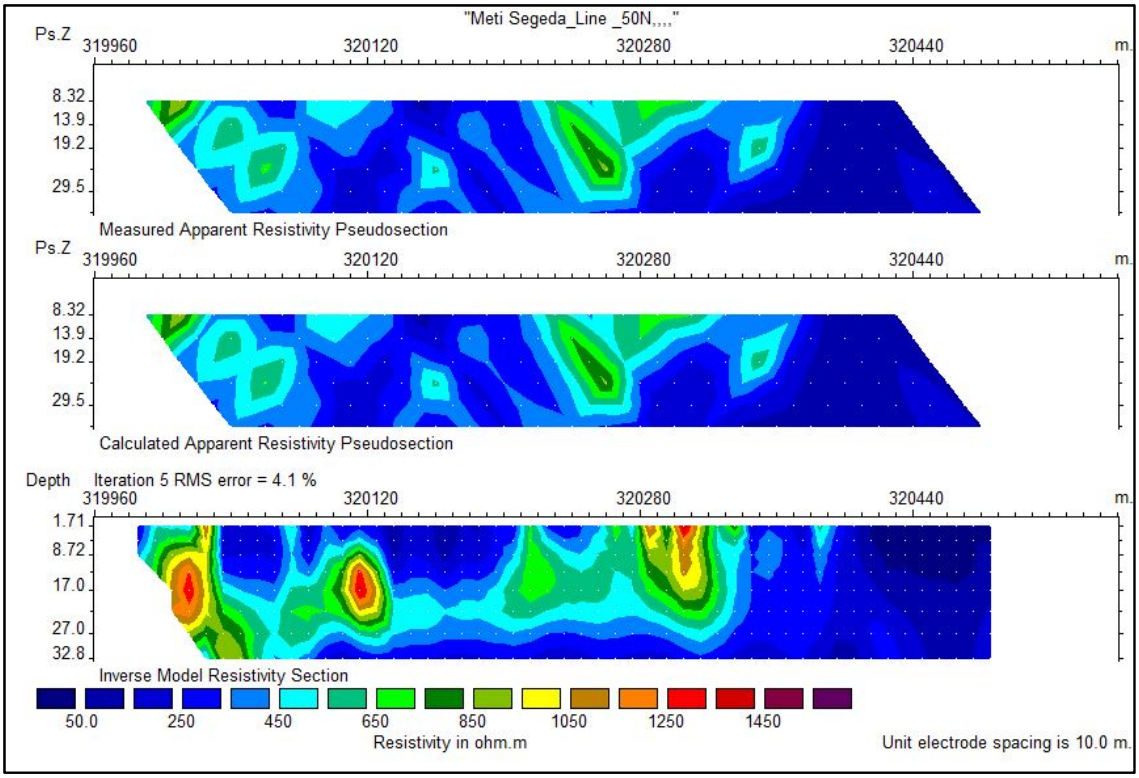

Figure 5.21: Measured and inverted Resistivity section for line 50N

For figure 5.22 chargeable zone of (14 to greater than 28mV/V) is observed between 320180E and 320370E. It dips SE with 10 to 30m depth starting from surface and cover a horizontal distance of 190m. Both eastern low and central strong IP anomalies directly correlate to equivalent intensities of resistivity anomalous of the same line. Therefore, this chargeable zone correlates to high resistivity zones that may be due to compacted volcanic rock.

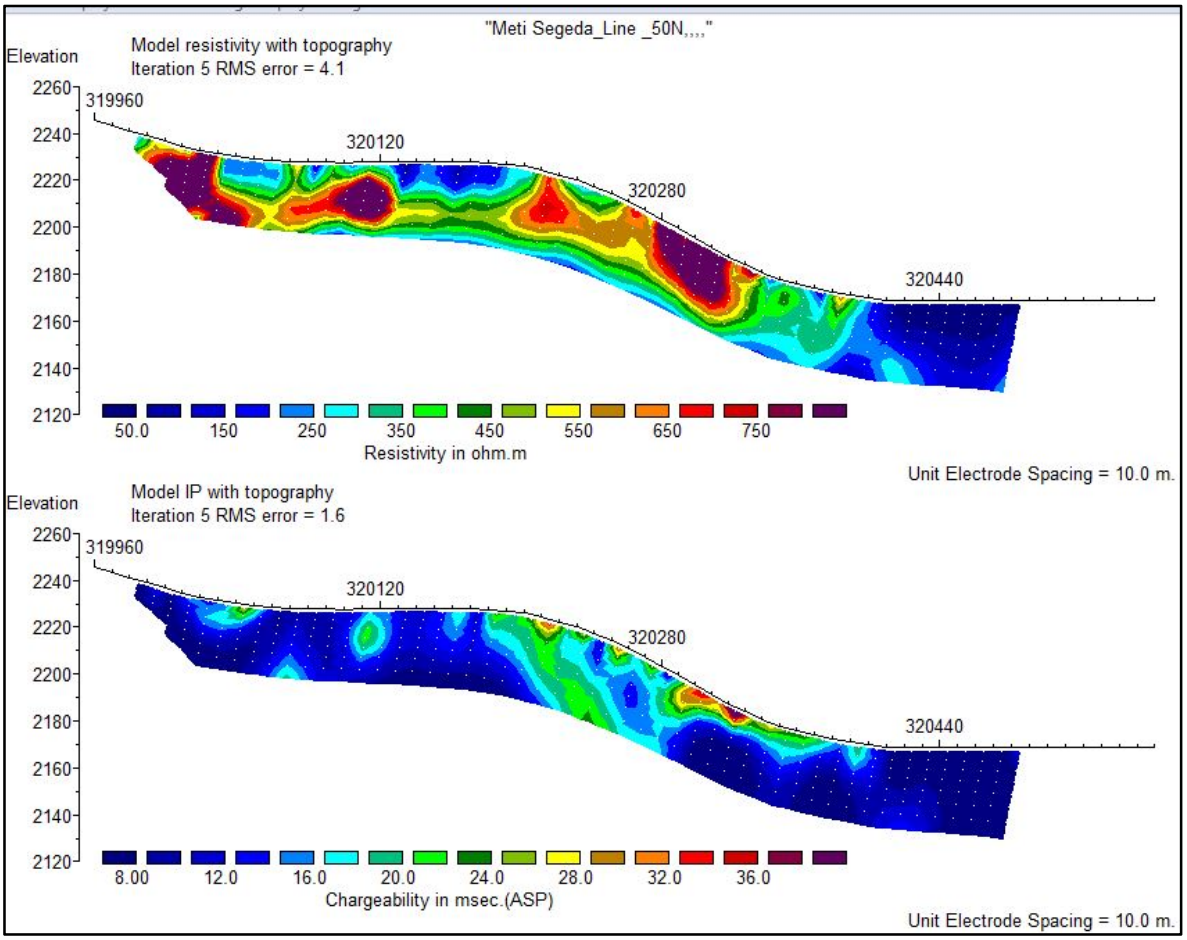

Figure 5.22: Model resistivity and model IP for line 50N

5.2.2.3 IP/Resistivity Inverse Model Section (Line 0)

From inverted resistivity section of line 0 (Figure 5.23), three units are identified as the eastern low resistivity zone, the central higher and the western and bottom central intermediate zones. The central resistive zone ranges from 450-51450Ω.m.

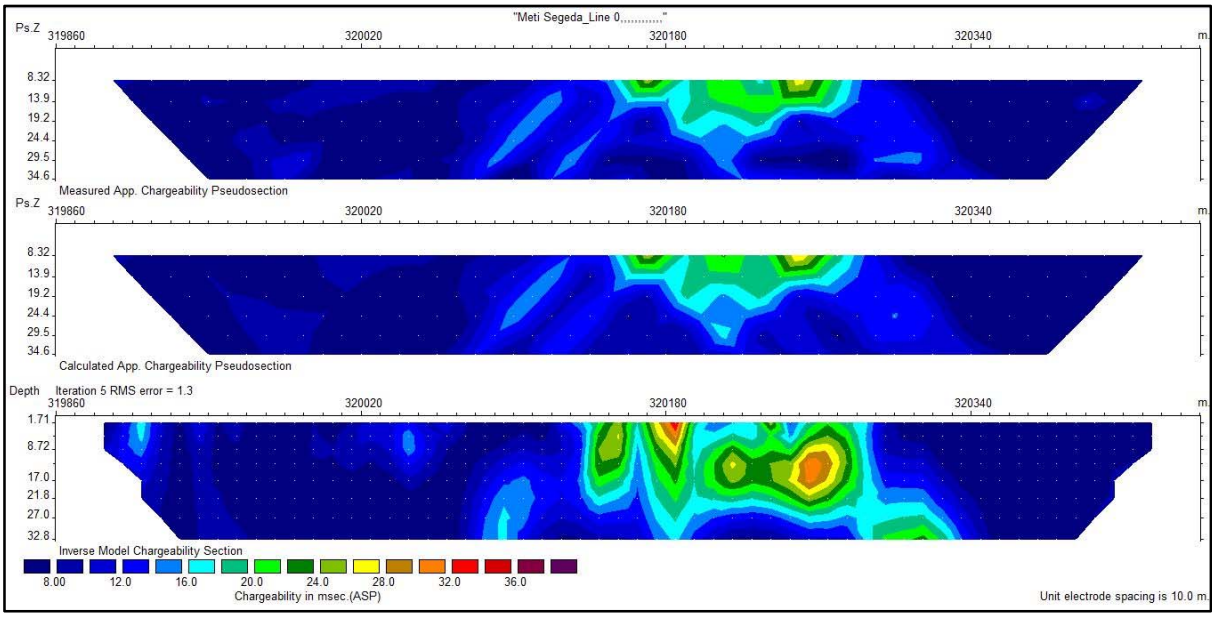

Figure 5.23: Chargeability measured and inverted section for line 0

From line 0 resistivity and IP model (figure 5.24), a resistive layer is observed along the surface and extends to depth at eastern part. As two resistive zones are connected by thin resistive surface layer, so that two chargeable zones are observed at corresponding location for the same line. The horizontal extent of this mineralized zone is 130m, with a depth of 21 to 32m. Generally, the low and high IP zones directly coincide with low and high resistivity for the same locations.

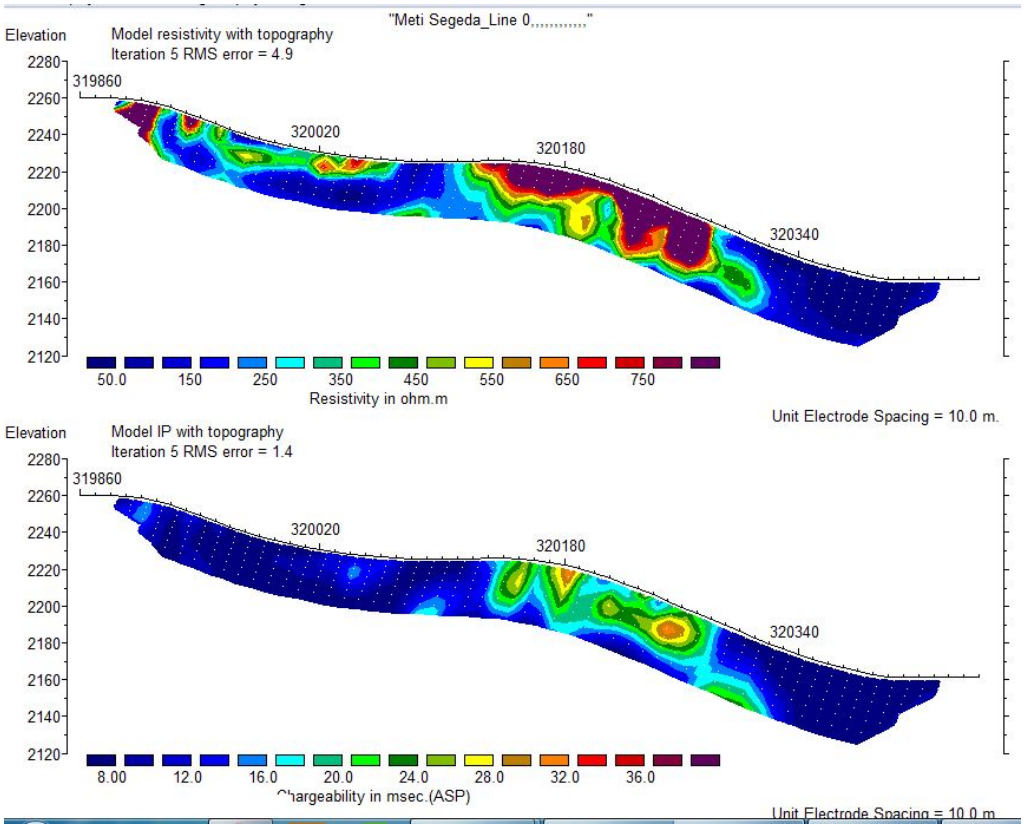

Figure 5.24: Model resistivity and model IP section for line 0N

The cause of resistive and chargeable zones in the survey area may be due to the discontinuity of iron (which in nature has high conductivity or low resistivity) throughout the mineralized zone and the resistive natures of quartz that mixed with iron with iron and other chargeable mineral in association.

5.2.2.4 IP/Resistivity Inverse Model Section (Line 50S)

Figure 5.25, revealed that, the chargeable zone is shifted toward east relative to the anomalies in line 0. Just as that of the previous discussion chargeable zone in this line also coincides with the resistive rock units.

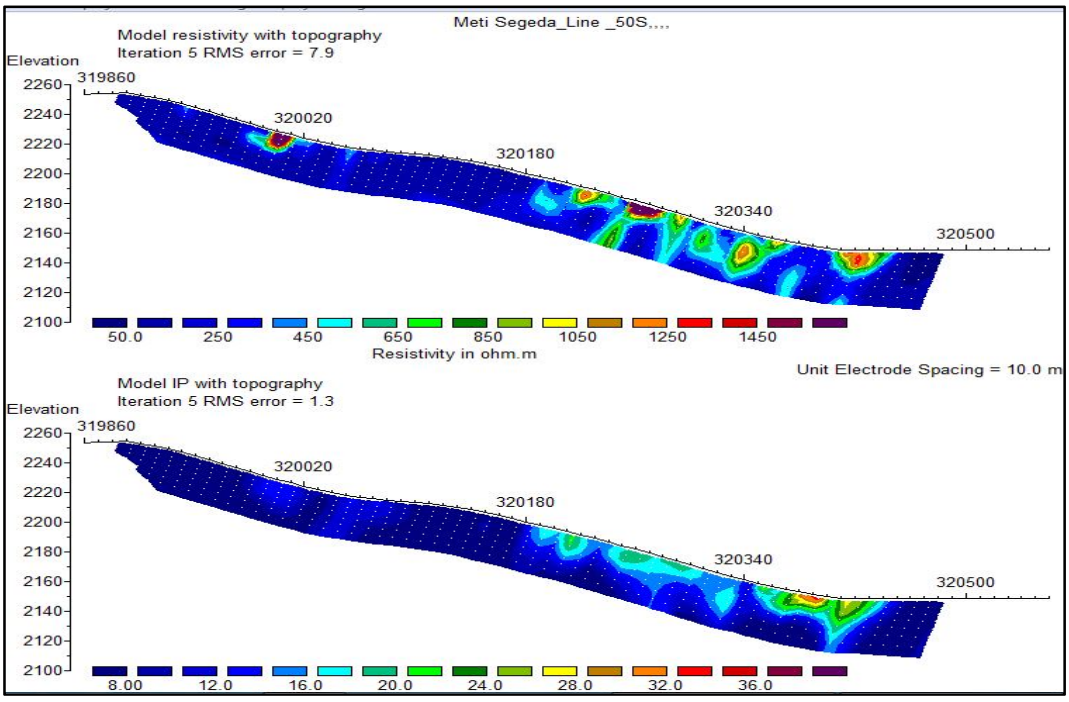

Figure 5.25: Model resistivity and model IP sections for line 50S

5.3 Radiometric Method

From the radiometric data, the overall distributions of each channel count in the area are discussed and their causes are inferred. The total counts, able delineate major lithological contact in the survey grid. Accordingly, it classifies the survey area into tree zones. The higher Tc counts (>70 cps) at the central part following NE to SW, the intermediate zones of counts of (>54cps) that cover most parts of the area and lower counts of (<40cps) at the SE corner. The highest peak total count zones are shown in three zones Z1, Z2 and Z3 (figure 5.26); the values of these three zones are exactly similar which can thus, interpreted as zone of similar lithological units. However, the NE to SW extending body is one lithologic unit, the break in between (zone of NW to SE) near Z1 and Z2 revealed that unexposed nature (thick over burden) of same extending unit.

At the SE coroner, low anomaly of Tc is clearly reveled basalt rock unit which also confirmed in thin section and susceptibility measurements. The rest parts of the area are covered by intermediate Tc values; which may be due to the variation in degree of weathering and attenuation of gamma rays from thick overburden and the effects of rhyolite and trachyte flows. The extension of basalt is more than the field observation as delineated by total count.

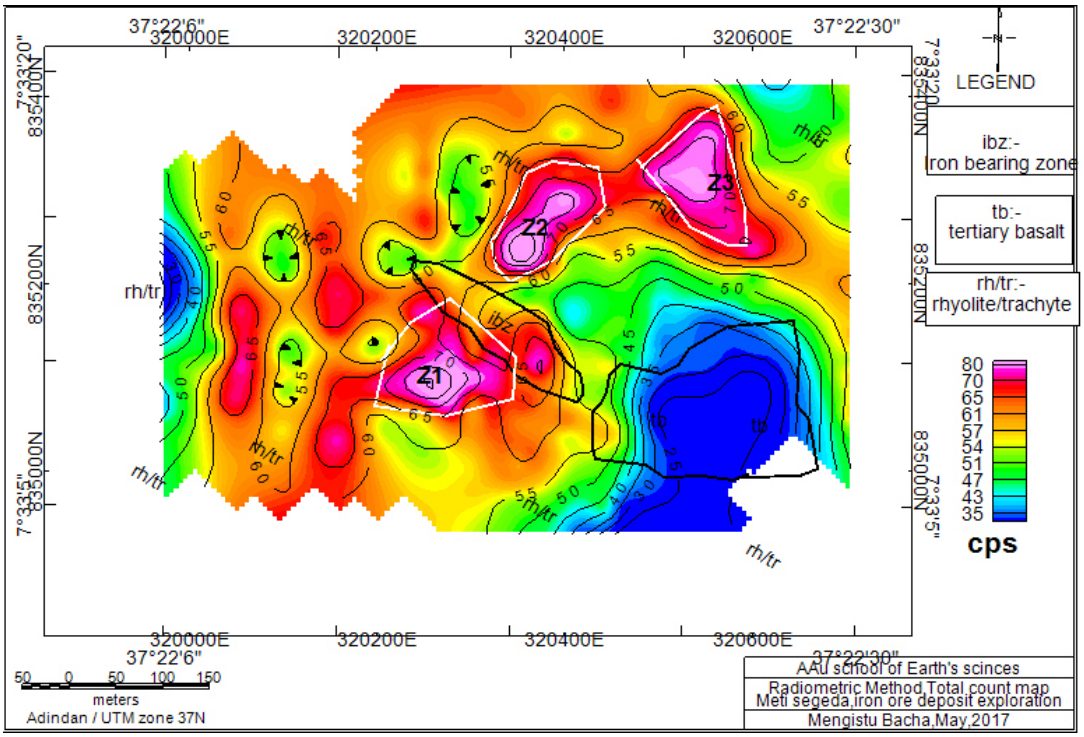

Figure 5.26 Total counts map

From figure 5.26 and 5.27 the total count (Tc) and potassium (K) count have shown generalized similar characteristics. Both of them are correlated in indicating exposed out crops at the NE and SW part of the area by higher concentration. The NW to SE intermediate total count rate mapped by total count (Tc) is further delineated by low potassium counts. The low potassium reading zone is parallel with the strike of mineralized zone. Based on lineaments those observed in analytic signal (Figure 5.3), residual (Figure 5.4) and tilt angle (Figure 5.5) anomaly maps, low potassium zone may have association with fracture that contributes for mineralization.

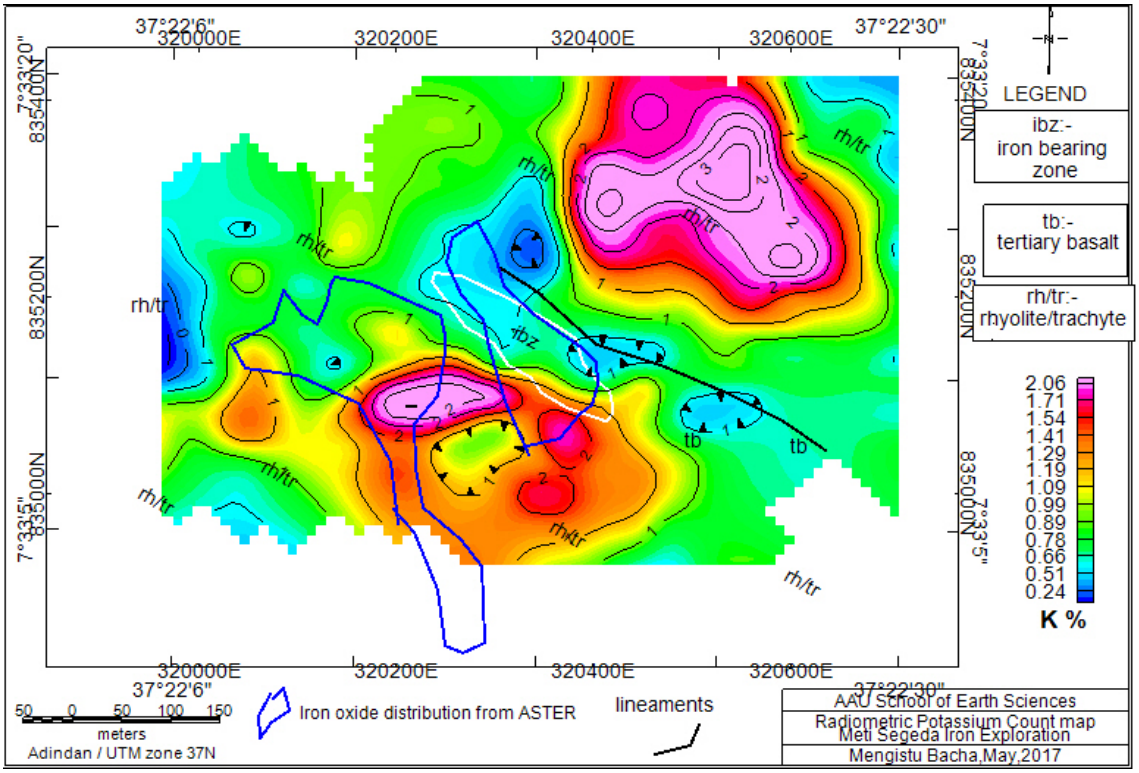

Figure 5.27: Potassium concentration map

Though the uranium concentration map of figure 5.28 keeps the general trend that is observed on the total count, at some places it shows different signatures to that of Tc or K concentration. Uranium concentration delineates the survey area to three zones of different concentration of equivalent uranium concentration. The higher uranium values aligned along NE to SW through the central part of the area. Enhanced uranium values may occured around the probable fault structure, as a result higher uranium anomaly at the center interpreted as fault zone which coincides with the lineaments and thus, associated with mineralized zone. The low uranium concentration in the south east corner of the area is attributed to the basalt which is delineated by other methods.

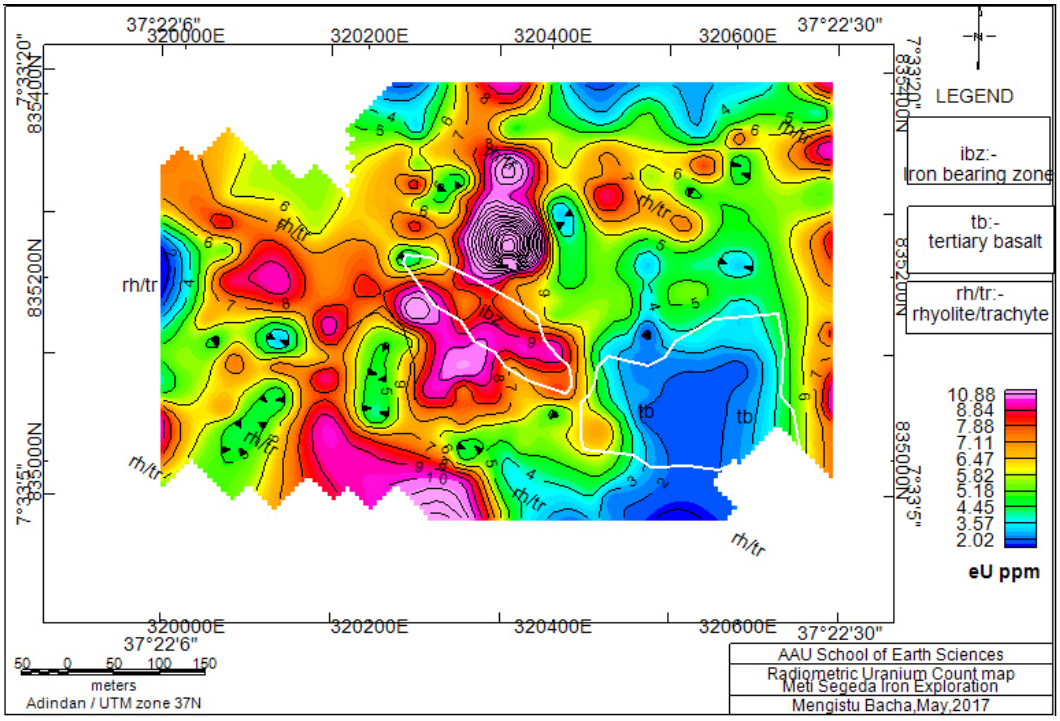

Figure 5.28: Uranium concentration map

The thorium to potassium ratio maps of figure 5.29 shows that, NW to SE higher anomaly at the central part and low ratio count at the south and north east part of the area. As potassium concentration is less along the strike of mineralized zone, the ratio of "Th" to "K" will be high if the value of Thorium is high and thus, the ratio of "Th" to K" is high along the strike of mineralized zone indicating mineralization.

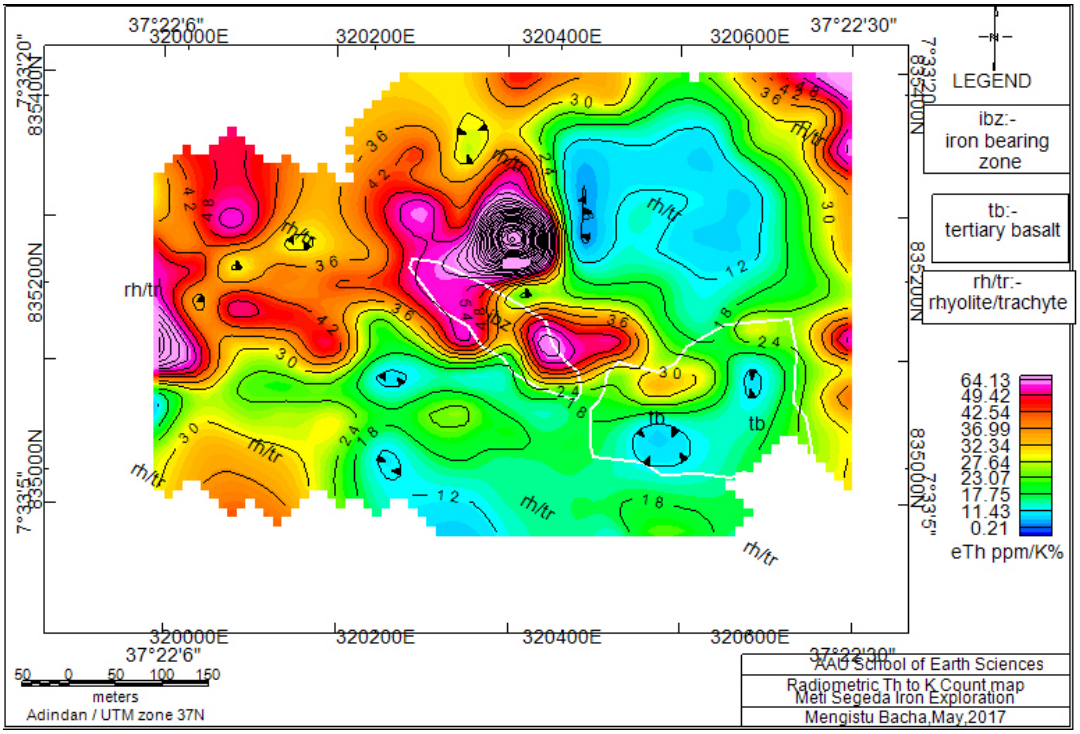

Figure 5.29: Thorium to potassium ratio count map

Weathering and metamorphism can modify the radioelement content of rocks profoundly. Uranium is easily oxidized to a water-soluble form; and can be readily leached and redeposit in sediments at large distances from the source rock. Thorium has no soluble ion and therefore tends to remain with the parent rock or is transported over relatively short distances in the form of solid mineral grains. Weathering, therefore, produces significant effects upon the distribution of radioelement: It decreases the eU/eTh ratio in weathered rock. Figure 5.30 shows the higher Uranium to Thorium ratio nearly at the center and decreasing outward showing that, the decreasing of the ratio leads to dispersion halos and increasing of weathering.

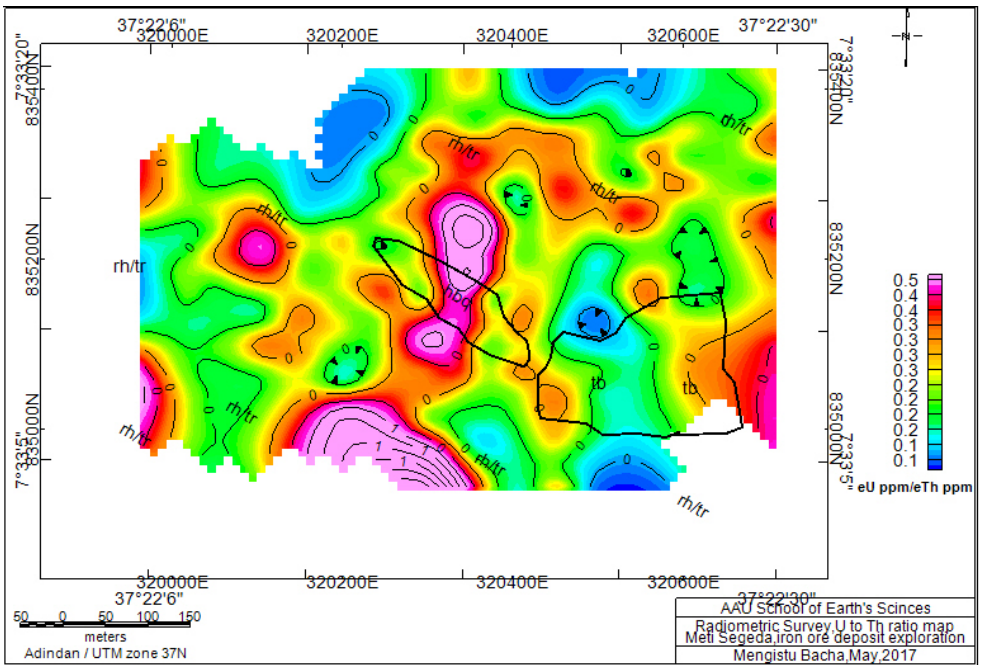

Figure 5.30 Uranium to Thorium ratio map

The ternary map of gamma ray spectrometric survey revealed that, the central parts of survey area around lineaments (cyan color) are characterized by uranium and Thorium radioelement concentration. As, Uranium concentration may show significant signature over faults while, Thorium over the mineralization, the central and north extending zone may be associated with iron mineralization which is affected by structure. North eastern part of the area is characterized by high potassium.

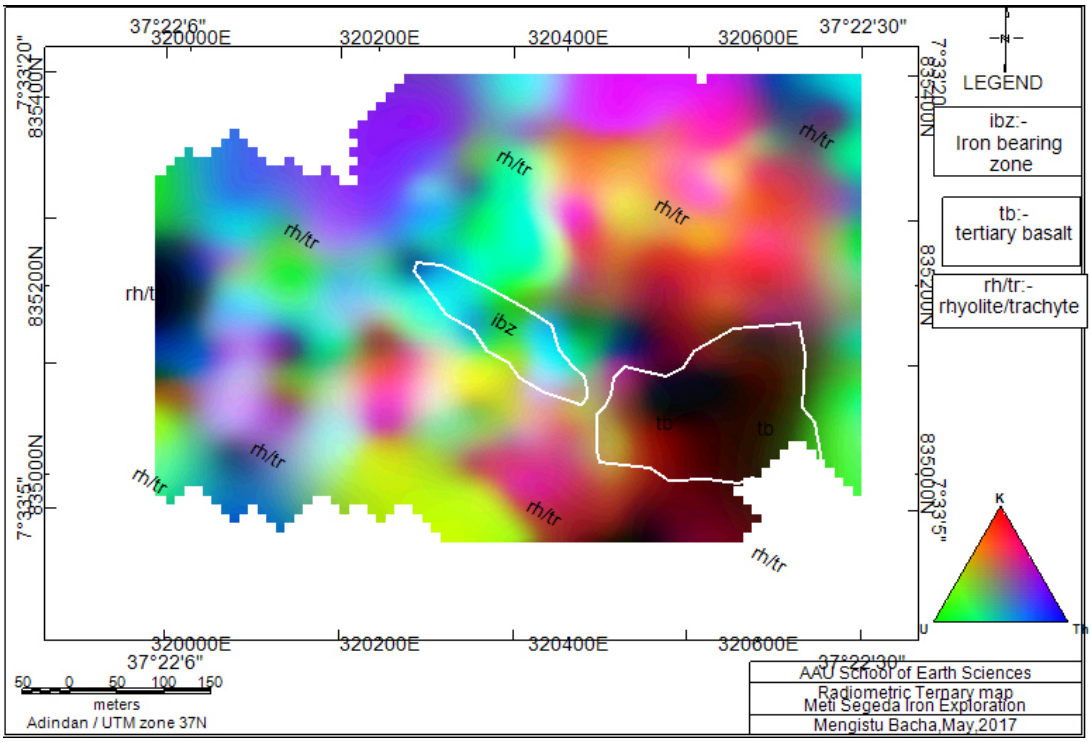

Figure 5.31 Ternary map of radioelement concentration

Generally, the decrease in Tc, U and K responses at some places in the area is mainly due to the increasing of the over burden soil thickness which, attenuates the energy of Gama rays from the sources under these layers. In other way, with the intensity of Tc the area is classified in to three different zones.

- Low values of < 50cps at the south east coroner is attributed to olivine basalts
- Intermediate radioactive zone, of values 47- 60 cps at the western, central and northern part of the area are attributed to iron bearing and quartz rich rhyolite flows.
- High radioactive zone, greater than 61cps central south and central north as defined by Z1, Z2 and Z3 are due to exposed rhyolite and trchyite flows.

5.4 ASTER Satellite Imagery Interpretation

In this study, tried was made to detect the iron alteration distribution in Metie Segeda and its vicinity using ASTER satellite imagery data analysis. Band ratio was used for iron oxides detection with the help of Qgis software. The ratio of Band2 to Band1 used to enhance the small contribution of iron oxide minerals and discriminate zones of iron oxide in study area with its surrounding as shown in figure 5.38.

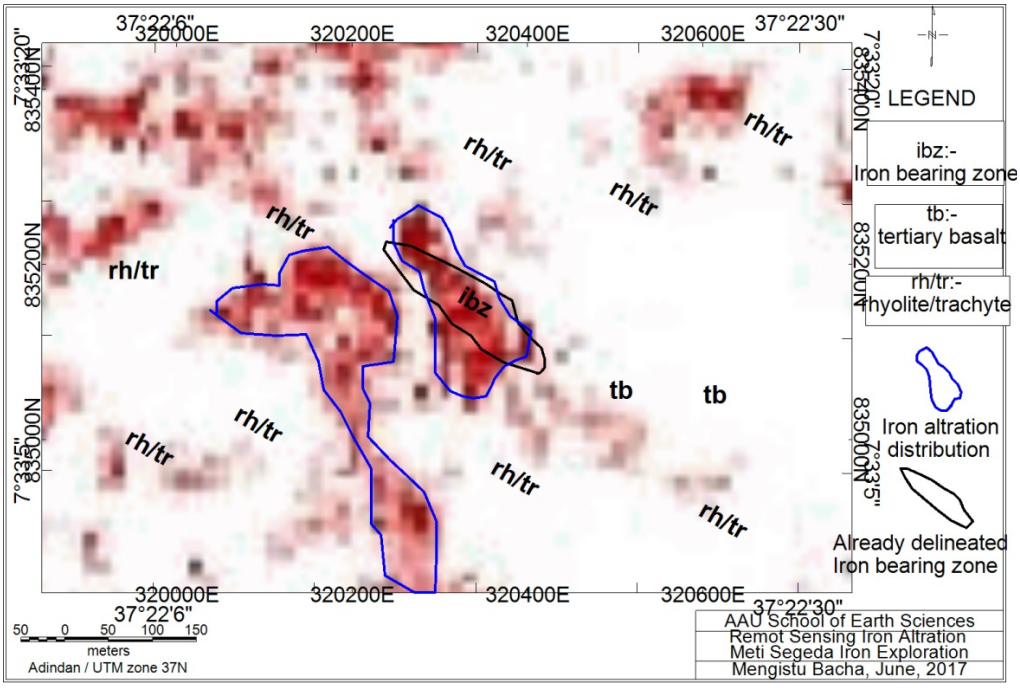

Figure 5.38: Iron oxide distribution from ASTER band ratio (B2/B1)

From map 5.38, the iron distribution is coinciding with the iron bearing zone that already delineated. However; additional iron alteration zones are mapped in NW part. The distribution is seems strong to far northwest which recommending the extensional survey in far NW direction.

CHAPTER VI

6. Integrated Interpretation

The result of individual geophysical methods has been discussed and interpreted separately in chapter five. Here the results of those different methods are integrated and their general effects are discussed and interpreted. From separately interpreted result of each geophysical method, strong resistivity, high Th to K ratio, intermediate magnetic (analytic signals) and high IP anomalies were compiled together. The intersection zone of those anomalies (Figure 6.1) is interpreted as the reflection of mineralized zone. Thisintersection is given by blue, red and black colors following NW-SE direction as that of geologically delineated iron bearing zone. The same zone is correlated to interpreted 2D IP/R section of line 50N (Figure 5.22).

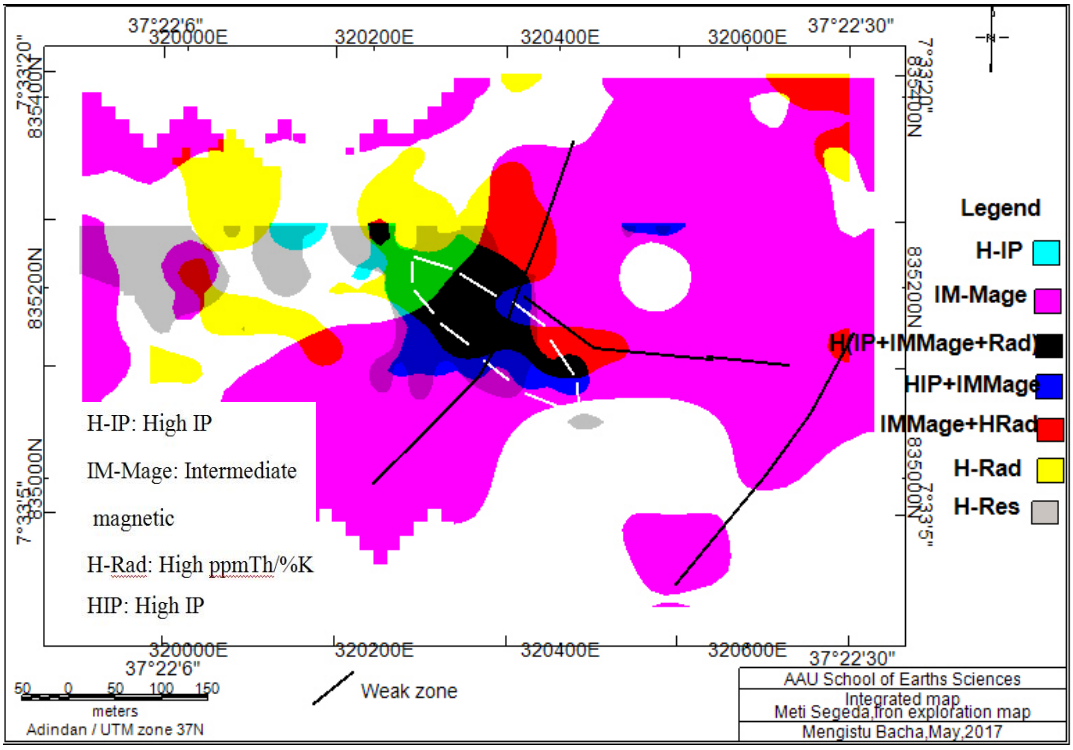

Figure 6.1: Compilation map of interpreted geophysical methods

Thin section analysis show iron-oxide and quartz mineral for rock samples took from survey area. Susceptibility measurement of rock samples, from the intersection zone shows intermediate susceptibility contrast in relation to its surrounding. Those intermediate susceptibilities, high iron oxide (hematite) and high quartz concentrations are defining the same intersection zone which is mapped by analytic signal as the contact zone of intermediate susceptibilities and by tilt angle derivative as the intersecting area of lineaments within the contact zone. From IP/R plan maps (Figure 5.10 and 5.15) the resistive and chargeable nature of the intersection zone could be the effect of quartz and hematite respectively. Moreover, if the hematite (less resistive in nature) is not continuous throughout the mineralized zone, its conductive nature does not contribute much and the resistive nature of quartz dominates to reflect high resistivity responses.

From residual anomaly of figure 5.3 NE-SW weak zone crossing the mineralized zone and line 0 near 835200N. Along this zone equivalent Uranium concentration (Figure 5.28 and 5.31) show higher reading while, tilt angle derivative map (Figure 5.5) show a lineament. As moderately high Uranium is related to fault structures, this NE-SW zone can be a fault zone. In other way, from (Figure 5.10 and 5.15) both the chargeability and resistivity anomalies are not extends beyond 320400E toward east. Maybe this is due to some kind of discontinuities (tectonic discontinuity which can be fault) along this location. The same structure is observed in residual map (Figure 5.3), tilt angle derivative (Figure 5.5) and in Uranium concentration map (Figure 5.28) which show high values over faults.

Referring figure 5.3, 5.4, 5.5 and 5.28 the mineralized zone is occurred where structures are intersect within contact zone. This occurrence of mineralization in tectonic zone indicates the spatial association of mineralization with structure.

From ASTER imagery data analysis, iron alteration is observed at western side of already delineated mineralized zone (Figure 5.38). This zone seems coincide to intermediate magnetic susceptibility (Figure 5.4) and high chargeability of level 6 (Figure 6.2).

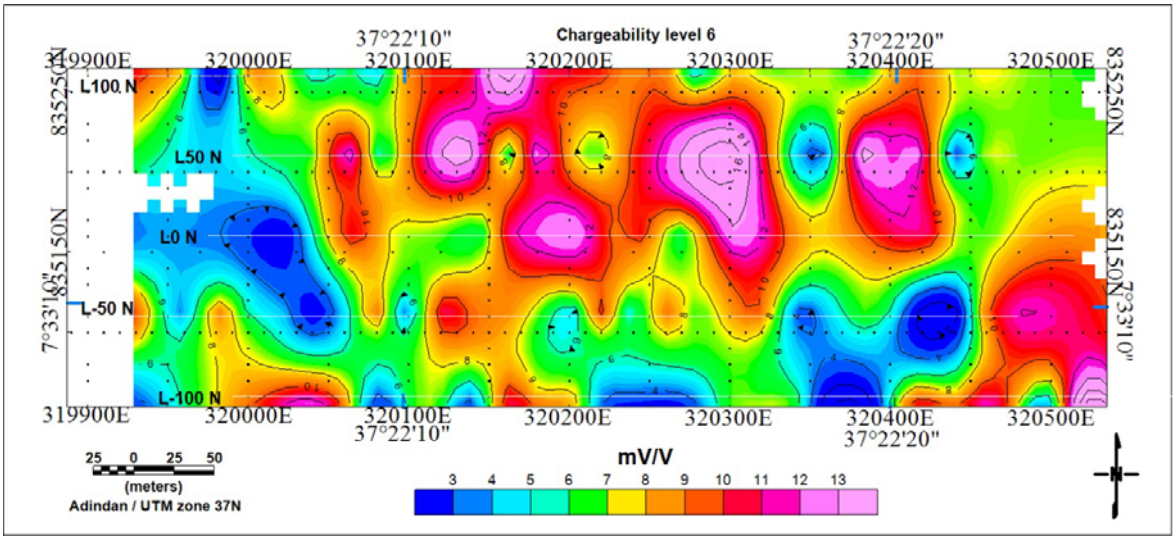

Figure 6.2: Chargeability plan map of level 6

CHAPTER VII

7. Conclusion and Recommendation

7.1 Conclusions

Detail analyses of the survey results enabled to make the following conclusions:

1. Lithologic features that bounded the contact zone of intermediate susceptibilities are mapped as basalt and rhyolite
2. Mineralization is occurred in a contact zone where lineaments intersect
3. NW-SE and NE-SW lineaments and high Uranium concentrations are revealed the spatial association between structure and iron mineralization
4. The anomaly is modeled as easterly striking iron bearing zone of 200m length and 105m depth.
5. From inverted IP section, delineated anomaly has a vertical extent more than 30m, a lateral extent of 190m and width of 60m
6. Based on non-continuity of hematite, lateral extent and vertical extent of the mineralized zone, the prospect may be used for small scale investment
7. The mineralized zone is mainly characterized with high IP (> 15mV/V) and high resistivity (>400Ω.m) due to quartz and hematite in association.

7.2 Recommendation

1. If small scale iron potentials collectively are the option for large scale investment, the current occurrence is recommended to be considered
2. Anomalies for mineralized zone are opened toward north. And processed ASTER satellite imagery data shows the distribution of iron is continuing toward northwest. These information may be indicators of wider anomaly features at northwest and north which need extensional surveys
3. Detail and wider geochemical analysis is recommended for iron oxides
4. It is recommended to map the geology and structure of the area in detail to substantiate the geophysical results
5. For mapping lithologies and structures gravity survey is also recommended

References

1. **Abbate, P. B.** and Mario, S. **(1980).** Geology of Ethiopia: A Review 2 and Geomorphological Perspectives, page: 15

2. **Agocs, W. B.(1951).** Least-squares residual anomaly determination: Geophysics. **16**, 686–696

3. **Alan, E., Mussett, M. and Aftab, K. B. (2000).**Looking into the Earth an introduction to geological geophysics. Department of Earth Sciences, Liverpool University, UK, Cambridge University Press.**15**: 225

4. **Carlos, A.T.** Mineral Exploration Using Aster Images, University of Texas at San Antonio

5. **Chapman & Hall. (1997).** Principle of applied Geophysics, UK, London.

6. **Charles, J., Moon, M. K. Whateley, G. and Anthony, M. E. (2006)**. Introduction to Mineral Exploration, 2nd edition. BLACKWELL PUBLISHING,350 Main Street, Malden, MA 02148-5020, USA, pp136

7. **Dalstra, H. I., Hodkiewicz, P., Flis, M.,Thorne, W. &McCuaig, C. (2007).** Recent Advances in BIF-related Iron Ore Models and Exploration Strategies. In: Milkereit, B.(ed.) "Proceedings of Exploration 07: Fifth Decennial International Conference on Mineral Exploration", 811821.

8. **Davidson, A., Moore, M.J., Davies, C.J. (1983).**Reconnaissance Geology and Geochemistry of Parts of Ilubabor Kefa, Gemu Gofa and Sidamo, Ethiopia. Bull. No2. Ottawa

9.Davidson. A. (1980). Age of volcanism and rifting in southwestern Ethiopia, Nature 283:657–658)

10. **Dey, A. and Morrison, H.F. (1979a).**Resistivity modeling for arbitrary shaped two-dimensional structures. Geophysical Prospecting **27**, 1020-1036.

11. **Durrance, E. R. (1986).**Radioactivity in geology: Principles and applications. Ellis Horwood, Chichester, and Halstead Press, New York

12. **Frantisek, H., Marta, C. and Martin, C. (2009).** The Use of Magnetic Susceptibility of Rocks in Geological Exploration (case history study),Ter Plus, Geophysical Equipment Supplier.

13. **Girma Woldetinsae, Dawit Mamo and Yohannes Demisse. (2006).** SIP/Resistivity and Magnetic Survey in Galesa area (Western Ethiopia), Dugi-Mambuk.Unpublished Technical Report, Geological Survey of Ethiopia, Addis Ababa, Ethiopia.

14. **Golivkin, N.I. and Kovalevich,V.B. (1982).**Preliminary report on iron ore occurrence in the provinces Wollega, Eritrea, Harrar and Keffa of Socialist Ethiopia. Published technical report, GSE, Addis Ababa, Ethiopia

15. **Habtamu Eshetu, Alula Demewez, Ezra Tadesse and Debebe Kifle. (2014).** Engineering geological and Geo-hazard distribution mapping of Jima map sheet. Unpublished technical report, GSE, Addis Ababa, Ethiopia.

16. **Haha, A. (1965).**Two application of Fourier analysis for the interpretations of geomagnetic anomalies Journal of geomagnetic and Geoelectric**17,**195-225.

17. **Hamral, M. (1963).**Report on iron ore occurrences in Mai Gudo region (Nada district, Kaffa Province), Ministry of mines ,Addis Ababa, Archives of the Ministry of mines.

16.**Jens, G. and Nicolas, J. (2000).** Iron and Manganese ore deposits: Mineralogy, geochemistry, and Economic geology. Rand Afrikaans University, South Africa.

19. **John, M.R. (1997).** An Introduction Applied and Environmental Geophysics, Reynolds Geo-Sciences Ltd, UK, page 428.

20. **Kamar, S. A.** Geophysical Surveying Using Magnetics Methods, EBS 309: Geofizik Carigali, pp 9.

21. **Ken, Z. Z**. Engineering & Research Organization Geophysical prospecting methods.

22. **M.H. Loke. (2001).**2-D and 3-D electrical imaging surveys email: mhloke@pc.jaring.my.

23. **Macleod, I.N., Vierra, S. and Chaves, A. C. (1993)**. Analytical signal and reduction to-the-pole in the interpretation of total magnetic field at low magnetic latitudes. Proceeding of the Third International Congress of the Brazilian Geophysical Society.

24. **Mark, E.E. (2013).** Near-Surface Applied Geophysics. Texas A &M University, Cambridge university press.

25.**Masresha Gebrselassie and Wolf, U. R. (2000).** A review of the metallic mineral resource potential of Ethiopia. Published Technical Report, Geological Survey of Ethiopia, Addis Ababa, Ethiopia.

26. **Mengesha Tefera, Tadiwos Chernet and workineh Haro. (1996).** Explanation of the geological map of Ethiopia 2nd edition. Unpublished technical report, GSE, Addis Ababa, Ethiopia

27. **Merla, G., Abbate, E., Azzaroli, A., Brinni, P., Cnuti, p., Fuzuli, M., and Tacconi, P.(1979).**
The Geology of Ethiopia and Somalia; with accompanied map of 1:2000000. Department of Geology and Paleontology. Florence, Italy.

28. **Milan, H. (1963).** The iron and Manganese ore deposits in Ethiopia. Published technical report, GSE, Addis Ababa, Ethiopia

29. **Mohr, P.A.(1983).**Ethiopian flood basalt province, Nature, 303:577–584

30. **Murdock, T.G. (1960).**Geology and mineral resource of Ethiopia. U.S. Dep. of Interior, Working paper 10, Addis Ababa.

31. **Neil, A, and Neil, C., Rick, H. and Phil, S. (2008).** Geophysical Methods Commonly Employed for Geotechnical site Characterization, Missouri University of Science and Technology, USA.

32.**Parasnis, D.S. (1997).**Principles of Applied Geophysics. 5th Edition, Chapman and Hall, London, 104-176).

33. **Philip, K., Michael, B. and Ian, H. (2002).**An Introduction to Geophysical Exploration, 3rdedtion**.** Department of Earth Sciences University of Bristol, Blackwell Science Ltd, Australia

34. **Poveromo, J. J. (2016).** Iron Ores. Date of access Oct, 2016 from http://183.91.33.13/cache/jpkc.lut.

35. **Reynolds, R.L., Rosenbaum, J.G., Hudson, M.R., and Fishman, N.S. (1990).**Rock magnetism, the distribution of magnetic minerals in the Earth's crust, and aeromagnetic anomalies, in Hanna, W.F., ed., Geologic.

36. **Roset,W.E.,Verhoef, J., and Pilkington, M. (1992).**Magnetic interpretation using 3D analytical signal. Geophysics **57**, 116-125.

37.**Rosli, S., Imran, A., Ahmad, S. M.(2012)** .The Study of Iron Ore Prospect using 2-D Resistivity and Induced Polarization (IP) Method , Geophysics Section, School of Physics, University of Sains, Penang, Malaysia.

38.**Salem, A., Williams, S., Fairhead, J.D., Ravat, D.J. and Smith R. (2007).**Tilt-depth method: a simple depth estimation method using first-order magnetic derivatives, The Leading Edge, 1502-1505.

39. **Sara, M. M. (2013).**Investigating Fault Structure Using Electrical Resistivity Tomography, Faculty of the Physics Department, California Polytechnic State University, San Luis Obispo, In Partial Fulfillment of the Requirements for the Degree Bachelor of Science.

40. **Scintrex. (1989).** GAD-6 Four Channel Stabilized Gamm-Ray Spectrometer, operational manual.

4. **Scientrex. (1989).** IPR-12 Time domain IP/resistivity receiver operational manual

42. **Telford, W. M., Sheriff, R. F.(1990).** Applied geophysics, 2nd edition, Cambridge university press

43. **Thomas, M.D., Walker, J.A., Keating, P., Shives, R., Kiss, F., and Goodfellow,W.D. (2000).** Geophysical atlas of massive sulfide signatures, Bathurst mining camp, New Brunswick: Geological Survey of Canada Open File 3887,105 p.

44.**Verduzco, B. (2004).**New insights into magnetic derivatives for structural mapping, The Leading Edge, v. **23**, p. 116-119.

45. **Workineh Haro, Asamnew Besufikad, Daba Bulto, Fikadu Bekele and Mohamed Edris. (2012).**Geology, Geochemistry and Gravity Survey of Jimma area. Unpublished technical report, GSE, Addis Ababa, Ethiopia.

46. **Yiheyse Kebede, Mohamednur Dessisa, Akalwold Seifu, Aklilu Hailu, Hailesilassie G/Silassie and Aboma Abdissa. (2000)**. Geological Survey for Gold and Base Metals In Gechungia Area, Benishangul-Gumuz Region. Unpublished Technical Report, Geological Survey of Ethiopia, Addis Ababa, Ethiopia.